Thesis

First-Principles Study on Solid Oxygen and Selenium under High Pressures

Minoru OTANI

OSAKA UNIVERSITY
Graduate School of Engineering Science
Department of Physical Science
Division of Material Physics
Toyonaka Osaka

January **2000**

Thesis

First-Principles Study on Solid Oxygen and Selenium under High Pressures

Minoru OTANI

OSAKA UNIVERSITY
Graduate School of Engineering Science
Department of Physical Science
Division of Materials Physics
Toyonaka Osaka

January 2000

Abstract

First-principles calculations are performed for molecular phases of solid oxygen and monatomic phases of solid oxygen and selenium.

First-principles band calculations are carried out for the first time for molecular phases of solid oxygen and quite interesting results have been obtained. At large volumes (low pressures) an insulating antiferromagnetic state is the most stable. With decreasing the volume (increasing the pressure) the magnetic moment decreases and finally a nonmagnetic metallic state becomes the most stable above about 100 GPa. The metallic state is realized by band overlapping.

For monatomic phases of solid oxygen it is shown that transition from the β-Po to the bcc structures will be hard to occur in the pressure region accessible by experiments in contrast with other VI-b elements, S, Se and Te. For monatomic selenium our calculation reproduces fairly well the pressure-induced phase transition from β-Po to bcc observed experimentally. The calculated transition pressure is lower by 30 GPa than the observed one (150 GPa), but the calculated pressure dependence of the lattice parameters agrees well with the observations in a wide range of pressure.

We also investigate pressure-induced superconductivity in monatomic selenium by calculating lattice dynamics and electron-lattice interaction with use of a first-principles method based on the linear-response theory. For bcc selenium, with decreasing pressure, softening of phonon frequency is observed and in particular the transverse mode along the Γ-N line in the Brillouin zone exhibits a phonon anomaly, *i.e.*, a dip in the middle of the line. Finally, we calculate the pressure dependence of the superconducting critical temperature (T_c) of both the β-Po and bcc phases and predict a discontinuous jump of T_c going from β-Po to bcc.

Acknowledgements

The author would like to express his sincere gratitude to Professor N. Suzuki, under whose guidance this work has been done, for valuable suggestions and enlightening discussions throughout the course of the work and also for his help in preparing the manuscript.

He also thanks Associate Professor M. Shirai for his continuous encouragement and for helpful discussions. He is grateful to Associate Professor H. Miyagi and Dr. K. Yamaguchi for valuable discussions and suggestions at the early stage of this work.

He greatly thanks Dr. S. Yu. Savrazov of Max Planck Institute for providing him with the FPLMTO and LR-LMTO program. He is very grateful to Professor Y. Akahama of Himeji Institute of Technology for useful discussions and also for showing him their experimental data prior to publication.

He willingly thanks Dr. T. Kawamoto for fruitful discussions and providing him with the exact diagonalization program for two-band Hubbard Hamiltonian.

He thanks all of the students of Suzuki laboratory for their generosity on his use of computer and also for fruitful discussions.

Finally he thank his parents and his friends for their warmhearted helps.

Contents

Chapter 1

Introduction

1.1 Experimental and theoretical background

Among many homonuclear diatomic molecules only the oxygen molecule has a spin in its ground state, which gives quite interesting properties to assemblies of oxygen molecules. In particular it yields a rich variety of phases of solid oxygen in the temperature-*vs*-pressure plane[1–6] as shown in Fig.1.1.1 and 1.1.2. The magnetic moment of an oxygen molecule comes from two parallel spins in degenerate antibonding π^* orbitals, $\pi^*_{2p_x}$ and $\pi^*_{2p_y}$ as shown below.

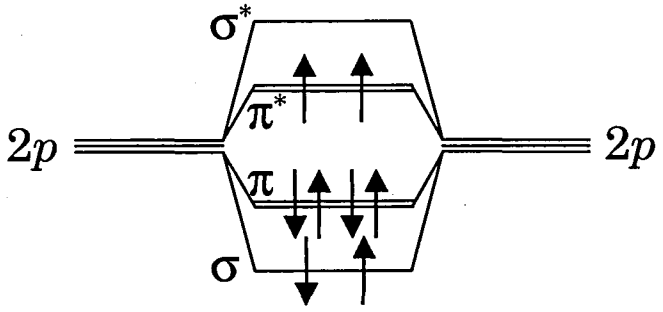

The α-phase which appears at low pressures and low temperatures has a monoclinic crystal structure (space group $C2/m$) which contains two molecules in the unit cell as shown in Fig. 1.1.3. In this α-phase an antiferromagnetic (AF) order is realized and the magnetic moment is reported to be 0.6 μ_B/atom [3]. With increasing pressure at low temperatures

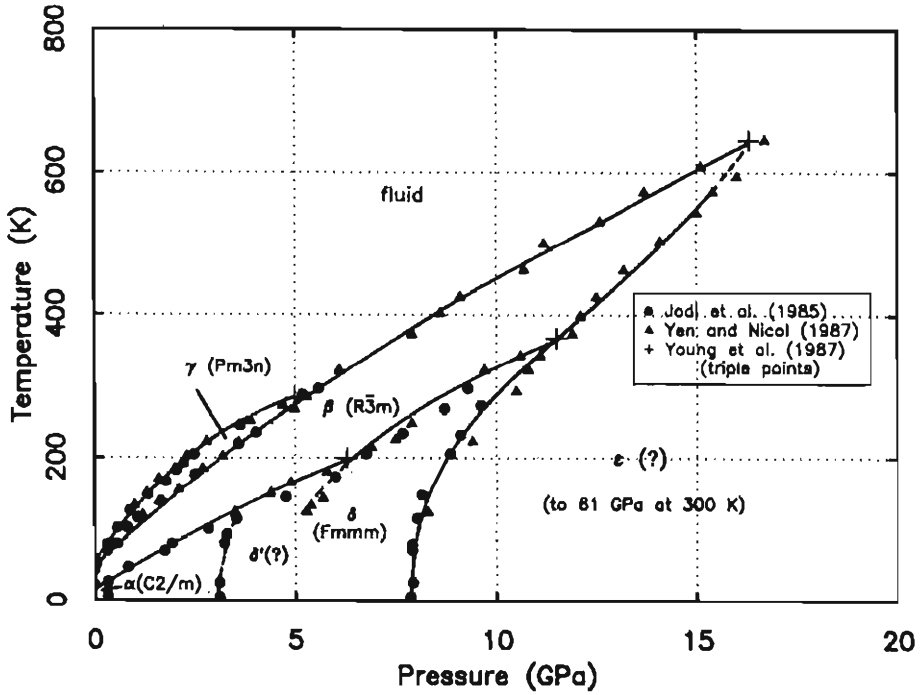

Figure 1.1.1: Temperature-pressure phase diagram of solid oxygen [6].

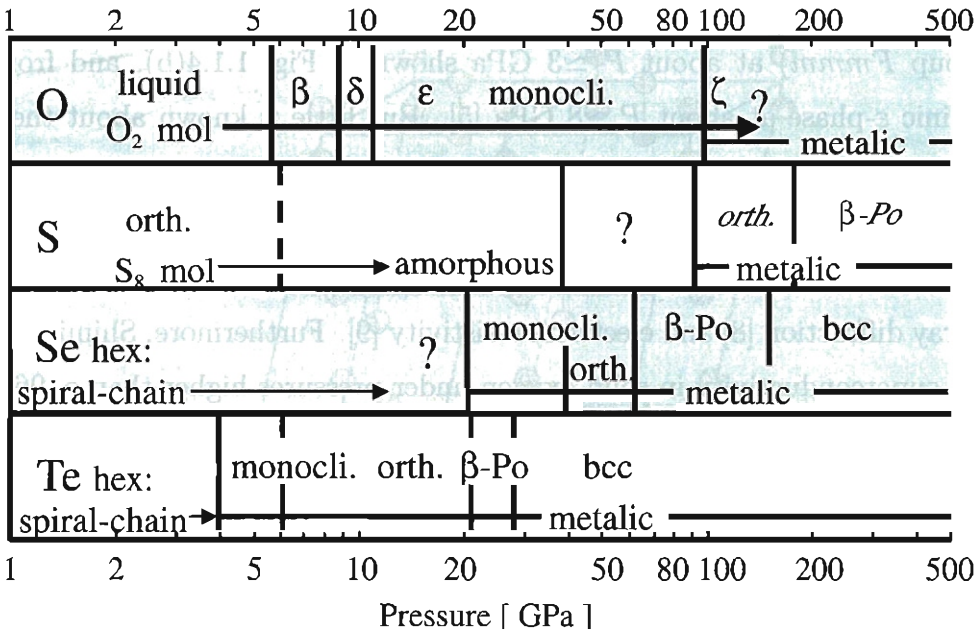

Figure 1.1.2: The phase sequence of VI-b elements as a function of pressure at room temperature. The blue bands represent target materials in this thesis.

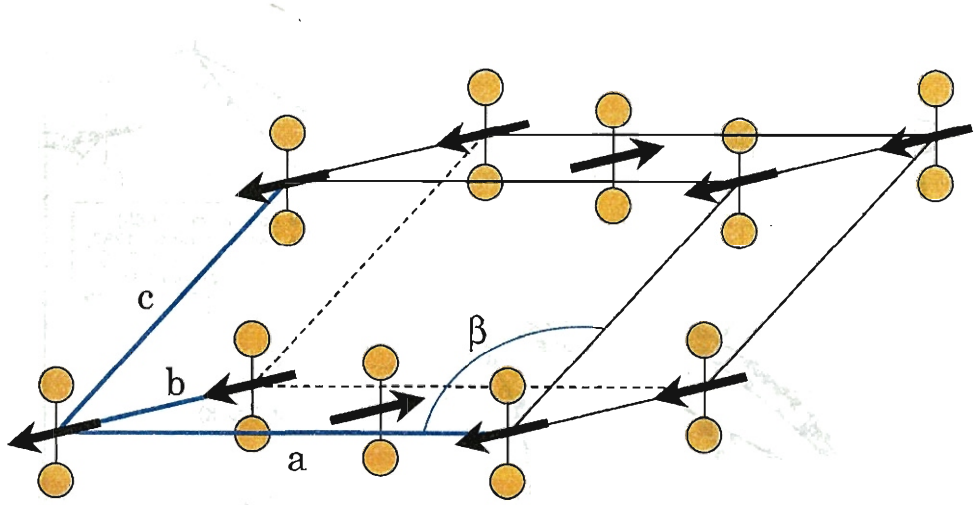

Figure 1.1.3: The crystal structure of α-O_2. The arrows at molecules denote the magnetic moment.

successive structural phase transitions occur: from α-phase to orthorhombic δ-phase (space group $Fmmm$) at about $P \simeq 3$ GPa shown in Fig. 1.1.4(b), and from δ-phase to monoclinic ε-phase at about $P \simeq 8$ GPa [5]. But little is known about the magnetic properties of the δ- and the ε-phases.

Recently a couple of experimental observations which might evidence metallization of oxygen above $\sim$96 GPa have been reported: measurements of optical absorption spectra [7], X-ray diffraction [8] and electrical resistivity [9]. Furthermore, Shimizu *et al.* have discovered superconductivity in solid oxygen under pressures higher than $\simeq$ 96 GPa [10]. The transition temperature is reported to be $T_c = 0.6$ K. Interestingly Akahama *et. al.* suggested that the metallization is realized in a molecular phase [8]. As the crystal structure of the metallic molecular state they proposed a monoclinic phase (called ζ-phase) which is an isostructure of the ε-phase. Theoretically, Serra *et.al.* [11] have performed *ab initio* deformable-cell MD simulations and proposed a new base-centered monoclinic structure for the ζ-phase. Kususe *et.al.* [12] have also investigated the molecular phase of oxygen by using first-principles calculations and supposed the molecular dissociation

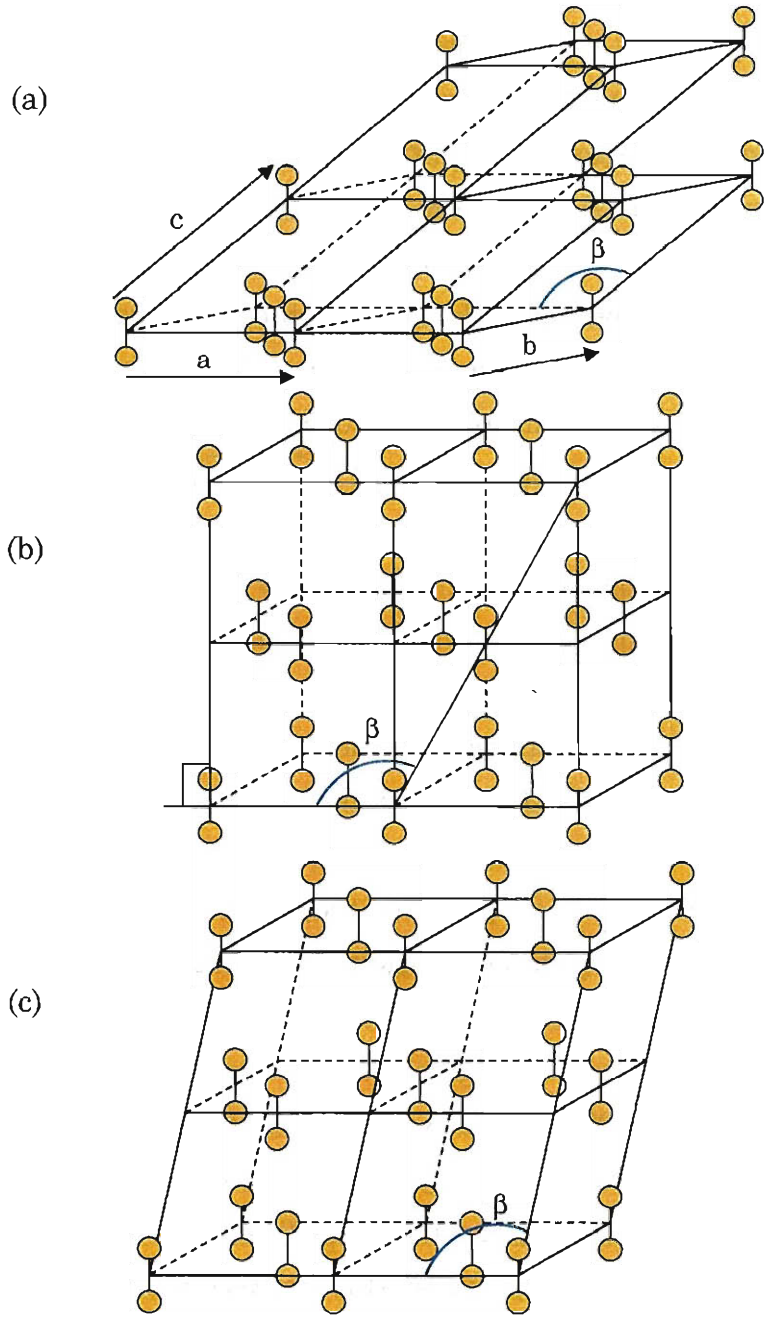

Figure 1.1.4: The crystal structures of (a) the α-phase, (b) the δ-phase and (c) the ε-phase (or ζ-phase) of oxygen. With increasing pressure the monoclinic angle β of the α-phase decreases toward that of the δ-phase. The ζ-phase is considered to be an isostructure of the ε-phase [8].

does not occur at the metallization pressure. They concluded that in the ζ-phase magnetic state is collapsed and a nonmagnetic metallic state is realized.

Another interesting example of oxygen molecular assembly is oxygen in restricted geometry such as oxygen physisorbed in Cu-trans-1,4-cyclohexanedicarboxylic acid (CCHD) having one-dimensional (1-D) micropores. Magnetic measurements on this system have given quite peculiar results [13]. According to measurements of magnetization process the saturation moment is $2\mu_B$ per molecule, and the observed susceptibility indicates clearly the existence of a gap. However, the temperature dependence of the susceptibility is explained neither by S=1 Heisenberg antiferromagnetic (AF) chain nor by S=1 dimer model. It is rather understood well by S=1/2 dimer model. These results indicate that S=1 state is rather unstable in this oxygen molecular assembly and also suggest that degeneracy of π^* orbitals may be lifted.

The elements in the same group of the periodic table exhibit a close homology in their high pressure behavior. In other VI-b elements, S, Se and Te, molecular dissociation to a monatomic phase has been observed. The monatomic phase first realized has a β-Polonium (β-Po) structure [13–18], and with further increasing pressure transition from the β-Po to the bcc structures has been observed in Se and Te [14, 15, 16] or predicted for S [20]. Recently, Rudin *et. al.* predicted the simple-cubic phase is realized between the β-Po and the bcc phases [21]. This suggests that O and S have a structural sequence different from that of Se and Te in the monatomic phase. Sulfur, selenium and tellurium show also superconductivity under high pressures. Their transition temperatures are T_c = 10 K at 100 GPa in S [22, 23], 4.5 K at 36 GPa in Se [18] and 2.5 K at 5 GPa in Te [16]. In case of Te superconductivity has been observed also in monatomic simple structures under higher pressures, and its T_c is 2.6 K at 27 GPa in the β-Po structure and 7.4 K at 35 GPa in the bcc structure [16]. In case of Se and S there has been no experimental measurements of superconductivity in their monatomic phases. There is only a first-principles calculation of T_c for monatomic bcc S, which predicts T_c = 15 K at 550 GPa [20].

In comparing T_c of molecular solid oxygen with those of S, Se and Te a question arises: why T_c of oxygen is so low ? It is also an interesting problem to investigate the possibility

of superconductivity in monatomic simple structures of selenium and oxygen. In Te a jump in T_c from 2.5 K to 7.4 k is observed at 32–35 GPa [16]. Theoretically, Mauri, *et. al.* have suggested that the jump in T_c is related to the phonon softening in the bcc phase [24], namely with decreasing pressure the phonon anomaly enhance the electron-phonon coupling. For Se, on the other hand, there is neither experimental observation of superconductivity nor *ab initio* calculation for pressure dependence of phonon frequencies, electron-phonon interaction and T_c, in its monatomic phases.

1.2 Purpose of this thesis

For solid oxygen, if the insulator-metal (IM) transition occurs truly in the molecular phase, several interesting questions arise. What is the driving force of the IM transition? Is the mechanism the same as for the IM transition of other diatomic molecular solids such as halogens? Does the spin remain even in the metallic phase or does it disappear before the IM transition? It will be quite important to seek for the answers to these questions. As the first step to understand or predict the above interesting properties of solid oxygen under high pressures we carry out first-principles calculations of the electronic band structures of the molecular phases of solid oxygen.

Secondly we study in detail the structural phase transition from β-Po to bcc phase in monatomic Se. Then, for comparison we study also the possibility of transition from β-Po to bcc in monatomic oxygen.

Finally we investigate pressure-induced superconductivity in monatomic selenium by carrying out first-principles calculation for lattice dynamics and electron-phonon interaction. At first we calculate phonon frequencies and electron-phonon coupling constants for both the bcc and β-Po structures by using the linear-response LMTO method. Then, with use of the Allen-Dynes formula we evaluate the pressure dependence of the superconducting transition temperature T_c in both the phases.

In Appendix A we give the results of analysis for 1D two-band Hubbard Hamiltonian which is relevant to a 1D oxygen chain. Appendix B is devoted to detailed theoretical description of the calculational methods used in this thesis.

Chapter 2

Theoretical Method

2.1 Full-potential LMTO method

In this thesis theoretical investigations for the electronic band structure is done by full-potential linearized muffin-tin orbital (FPLMTO) method [25, 26, 27]. In this section we outline the essence of FPLMTO method.

For N-electron systems with N as large as $\sim 10^{23}$, it is difficult or practically impossible to solve exactly the eigenvalue and eigenstate by correctly taking into account the electron-electron interaction. Therefore, usually the electron-electron interaction term is approximately treated by a self-consistent procedure on the basis of a one-particle picture. A typical example of such approximations is the local density functional approximation (LDA), in which exchange and correlation energy part are represented by a functional of electron density[28, 29]. By using LDA the N-electron problems result in to solving the Kohn-Sham equation as follows

$$\left[-\frac{1}{2}\nabla^2 + v_{\text{eff}}\right]\varphi_i(\boldsymbol{r}) = \varepsilon_i\varphi_i(\boldsymbol{r}), \tag{2.1.1}$$

where v_{eff} is the one-particle effective potential which includes external field, bare Coulomb interaction and exchange correlation energy.

The FPLMTO method is based on the density-functional theory (DFT) with usual LDA. The crystal space is partitioned into nonoverlapping MT spheres (MTS) centered on each atom ($|\boldsymbol{r}| \leq S_{MT}$) and the remaining interstitial region ($|\boldsymbol{r}| > S_{MT}$). Within the

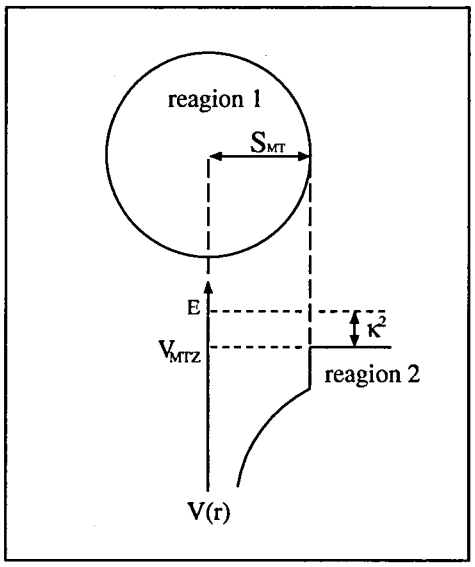

Figure 2.1.1: A schematic picture of muffin-tin approximation where the kinetic energy in the interstitial region is defined by $\kappa^2 = E - V_{\mathrm{MTZ}}$

spheres the basis functions are represented in terms of numerical solutions of the radial Schrödinger equation for the spherical part of the potential multiplied by spherical harmonics. In the interstitial region where the potential is essentially flat, the electronic state is described by the Hankel functions, which are taken from the solutions of Helmholtz's equation:

$$(\nabla^2 + \kappa^2) f(\boldsymbol{r}) = 0. \tag{2.1.2}$$

For the solution of the radial part of the equation (2.1.2) we use some fixed kinetic energy of interstitial energy κ^2. Inside the MTS, the radial part of the electronic state is described by the linear combination of $\phi_{RL}(r_R - t, \varepsilon_{\kappa R\ell})$ and it's energy derivative $\dot{\phi}_{RL}(r_R - t, \varepsilon_{\kappa R\ell})$, where ϕ is the solution of the one-electron Schrödinger equation inside MTS with the spherically symmetric part of the potential for the energy $\varepsilon_{\kappa R\ell}$ which is taken with the center of interest, L denotes the combined index for ℓm and $r_R = r - R$, other definition of the vector is shown in figure 2.1.2. The coefficients of the linear combination are determined with the condition of smooth augmentation to the Hankel function, $K_{\kappa L}(r_R - t)$, at the boundary of MTS centered at $\boldsymbol{R} + \boldsymbol{t}$. Inside any other MTS

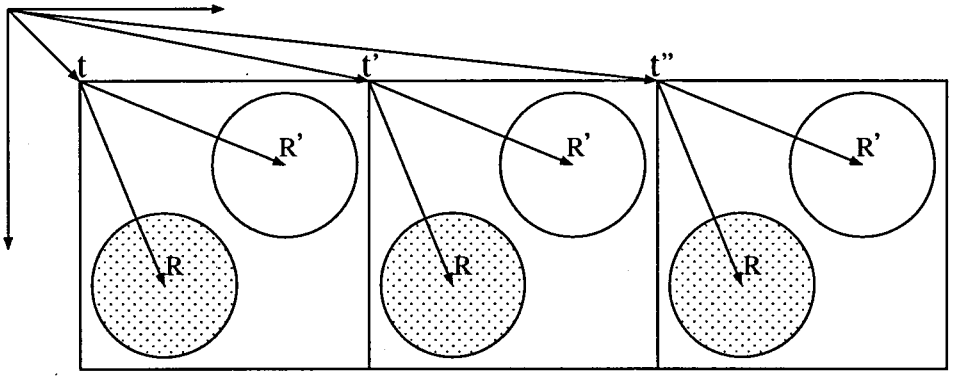

Figure 2.1.2: The definition of position vectors used in this section: $\boldsymbol{R}$ denotes the position of atoms in the unit cell and $\boldsymbol{t}$ represents transnational vector.

centered at $\boldsymbol{R}+\boldsymbol{t}'$ the electronic states are also described by the linear combination of ϕ and $\dot{\phi}$, and the coefficients are determined as follows. The tail of the Hankel function is expanded in terms of Bessel functions, which are also the solutions of equation (2.1.2).

$$K_{\kappa L}(\boldsymbol{r}_R - \boldsymbol{t}) = 4\pi \sum_{L'L''} C_{LL'L''} J_{\kappa L'}(\boldsymbol{r}_{R'} - \boldsymbol{t}) K^*_{\kappa L''}(\boldsymbol{t} - \boldsymbol{t}' + \boldsymbol{R} - \boldsymbol{R}'), \tag{2.1.3}$$

where the Gaunt coefficients $C_{LL'L''}$, augmented Hankel K and Bessel J function are defined as follows:

$$\begin{aligned} C_{LL'L''} &= \int Y_\ell^m(\hat{\boldsymbol{r}}) Y_{\ell'}^{m'}(\hat{\boldsymbol{r}}) Y_{\ell''}^{m*''}(\hat{\boldsymbol{r}}). \\ K_{\kappa L}(\boldsymbol{r}) &= -\frac{\mathrm{i}^{\ell+1}(\kappa S_{MT})^{\ell+1}}{(2\ell-1)!!} Y_\ell^m(\hat{\boldsymbol{r}}) h_\ell(\kappa r) \\ J_{\kappa L}(\boldsymbol{r}) &= \frac{1}{2}\frac{\mathrm{i}^\ell (2\ell-1)!!}{(\kappa S_{MT})^\ell} Y_\ell^m(\hat{\boldsymbol{r}}) j_\ell(\kappa r). \end{aligned} \tag{2.1.4}$$

The phase factor of spherical harmonic Y_L to be used is defined after Condon and Shortley [30], and $f_L \equiv \mathrm{i}^\ell Y_L f_\ell$, where f is K, J, ϕ, $\dot{\phi}$, and so on. We introduce the structure constants in direct space as

$$S_{R'L'RL}(\boldsymbol{t} - \boldsymbol{t}', \kappa) = 4\pi \sum_{L''} C_{LL'L''} K^*_{\kappa L''}(\boldsymbol{t} - \boldsymbol{t}' + \boldsymbol{R} - \boldsymbol{R}'). \tag{2.1.5}$$

Thus the expansion of Hankel function Eq.(2.1.3) is rewritten as follows

$$K_{\kappa L}(\boldsymbol{r}_R - \boldsymbol{t}) = \sum_{L'} C_{LL'L''} J_{\kappa L'}(\boldsymbol{r}_{R'} - \boldsymbol{t}) S_{R'L'RL}(\boldsymbol{t} - \boldsymbol{t}', \kappa). \tag{2.1.6}$$

The last step is to perform lattice summation of LMTO's centered at different sites with phase shift $e^{i\boldsymbol{k}\cdot\boldsymbol{R}}$ in order to guarantee that our basis functions would satisfy the Bloch theorem, and finally we obtaine the basis functions as in the following form

$$\chi^{\boldsymbol{k}}_{\kappa RL}(\boldsymbol{r}) = \kappa \begin{cases} \Phi^K_{\kappa RL}(\boldsymbol{r}_R)\delta_{RR'} + \sum_{L'} \Phi^J_{\kappa R'L'}(\boldsymbol{r}_{R'}) S^{\boldsymbol{k}}_{R'L'RL}(\kappa) & \text{for } r_{R'} < S^{R'}_{MT}, \\ K_{\kappa L}(\boldsymbol{r}_R)\delta_{RR'} + \sum_{L'} J_{\kappa L'}(\boldsymbol{r}_{R'}) S^{\boldsymbol{k}}_{R'L'RL}(\kappa) & \text{for } r_{R'} \in \Omega^{\text{int}}_{R'}, \end{cases} \tag{2.1.7}$$

where $S^{\boldsymbol{k}}_{R'L'RL}(\kappa)$ is the Fourier transformation of structure constant

$$S^{\boldsymbol{k}}_{R'L'RL}(\kappa) = \sum_{\boldsymbol{t}} e^{i\boldsymbol{k}\cdot\boldsymbol{r}} S_{R'L'RL}(\boldsymbol{t},\kappa).$$

The functions $\Phi^K_{\kappa RL}(\boldsymbol{r}_R)$ and $\Phi^J_{\kappa RL}(\boldsymbol{r}_R)$ are the linear combination of ϕ_{RL} and $\dot{\phi}_{RL}$, in which the functions match smoothly to Hankel and Bessel functions at the MTS boundary, respectively, as described above.

With the LMTO basis set defined in (2.1.7) the wave functions $\psi_{\boldsymbol{k}\lambda}(\boldsymbol{r})$ for valence electrons is given by linear combinations of LMTO's:

$$\psi_{\boldsymbol{k}\lambda}(\boldsymbol{r}) = \sum_{\kappa RL} A^{\boldsymbol{k}\lambda}_{\kappa RL} \chi^{\boldsymbol{k}}_{\kappa RL}(\boldsymbol{r}), \tag{2.1.8}$$

where λ represents the bands, the coefficients $A^{\boldsymbol{k}\lambda}_{\kappa RL}$ are determined from the variational principle. For the one-electron Hamiltonian given by DFT they are found from the eigenvalue problem

$$\begin{aligned} &\sum_{\kappa RL} \left[\langle \chi^{\boldsymbol{k}}_{\kappa' R'L'} | - \nabla^2 + V^{\text{MT}}(\boldsymbol{r}) + V^{\text{NMT}}(\boldsymbol{r}) | \chi^{\boldsymbol{k}}_{\kappa RL} \rangle - \varepsilon_{\boldsymbol{k}\lambda} \langle \chi^{\boldsymbol{k}}_{\kappa' R'L'} | \chi^{\boldsymbol{k}}_{\kappa RL} \rangle \right] A^{\boldsymbol{k}}_{\kappa RL} \\ \equiv &\sum_{\kappa RL} \left(H^{\boldsymbol{k}}_{\kappa' R'L',\kappa RL} - \varepsilon_{\boldsymbol{k}\lambda} O^{\boldsymbol{k}}_{\kappa' R'L',\kappa RL} \right) A^{\boldsymbol{k}}_{\kappa RL} = 0, \end{aligned} \tag{2.1.9}$$

where $V^{\text{NMT}}(\boldsymbol{r})$ stands for the spherical and $V^{\text{MT}}(\boldsymbol{r})$ for nonspherical parts of the potential.

Some of other computational techniques which are necessary for actual calculations using the LMTO method are described in Appendix A.1.

2.2 Linear-response calculations

For the calculation of the dynamical property of solid and electron-phonon interactions, we use the linear-response FPLMTO (LR-LMTO) method [31, 32]. The method is based on DFT and it uses LMTO as a basis for representing first-order corrections to the one-electron wave functions $\psi_{k\lambda}$. First we consider infinitesimal atomic displacement $\boldsymbol{u}_{\ell\mu}$ from the equilibrium positions within the framework of the adiabatic and harmonic approximations. The equation of motion for $\boldsymbol{u}_{\ell\mu}$ is now given by

$$M_\mu \ddot{u}^\alpha_{\ell\mu} = -\sum_{m\nu}\sum_{\beta} V^{\alpha\beta}_{\ell\mu m\nu} u^\beta_{m\nu}. \tag{2.2.1}$$

where $V_{\ell\mu m\nu}$ is the force constant. Introducing the Fourier transform as follows

$$\boldsymbol{u}_{\ell\mu} = \frac{1}{\sqrt{N}} \sum_{\boldsymbol{q}} \boldsymbol{u}^{\boldsymbol{q}}_\mu \mathrm{e}^{\mathrm{i}\boldsymbol{q}\cdot\boldsymbol{R}_\ell} \tag{2.2.2}$$

and assuming the time dependence of $\boldsymbol{u}^{\boldsymbol{q}}_\mu$ as $\mathrm{e}^{\mathrm{i}\omega t}$, then the problem for the motion of atoms result in to solve the secular equation given by

$$\sum_{\mu\beta} \left[D^{\alpha\beta}_{\mu\nu}(\boldsymbol{q}) - M_\mu \omega^2 \delta_{\mu\nu}\delta_{\alpha\beta} \right] u^\beta_\nu(\boldsymbol{q}) = 0, \tag{2.2.3}$$

where α, β is the Cartesian component and the matrix $D(\boldsymbol{q})$ is called the dynamical matrix and its matrix elements is defined by

$$D^{\alpha\beta}_{\mu\nu}(\boldsymbol{q}) = \sum_{\ell - m} V^{\alpha\beta}_{\ell\mu m\nu} \mathrm{e}^{\mathrm{i}\boldsymbol{q}\cdot(\boldsymbol{R}_\ell - \boldsymbol{R}_m)}. \tag{2.2.4}$$

To combine the dynamical matrix and the ground state electronic band structure calculations, we adopt the density functional perturbation theory (DFPT) [33]. We can obtain the dynamical matrix $D(\boldsymbol{q})$ as follows. First we solve the Sternheimaer equation [34]

$$(-\nabla^2 + V_{\mathrm{eff}} - \varepsilon_{k\lambda})\delta\psi_{k\lambda} + \delta V_{\mathrm{eff}}\psi_{k\lambda} = 0, \tag{2.2.5}$$

where δV_{eff} is the first order change in the effective potential. Next we find the induced charge density according to

$$\delta\rho = \sum_{k\lambda} f_{k\lambda}(\delta\psi^*_{k\lambda}\psi_{k\lambda} + \psi^*_{k\lambda}\delta\psi_{k\lambda}), \tag{2.2.6}$$

where $f_{k\lambda}$ are the occupation numbers. Then we obtain the following expression for $\delta V_{\rm eff}$

$$\delta V_{\rm eff} = \delta V_{\rm ext} + e^2 \int \frac{\delta\rho'}{|\boldsymbol{r}-\boldsymbol{r}'|}{\rm d}\boldsymbol{r}' + \delta\rho\frac{{\rm d}\mu_{xc}}{{\rm d}\rho}, \tag{2.2.7}$$

where μ_{xc} denotes exchange correlation as in usual LDA. Note here, δA ($A = V_{\rm ext}$, ρ, μ_{xc}, and so on) represents the first order change of A with respect to the atomic displacement. For example $\delta V_{\rm ext}$ is given as

$$\delta V_{\rm ext} = \sum_{\mu}\{\boldsymbol{u}_{\mu}^{q}\delta^{+}V_{\rm ext} + \boldsymbol{u}_{\mu}^{q*}\delta^{-}V_{\rm ext}\}. \tag{2.2.8}$$

where

$$\delta^{\pm}V_{\rm ext} = \sum_{\ell}{\rm e}^{\pm{\rm i}\boldsymbol{q}\cdot\boldsymbol{R}_{\ell}}\frac{\partial}{\partial\boldsymbol{R}_{\ell\mu}}\frac{-Z_{\mu}{\rm e}^2}{|\boldsymbol{r}-\boldsymbol{R}_{\ell\mu}|}\bigg|_{\boldsymbol{R}_{\ell\mu}=\boldsymbol{R}^{0}_{\ell\mu}}. \tag{2.2.9}$$

Steps described by the above equations 2.2.5–2.2.7 are repeated until self consistency for $\delta\rho$ is fulfilled. Finally we obtain the dynamical matrix as follows:

$$\begin{aligned} D(\boldsymbol{q}) \;=\; & \sum_{k\lambda} f_{k\lambda}\langle\delta^{+}\delta^{-}\psi_{k\lambda} + \delta^{-}\delta^{+}\psi_{k\lambda}|\mathcal{H}-\varepsilon_{k\lambda}|\psi_{k\lambda}\rangle \\ & + \sum_{k\lambda} 2f_{k\lambda}\langle\delta^{+}\psi_{k\lambda}|\mathcal{H}-\varepsilon_{k\lambda}|\delta^{-}\psi_{k\lambda}\rangle + \int\delta^{+}V_{\rm ext}\delta^{-}\rho{\rm d}\boldsymbol{r} \\ & + \int\delta^{+}\delta^{-}V_{\rm ext}\rho{\rm d}\boldsymbol{r} + \int\delta^{+}V_{\rm eff}\delta^{-}\rho{\rm d}\boldsymbol{r}. \end{aligned} \tag{2.2.10}$$

where $\delta^{\pm}\delta^{\mp}\psi_{k\lambda}$ represents the second order change of the basis function $\psi_{k\lambda}$ with respect to the atomic displacement. A more detailed description of the LR-LMTO method is given in Appendix A.2.

Chapter 3

Electronic Structure and Magnetism of Molecular Phase of Oxygen

3.1 Introduction

In order to get an insight into pressure-induced insulator-metal transition in solid oxygen at low temperature we have carried out band structure calculations for three types of crystal structure of molecular phase by changing the volume: monoclinic α-phase, orthorhombic δ-phase and monoclinic ζ-phase. The crystal structure parameters of these three phases observed experimentally at a particular pressure are given in Table 3.1. There is a speculation [8] that in the ζ-phase the molecular axis may not be parallel to

Table 3.1: The crystal structure parameters of the α-phase at P=0 GPa (ambient pressure [35], the δ-phase at P=9.6 GPa [36] and the ζ-phase at P=116 GPa [8]. The data are taken at $T = 22$K for the α-phase and at room temperature for the δ- and ζ-phases.

	P (GPa)	a (Å)	b (Å)	c (Å)	β (deg.)	V_M (Å^3/molecule)
α [35]	0	5.403	3.429	5.086	132.3	34.85
δ [36]	9.6	4.214	2.957	6.689	122.2	20.84
ζ [8]	116	3.432	2.218	3.332	116.4	11.36

the z-axis (direction perpendicular to the ab-plane). For simplicity, however, we assume the molecular axis is parallel to the z-axis. The actual crystal structures are presented in Fig. 1.1.3 and Fig. 1.1.4. The first Brillouin zone (BZ) of the α-phase is shown in Fig. 3.1.1

In changing the molecular volume V_{M} we have fixed the mutual ratio of the lattice constants and the angle β of the monoclinic structure to the values determined from Table 1. Further the intramolecular atomic distance has been kept to be 1.2 Å which corresponds to that at ambient pressure. It should be noted here that in order to determine the pressure for each phase we have to optimize the lattice constants, the intramolecular atomic distance and the monoclinic angle for each volume in calculating the total energy. Therefore in our present calculation for molecular phases of solid oxygen we cannot determine precisely the pressure.

The actual calculations have been done by the FP-LMTO method based on the usual local spin-density approximation. The calculational details are given in section 3.2.

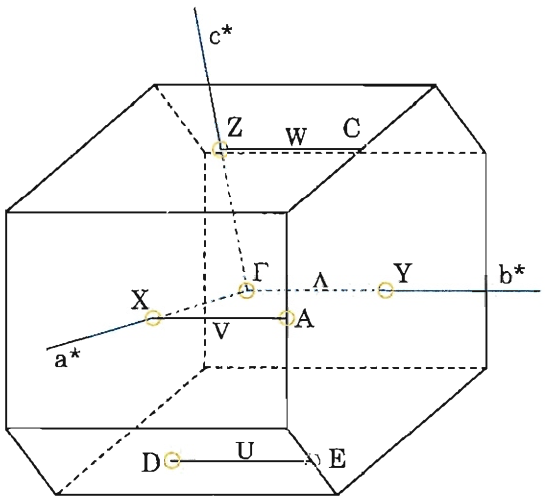

Figure 3.1.1: The fisrt Brillouin zone of the α-phase.

3.2 Detailed procedure of FP-LMTO calculations

Calculations of electronic structures of molecular phases of solid oxygen have been done according to the following procedure with use of FPLMTO program version 1.35.

For exchange-correlation functional we have adopted the formula proposed by Gunnarsson and Lundqvist [37] without GGA correction. Inside the MT spheres the scalar-relativistic calculations are performed for valence electrons, and the core states are recalculated at each self-consistent iteration with relativistic effects. The MT radius has been taken to be 0.54 Åwhich corresponds to 45 % of the intramolecular atomic distance. The $\boldsymbol{k}$-space integration has been performed by the improved tetrahedron method [38] with use of 68 sampling $\boldsymbol{k}$ points in the irreducible Brillouin zone (IBZ). We have used 3κ-sp-LMTO basis set (12 LMTO/atom): κ^2=-0.102, κ^2=-1.002 and κ^2=-2.002 Ryd. In the interstitial region the basis functions are expanded in plane waves. The charge densities and the potentials are expanded inside the MT spheres by spherical harmonics up to ℓ_{max} = 6 and in the interstitial region by plane waves with cutoff corresponding to 1,003 plane waves. The final convergence is within 10^{-6} Ryd.

3.3 Results of calculation

3.3.1 Electronic band structure at ambient pressure

First we have performed band structure calculations for the antiferromagnetic (AF) and the ferromagnetic (F) states of α-O_2 at ambient pressure. We have found that the AF state is more stable than the F state and the band structure of the AF state is insulating with an indirect energy gap $\sim$1eV. The obtained band structure and the density of states (DOS) of the AF state are depicted in Figs. 3.3.1 (a) and (b), respectively. A schematic diagram of electronic state of an O_2 molecule is shown in Fig. 3.3.1 (c). Note here that since α-O_2 has two molecule in a unit cell we have drawn each orbital twice. The magnetic moment inside the MT sphere is evaluated to be $\sim 0.5\mu_B$, and as will shown later, character of a free oxygen molecule is kept in the α-phase at ambient pressure.

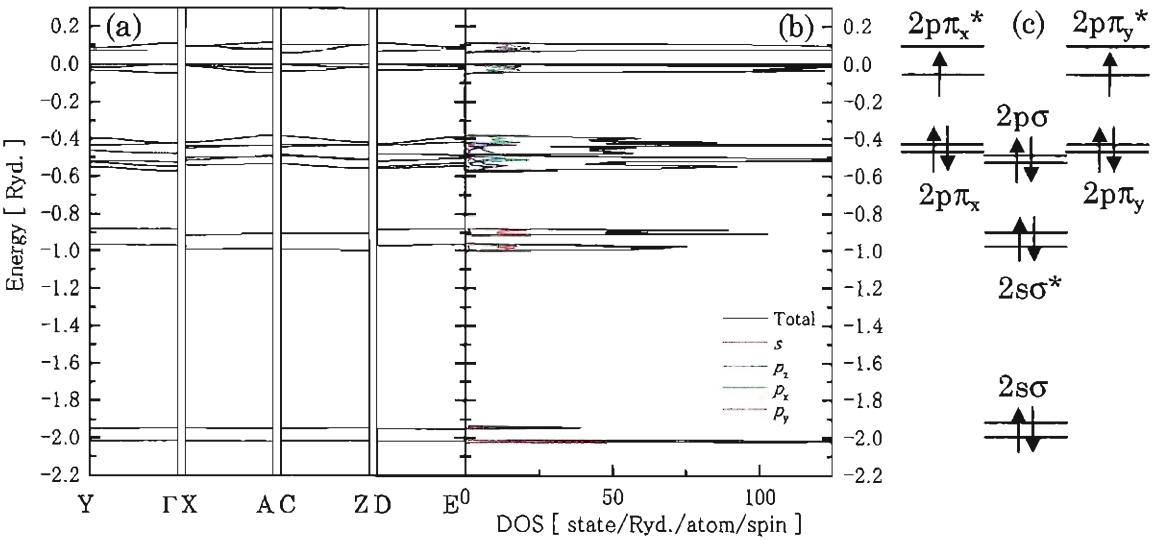

Figure 3.3.1: (a) the band structure and (b) the DOS calculated for the AF state of α-O_2 at ambient pressure. (c) a schematic diagram of electronic state of an oxygen molecule.

3.3.2 Insulator-metal transition

Secondly, we have calculated the volume dependence of the electronic band structure, the total energy, the magnetic moment inside the MT sphere and the DOS at the Fermi energy (ε_F) for the nonmagnetic (NM) state as well as for the AF and F states. Since the results obtained for the δ- and ζ-phases are essentially the same as those for the α-phase, in the following we give only the results obtained for the α-phase.

Fig. 3.3.2 shows the volume dependence of the total energies of the NM, the F and the AF states of the α phase, and the magnetic moments within the MT sphere in both the F and the AF states are given as a function of the molecular volume in Fig. 3.3.3. Figure. 3.3.4 shows the volume dependence of DOS at ε_F. As seen from Figs. 3.3.2, 3.3.3 and 3.3.4, the AF state is the most stable for a wide range of volume. For volumes larger than 25.98 Å^3 an insulating states are realized in the AF states, and the full magnetic moments are induced. With decreasing the volume the magnetic moments decrease and both the AF and the F states merge into the NM state.

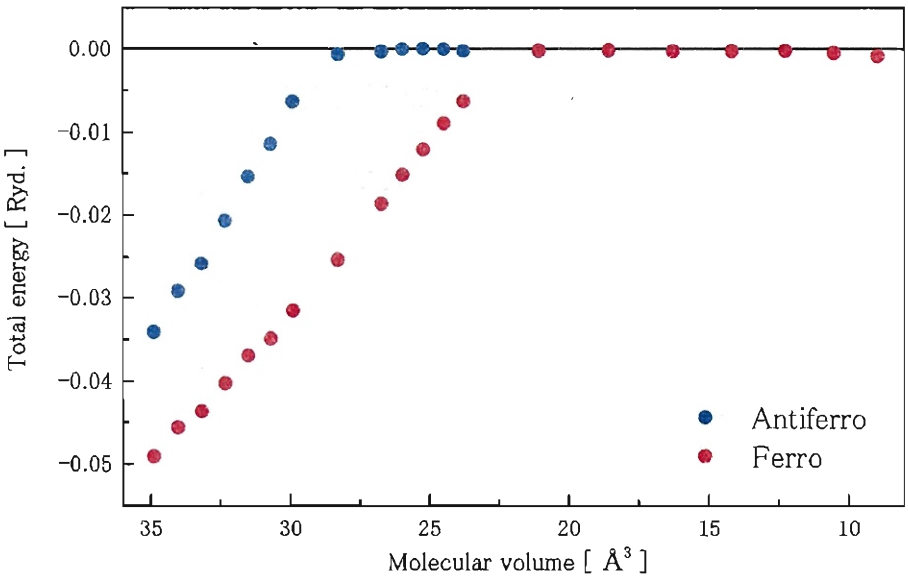

Figure 3.3.2: The volume dependence of the total energy of the AF and the F states of the α-phase. All the energies are referenced to the NM state.

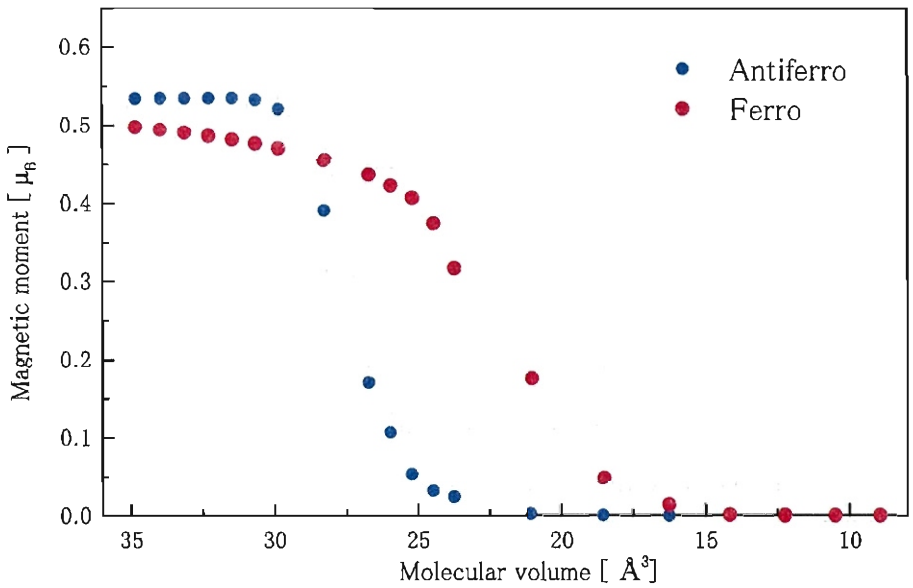

Figure 3.3.3: The volume dependence of the magnetic moments within the MT sphere in the AF and the F states of the α-phase.

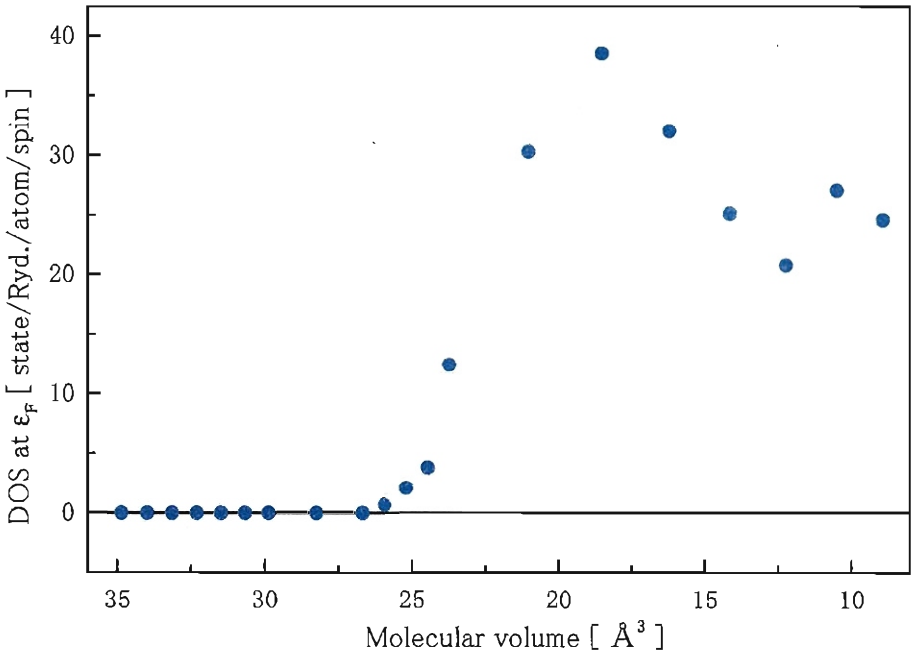

Figure 3.3.4: The volume dependence of the DOS at the Fermi energy of the α-phase.

Figure. 3.3.5(a) and (b) show the energy dispersion curves of the AF state calculated for $V_M = 34.85$ Å^3 (insulating) and $V_M = 25.98$ Å^3 (metallic), respectively. As for the F state, we obtain insulating states for $V_M > 30.67$ Å^3 and metallic states for $V_M < 30.67$ Å^3. For $V_M < 14.14$ Å^3 we could not obtained self-consistent solution also for the F state, *i.e.* we obtain only the NM state for $V_M < 14.14$ Å^3. Figures 3.3.5(c) and (d) show the energy dispersion curves of the F state obtained for $V_M = 34.85$ Å^3 (insulating) and $V_M = 25.98$ Å^3 (metallic), respectively, and Fig. 1(e) depicts the energy dispersion of the NM state obtained for $V_M = 11.36$ Å^3 corresponding to the molecular volume of the ζ-phase at 116 GPa. It should be emphasized here that the NM state is also metallic. Therefore, our present calculational results indicate strongly that solid oxygen would be a nonmagnetic metal under high pressures higher than about 100 GPa.

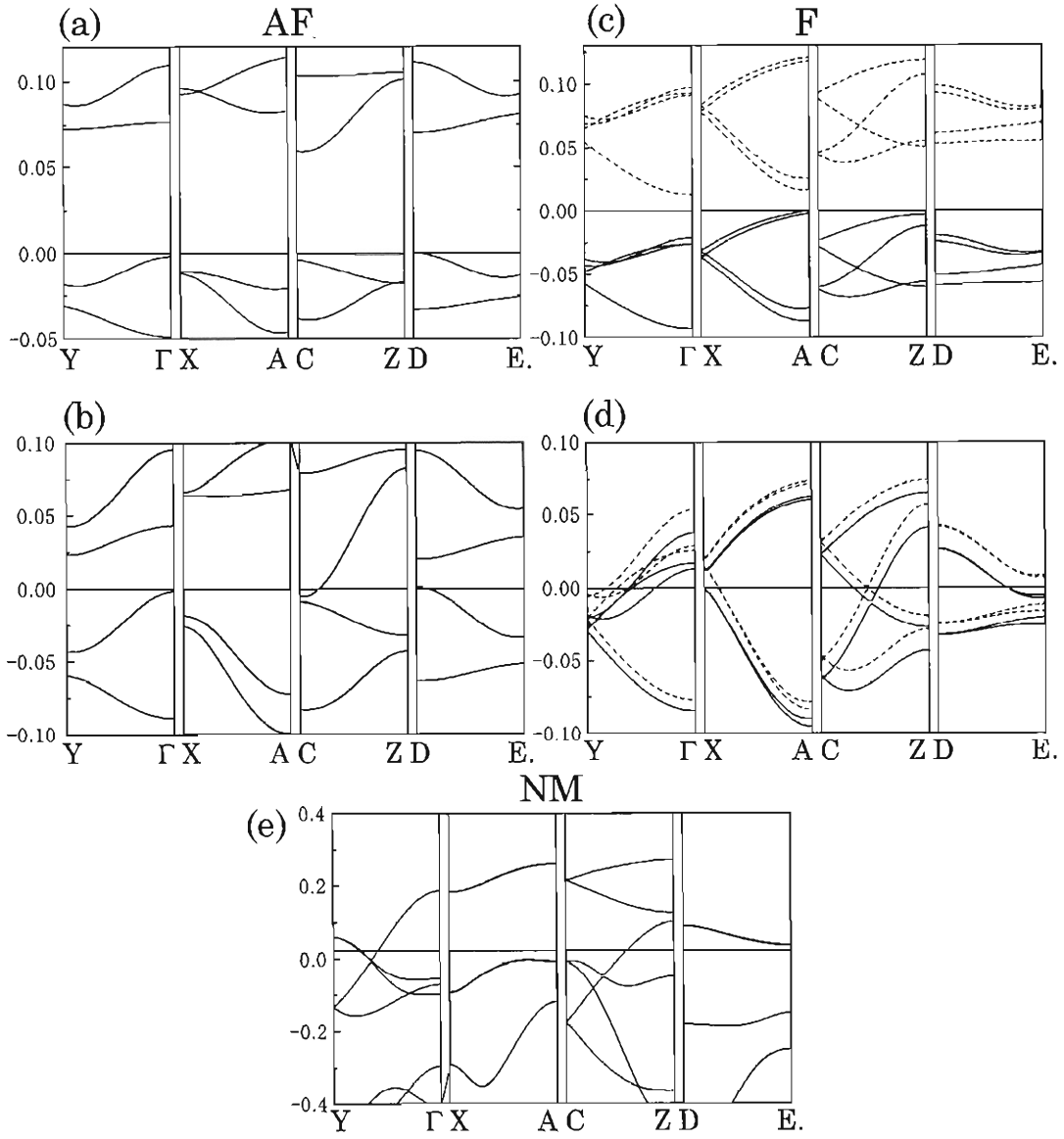

Figure 3.3.5: The energy dispersion curves of the α-phase along some symmetry lines in the first Brillouin zone: (a) AF state, $V_M = 34.85$ Å^3; (b) AF state, $V_M = 25.98$ Å^3; (c) F state, $V_M = 34.85$ Å^3; (d) F state, $V_M = 25.98$ Å; (e) NM state, $V_M = 11.36$ Å. In (c) and (d), the full curves denote the up-spin bands, and the dotted curves the down-spin bands. Note that in the AF state the up-spin and down-spin bands are degenerate.

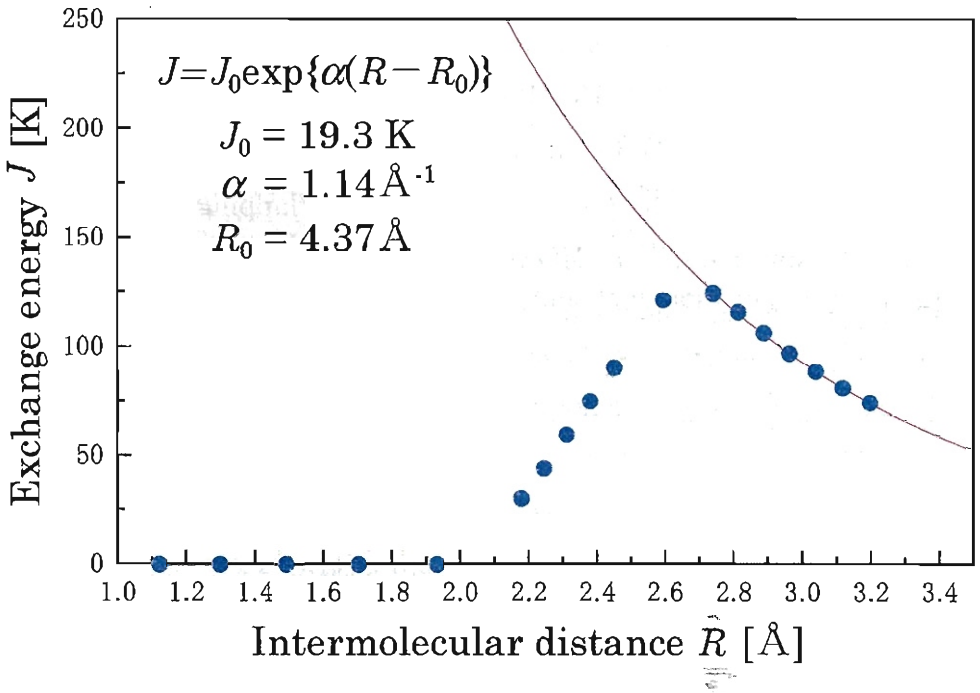

Figure 3.3.6: The exchange energy as a function of intermolecular distance. The red line shows a curve corresponding to the fitting function $J = J_0\exp\{\alpha(R - R_0)\}$.

From the total energy difference between the F and AF states we have evaluated the exchange coupling between the nearest neighboring oxygen molecules by assuming the Heisenberg Hamiltonian for the oxygen spins in the *ab*-plane. The exchange constant J estimated as a function of the molecular distance R is shown in Fig. 3.3.6. For larger R, J is well expressed by $J = J_0\exp\{\alpha(R - R_0)\}$ with J_0=19.3 K, α=1.14 Å^{-1} and R_0=4.37 Å. For R smaller than 2.38 Å, metallic state is realized and the assumption of Heisenberg Hamiltonian itself loses its meaning.

3.3.3 Charge and spin density map

To visualize the insulator-metal transition and the collapse of magnetism we have calculated the charge and spin density map of AF α-O_2 as a function of volume.

Figure. 3.3.7 shows the charge and spin density map of α-O_2 at V_M=34.85 Å^3 and 29.79 Å^3. At V_M=34.85 Å^3 the charge is well localized on the molecule, and character of

a free molecule is clearly seen. The spin moment is induced on each oxygen atom and the shape of the spin density contour well represents the $2p\pi^*$ molecular orbital which is the highest occupied molecular orbital (HOMO).

Fig. 3.3.8 shows the charge and spin density map at V_M=25.93 Å^3 and 11.36 Å^3. At V_M=25.93 Å^3 the metallization has occurred by band overlapping. However, we can still recognize clearly the spin moment at HOMO. Finally, at V_M=11.36 Å^3, the spin moment on a molecule disappears and the nonmagnetic metallic state is realized.

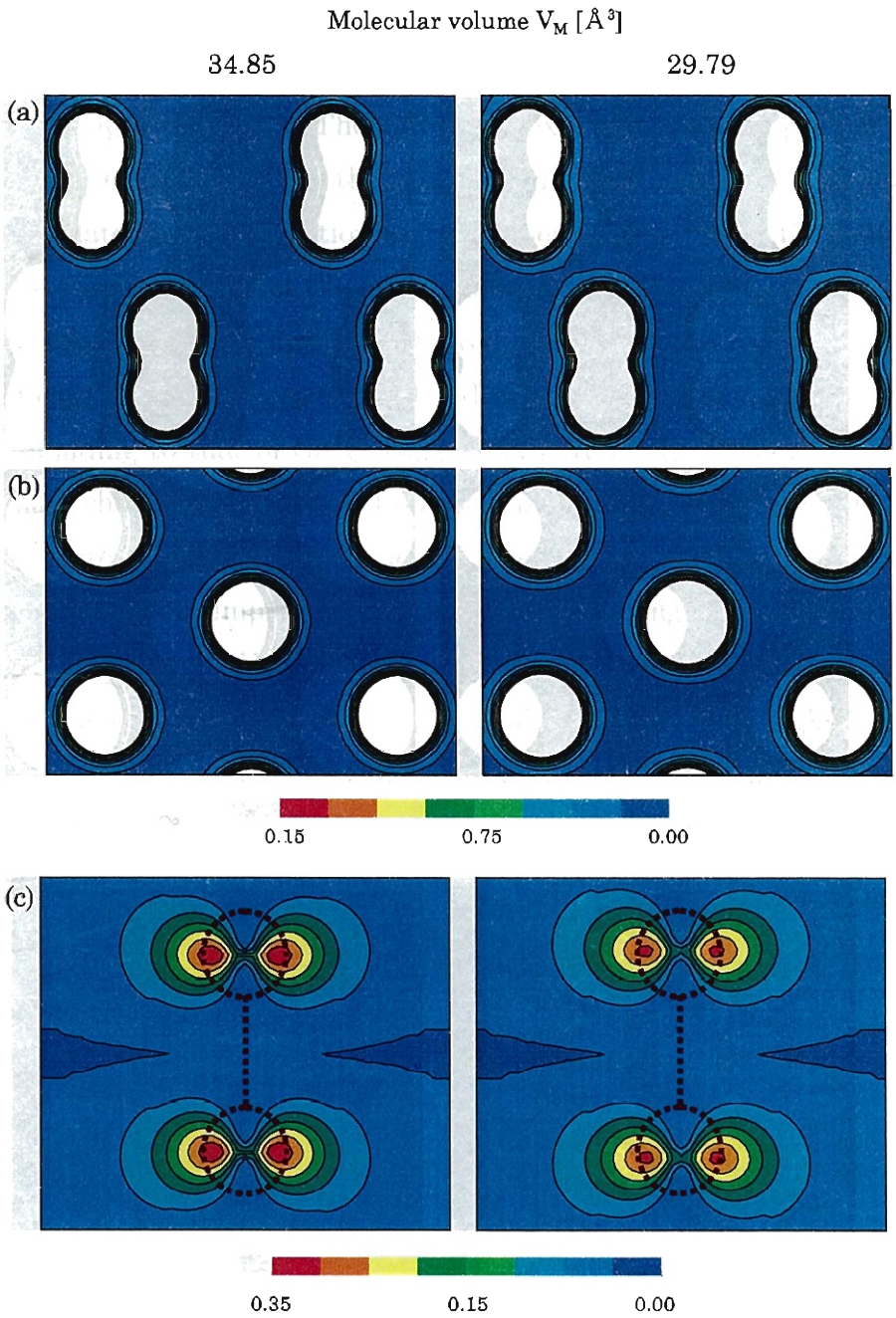

Figure 3.3.7: The charge density map [(a) and (b)] and the spin density map [(c)] of AF α-O_2 at V_M=34.85 Å^3 and 29.79 Å^3. (a) and (b) represent views perpendicular to the *ac*-plane and the *ab*-plane, respectively. The dotted line and circles in (c) illustrate a oxygen molecule schematically.

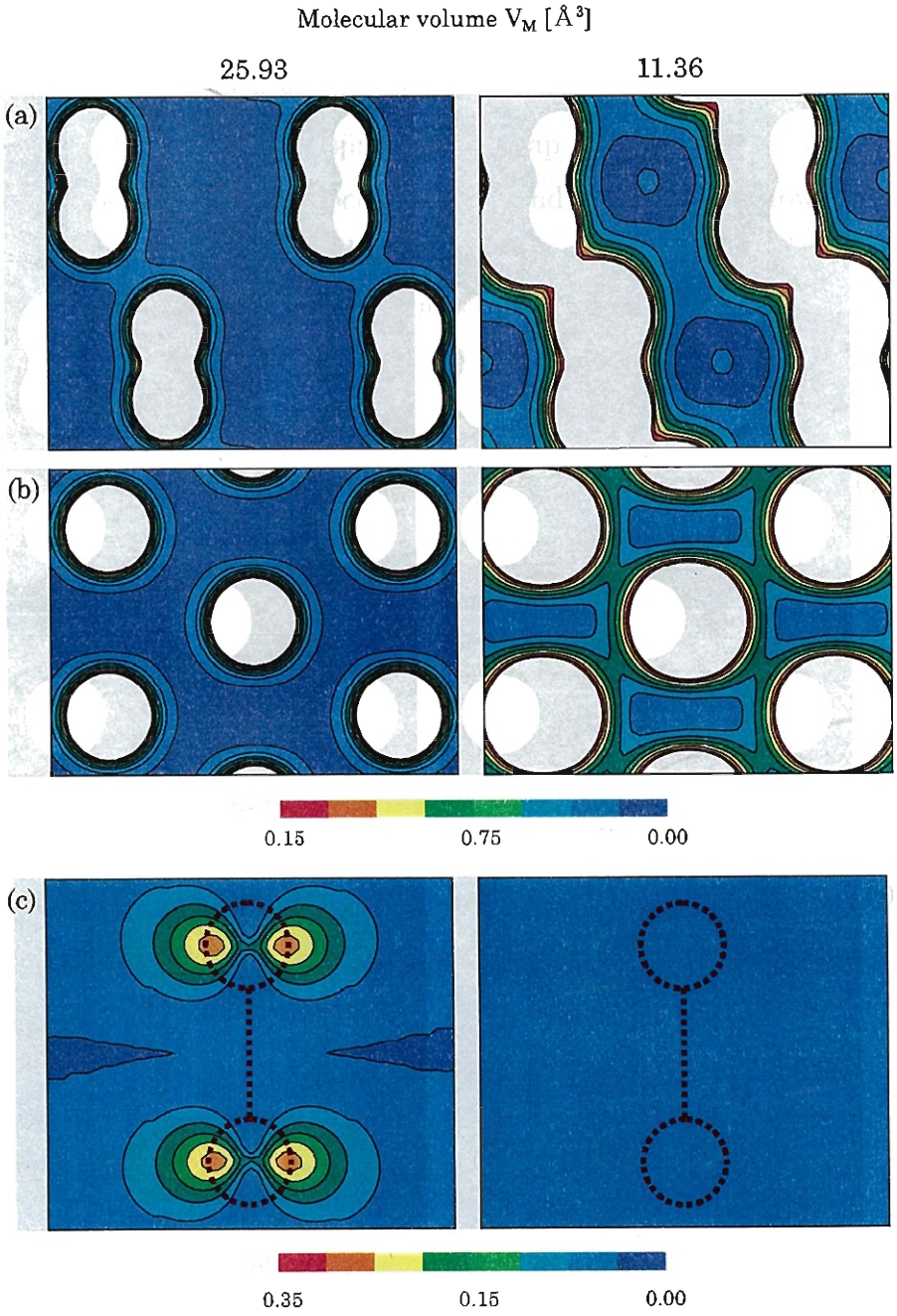

Figure 3.3.8: The charge density map [(a) and (b)] and the spin density map [(c)] of AF α-O_2 at V_M=25.93 Å^3 and 11.36 Å^3. (a) and (b) represent views perpendicular to the *ac*-plane and the *ab*-plane, respectively. The dotted line and circles in (c) illustrate a oxygen molecule schematically.

3.4 Discussion

We first note that our calculations have been done within the framework of the usual local spin-density approximation. Therefore, it is expected that the present calculations underestimate the energy gap and the magnetic moments. In order to obtain correct behaviors of insulator-metal transition and disappearance of magnetic moments it may be necessary to take into account the correlation effects.

In order to see a possibility that the observed metallization is realized in a monatomic phase of solid oxygen we have performed band calculations of monatomic phases for the volume corresponding to that of the ζ-phase at 116 GPa (V_M=11.36 Å^3). As the crystal structure we have chosen the β-Po type because it is the monatomic structure realized first under high pressures in other VI-b elements. The β-Po type structure is rhombohedral and can be described as a simple cubic lattice deformed along the [111] direction keeping the edge length unchanged. We have calculated the total energy as a function of c/a and obtained the minimum energy at c/a = 1.04 , and found that it is higher than the total energies of the δ(orthorhombic) and ζ(monoclinic) phases obtained for the same volume as shown in Fig 3.4.1. Therefore, judging from the results of our present calculations it is strongly suggested that a nonmagnetic metallic state is realized in molecular solid oxygen under high pressures higher than about 100 GPa.

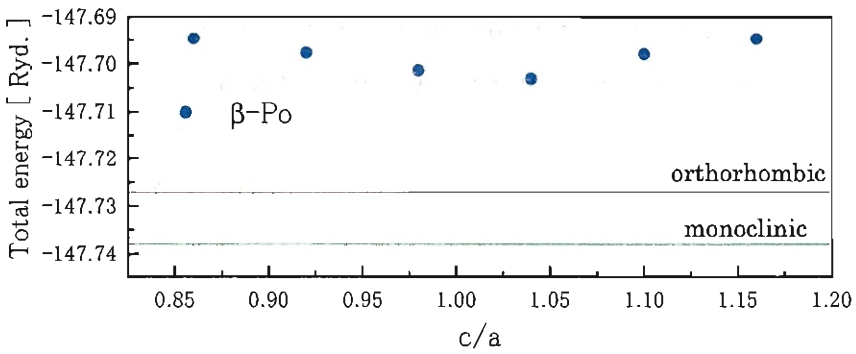

Figure 3.4.1: The c/a dependence of the total energy of the monatomic β-Po structure obtained for V_M=11.36 Å. The red and green lines denote the total energy of the δ- and ζ-phases, respectively, at the same molecular volume.

Chapter 4

Monatomic Phase of Selenium and Oxygen

4.1 Introduction

In this chapter we focus our attention on the electronic band structures of monatomic selenium and oxygen under high pressures. Monatomic selenium shows a pressure-induced structural phase transition from β-Po to bcc at 150 GPa [19]. The β-Po structure is shown in figure 4.1.1 together with the first Brillouin zone (BZ). The β-Po structure is rhombohedral and can be described as a simple cubic lattice deformed along the [111] direction keeping the edge length unchanged. By changing the ratio c/a (or the rhombohedral angle β) of the rhombohedral lattice we obtain the fcc structure, the sc structure and the bcc structure as shown in Table 4.1.

The experimental results show that the transition from β-Po to bcc causes a small

Table 4.1: The characteristic value of c/a and rhombohedral angle β.

	bcc	sc	fcc
c/a	$\sqrt{6}/4$	$\sqrt{6}/2$	$\sqrt{6}$
β (deg.)	109.47	90	60

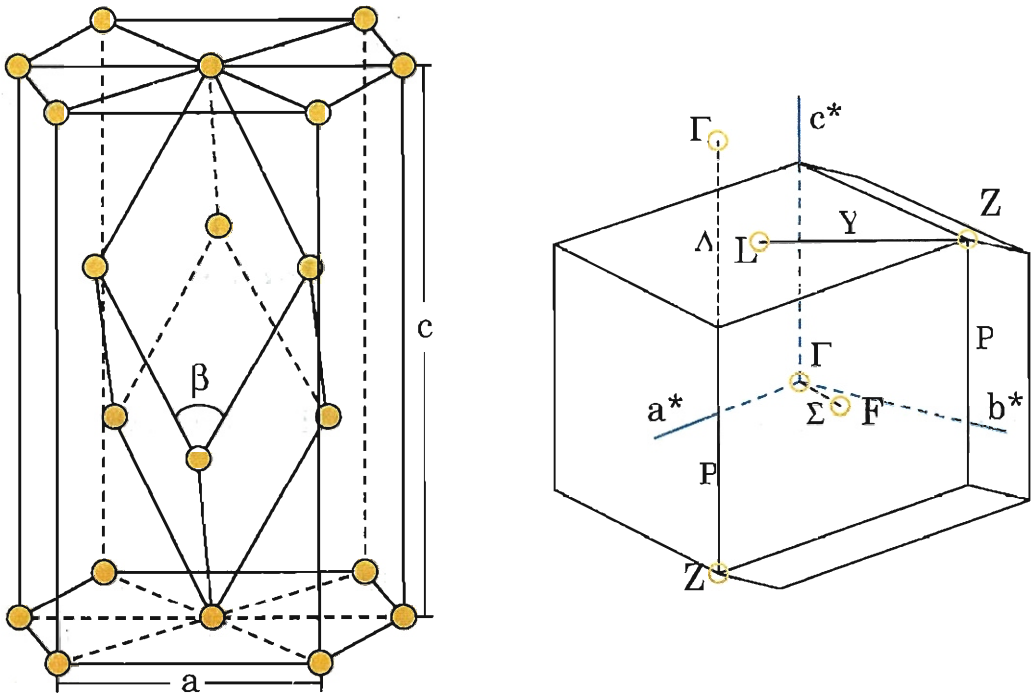

Figure 4.1.1: The crystal structure (left) and the first BZ (right) of β-Po type. β denotes the rhombohedral angle. Note that if the β-Po type structure transforms to the bcc structure, the point L and F of the rhombohedral BZ become the equivalent point, *i.e.*, the symmetry point N of BZ of bcc, the point Z becomes the symmetry point H of the bcc structure, and the contact point of the P and Λ lines the symmetry point P.

volume constriction and discontinuity of c/a with precursor behavior of decrease in c/a. Thus the transition is understood as a first-order transition. Theoretically, a couple of calculations have been done for this transition by using the FLAPW method [39] and the pseudo-potential method [40]. However, they underestimate the transition pressure(P_c), *i.e.*, 90 GPa [39] and 110 GPa [40].

In this chapter we first calculate the electronic structures of monatomic selenium by adopting FPLMTO method with gradient correction in order to try to improve the underestimation of P_c. Further this calculation is the first step to investigate the superconducting properties of monatomic Se in the following chapter. Secondly, we explore the monatomic phase of oxygen. Since the monatomic phase has never been observed

experimentally yet for solid oxygen, we have chosen the β-Po structure and all the cubic structures (fcc, bcc, sc) because the phase transition from β-Po to bcc has been observed or predicted in other VI-b elements. In Se and Te the bcc structure is the final phase in the pressure region accessible experimentally at present.

4.2 Computational details of calculations

The calculations of electronic states for the β-Po and bcc structures of Se and O have been done according to the following procedure with use of FPLMTO program version 3.12. For exchange-correlation functional we have adopted the formula proposed by Gunnarsson and Lundqvist [37] and the GGA correction proposed by Perdew *et. al.* [41] has been taken into account. Inside the MT spheres the scalar-relativistic calculations are performed for valence electrons, and the core states are recalculated at each self -consistent iteration with relativistic effects. The MT radius has been taken to be 1.07 Å for Se and 0.89 Å for O. The $\boldsymbol{k}$-space integration has been performed by the improved tetrahedron method [38] with use of (12, 12, 12) grid of the sampling $\boldsymbol{k}$-points [189 points in the IBZ]. We have used 3κ–*spd*–LMTO basis set (27 orbitals): $\kappa^2 = -0.1$,-1.0 and -2.0 Ryd. In the interstitial region the basis functions are expanded in plane waves up to the cutoff approximately corresponding to 200, 350 and 650 plane waves per s, p, and d orbitals, respectively. The charge densities and the potentials are expanded inside the MT spheres by spherical harmonics up to $\ell_{\max}$=6 and in the interstitial region by plane waves with the cutoff corresponding to the (16, 16, 16) fast-Fourier-transform(FFT) grid in the unit cell of direct space. The final convergence is within 10^{-6} Ryd.

We have checked out the total energy convergence with respect to the some variational freedom such as the number of plane waves and the number of sampling $\boldsymbol{k}$-points. For example, the total energy convergence with respect to the number of plane waves is shown in Fig 4.2.1. The convergence within 0.2mRyd is obtained over (16, 16, 16) FFT grid. Figure 4.2.2 shows the total energy convergence with respect to the number of sampling $\boldsymbol{k}$-points and the convergence within 0.2mRyd is obtained over 189 $\boldsymbol{k}$-points in the IBZ.

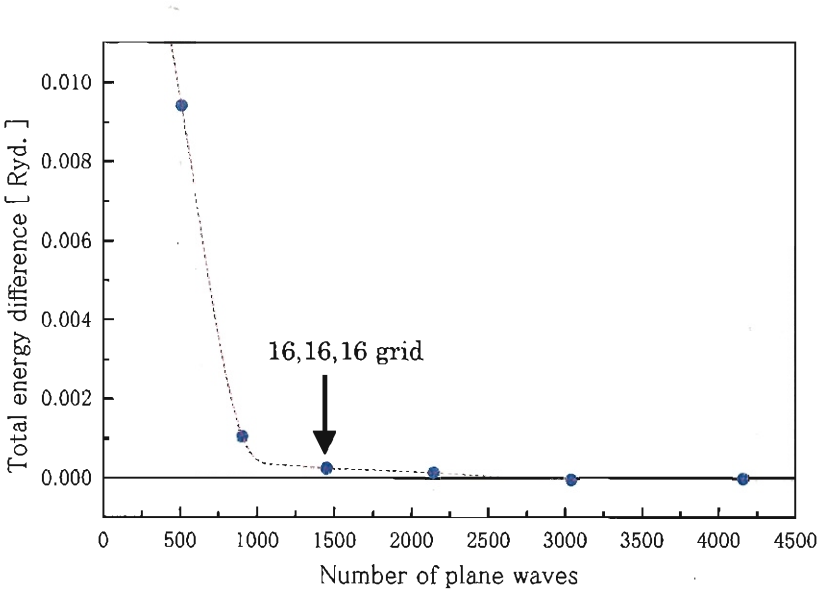

Figure 4.2.1: The total energy of monatomic β-Po Se versus number of plane waves to expanded densities. The broken line is just a guide to eyes. The number of plane waves is selected with the (16, 16, 16) FFT grid in the unit cell of direct space.

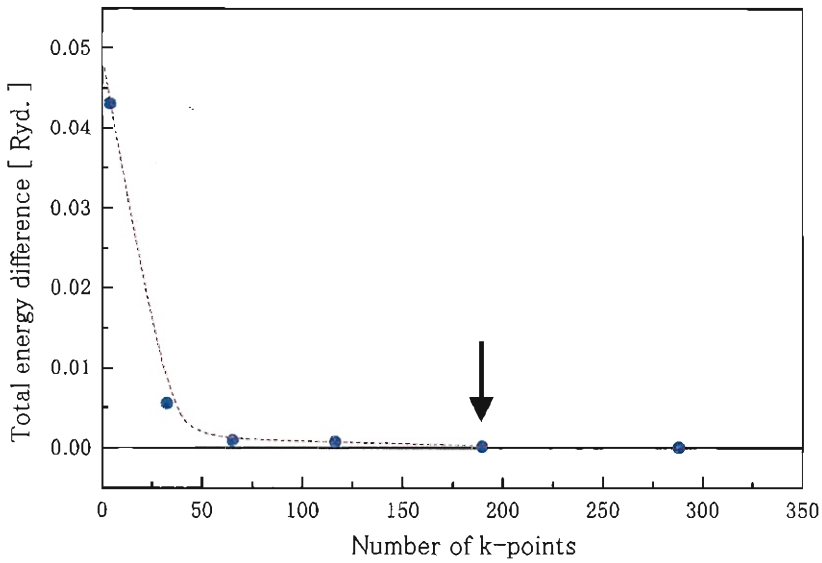

Figure 4.2.2: The total energy of monatomic β-Po Se versus number of sampling $\boldsymbol{k}$-points inside IBZ. The broken line is just a guide to eyes. The number of $\boldsymbol{k}$-points is selected at 189 points.

4.3 Results for monatomic selenium

As the first step to investigate the phase transition from β-Po to bcc we have calculated the electronic band structure and the total energy of the β-Po structure of selenium at atomic volume V_A=14.82Å. At this volume the β-Po structure is known to be stable by experimental measurements. For comparison we have calculated the electronic band structure and the total energy of the hypothetical bcc structure with the same atomic volume. The calculated energy band structures and the DOS for the β-Po and the bcc structures are shown in Fig. 4.3.1. The lowest band is mainly derived from the 4*s* component and the next three bands from the 4*p* component. Basically, the band structures of both the structures are similar to each other on the whole. However, remarkable difference can be seen in the band structure and the DOS near the Fermi level. First the band structure of the bcc structure along the P and Λ lines has much larger dispersion than that of the β-Po type structure. Secondly the DOS at the Fermi level of the bcc structure is larger than that of the β-Po structure because in bcc Se the L point is a saddle point of the third energy band from the bottom which crosses the Fermi level near the L point. By deforming from bcc to β-Po the L point energy of the third band goes up away from the

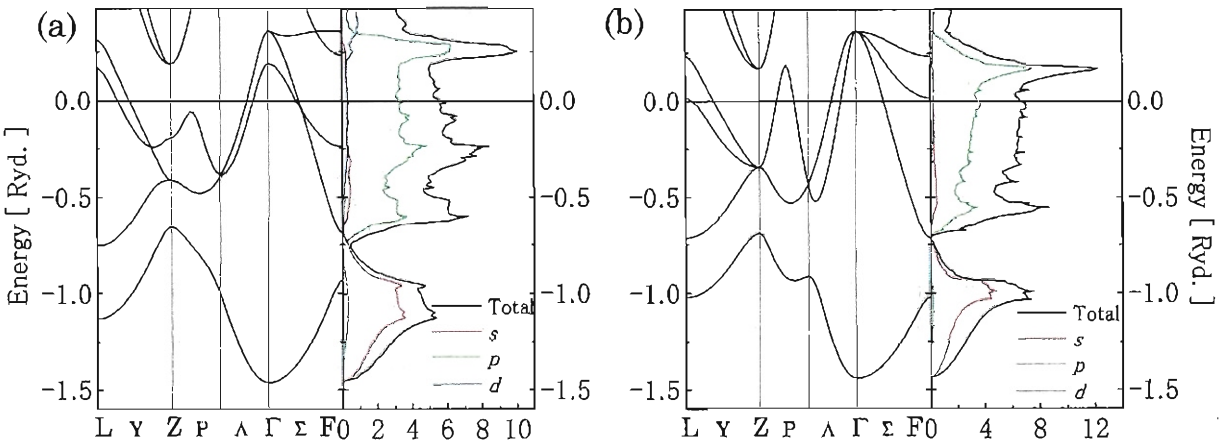

Figure 4.3.1: The band structure and the density of states of Se at atomic volume V=14.82 Å: (a) β-Po type structure and (b) bcc structure. The horizontal line denotes the Fermi level.

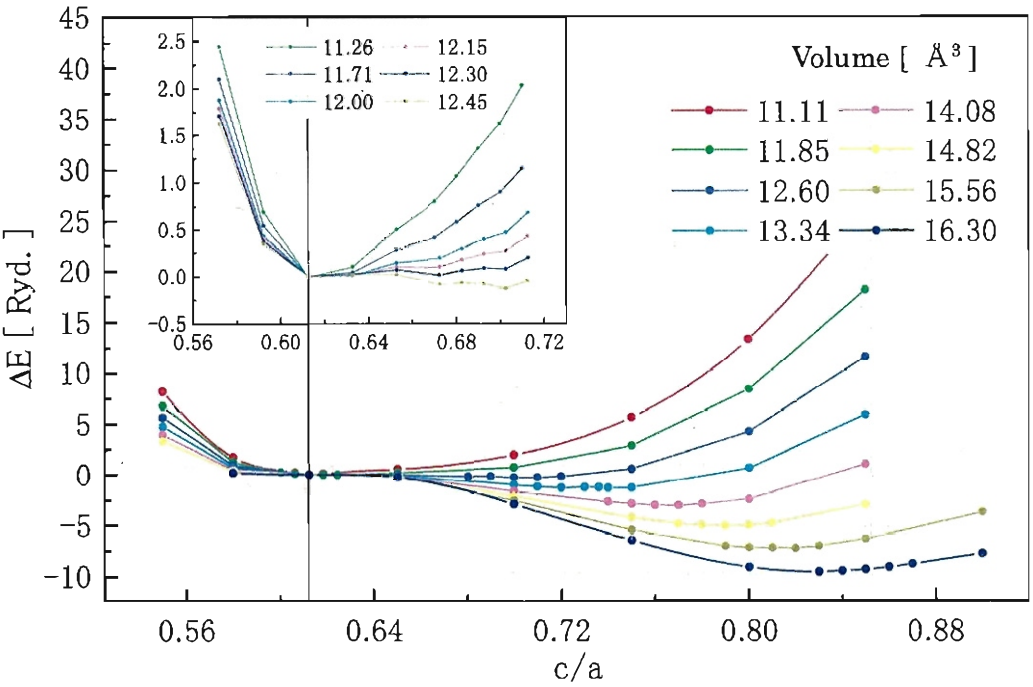

Figure 4.3.2: The total energy of β-Po Se as a function of c/a for the fixed atomic volume. The inset indicate the results for volumes near the phase transition. All the energies are referenced to the bcc structure, *i.e.* ΔE—E-$E_{\rm bcc}$.

Fermi level and the states of the fourth band in the middle of the P line comes down under the Fermi level. As the results the DOS of β-Po Se has a relatively large peak at 0.225 Ryd below the Fermi level. This is the reason why the β-Po type structure is relatively stable compared with the bcc structure.

To investigate the pressure-induced structural transition we have to calculate the total energy of the β-Po and the bcc structures as a function of volume. For the β-Po structure we have optimized c/a at each volume, namely, we have calculated the total energy of the β-Po type Se as a function of c/a with the atomic volume $V_{\rm A}$ being kept constant. Figure 4.3.2 shows a total energy *vs* c/a for several fixed atomic volume and the inset shows results for a volume range near the phase transition. All the energies are referenced to the bcc structure, *i.e.*, at the energy of c/a=$\sqrt{6}/4$. For a large volume such as 16.30 Å^3 the energy takes the minimum at $c/a \sim 0.85$ and the bcc structure is an inflection point.

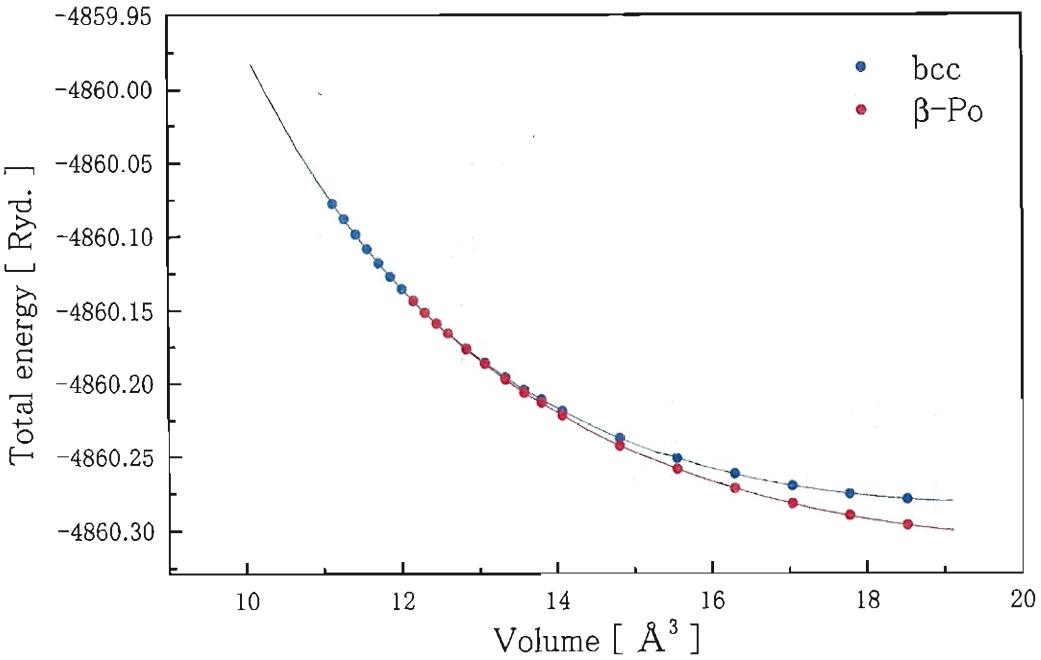

Figure 4.3.3: The total energy calculated as a function of volume for the β-Po and the bcc structures of Se. The lines are obtained by using Murnanghan's equation of state.

With decreasing the volume the value of the c/a starts to decrease gradually toward the bcc structure. Finally, the β-Po structure is no longer quasistable structure, that is, the total energy has single minimum at c/a=$\sqrt{6}/4$ corresponding to the bcc structure.

We have calculated also the total energies of the β-Po and the bcc structures as a function of the atomic volume. Figure 4.3.3 shows the total energy of the β-Po and the bcc structures of Se as a function of volume. As seen from the figure, at larger volumes the β-Po structure is certainly more stable than the bcc structure. At smaller volumes the total energies of both the structures take quite close values, but if we enlarge the energy scale of Fig. 4.3.3 we can recognize that the bcc structure is more stable than the β-Po structure at volumes smaller than $\sim$ 12 Å^3.

In order to estimate the transition pressure from β-Po to bcc we need to calculate the Gibbs free energy (or enthalpy) as a function of pressure. Then, to evaluate the pressure as a function of volume we fitted the calculated total energies by the Murnaghan's equation

of state (EOS) [42]:

$$E(V) = \frac{B_0 V}{B_0'}\left[\frac{1}{B_0' - 1}\left(\frac{V_0}{V}\right)^{B_0'} + 1\right] + \text{const},$$

where B_0 and B_0' is the isothermal bulk modulus at zero pressure and it's derivative, respectively. The pressure is determined from

$$P = \frac{B_0}{B_0'}\ln\left[\left(\frac{V}{V_0}\right)^{-B_0'} - 1\right].$$

The Gibbs free energy is defined by $G(P) \equiv E_{\text{tot}}(P) + PV(P)$ and the transition pressure between the two phases is obtained from the relation $G_\beta(P) = G_{\text{b}}(P)$, where G_β and G_{b} are the Gibbs free energies of the β-Po and the bcc structures, respectively. Figure 4.3.4 shows the pressure dependencies of the atomic volume V_{A}, the lattice constants a and c, and the bond lengths r_1 and r_2 which are defined as the n.n. and next n.n. atomic distances, respectively. Note that in the bcc phase $c = \frac{\sqrt{6}}{4}a$, and $r_1 = r_2 = \frac{\sqrt{3}}{2}a$. The red and blue circles indicate the results of the present calculations and the black triangles and green inverse triangles represent the experimental values [19]. The solid and the dashed vertical lines indicate the boundary of the phase transitions determined theoretically by us and experimentally by Akahama *et.al.* [19], respectively.

The transition pressure P_{c} from β-Po to bcc has been estimated as 120 GPa by our present calculation. This value is higher than other calculated transition pressures, 90 GPa [39] and 110 GPa [40], but still lower than the experimental value 150 GPa [19]. The origin of this discrepancy between theory and experiment may be ascribed to LDA itself and/or numerical accuracy of the total energy. With respect to the latter point we note here that as seen from Fig. 4.3.3 the volume-energy curves for the two structures are almost parallel near the phase transition. Therefore a small change in the total energy for one of the phases is expected to cause a large change for the value of P_{c}. In fact, if the total energy of one of the two phases is shifted by 1 mRyd, the value of P_{c} changes by 20 GPa.

As seen from Fig. 4.3.4 the volume variation as a function of pressure below 120 GPa (β-Po) and above 150 GPa (bcc) shows good agreement with the observations [19]. Also the obtained pressure dependence of a, c and β of the β-Po phase agrees well with the

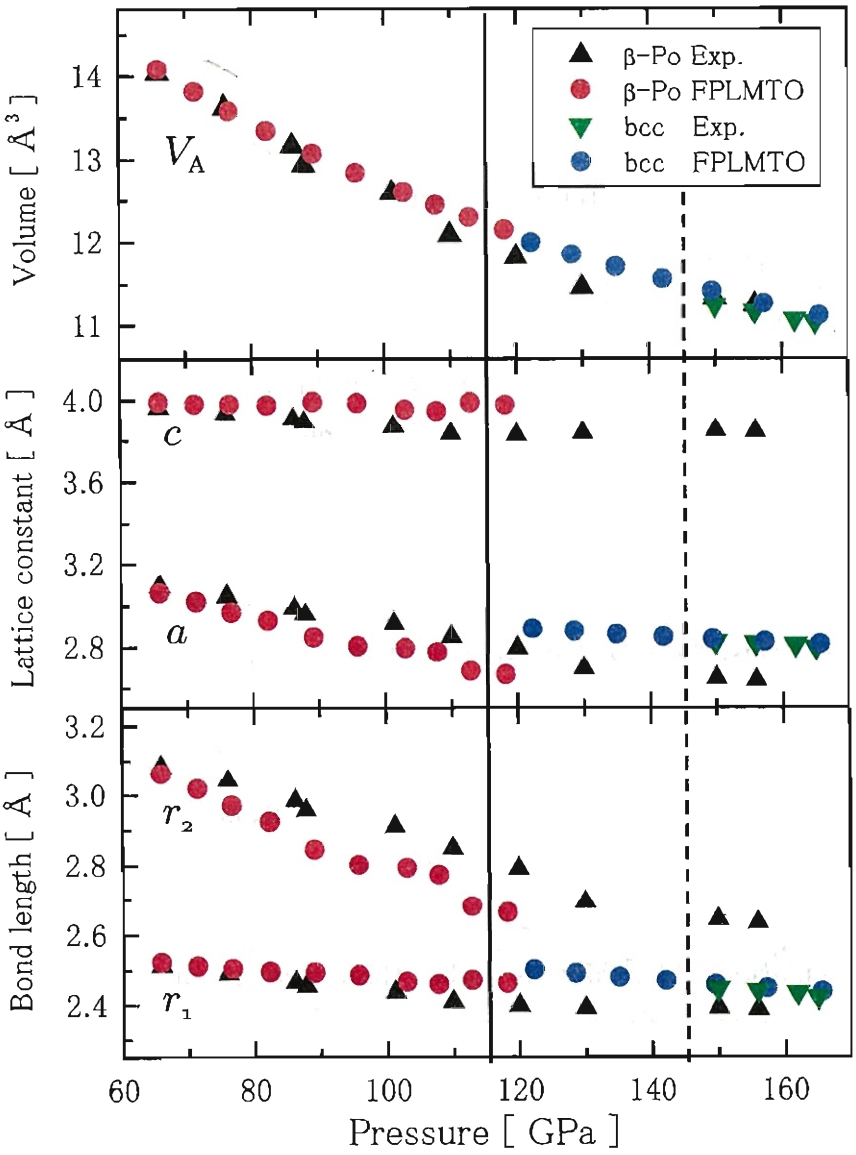

Figure 4.3.4: The pressure dependence of atomic volume, lattice constants and bond length of selenium. The red and blue circles indicate the results of the present calculations and the black triangles and green inverse triangles represent the experimental values [19]. The solid and the dashed vertical lines indicate the boundary of the phase transition from β-Po to bcc, determined theoretically by us and experimentally by Akahama *et.al.*, respectively.

experimental results [19]. Furthermore, the volume reduction at the transition from β-Po to bcc is estimated to be 0.06 Å^3, which is in good agreement with the experimental one (about 0.08 Å^3 [19]).

4.4 Results for monatomic oxygen

In Te, Se and S the β-Po structure is realized experimentally under high pressures and further the transition from β-Po to bcc has been observed at 27 GPa cite33 in Te and at 150 GPa [19] in Se. In S the transition pressure from β-Po to bcc is predicted to be 545 GPa [20]. However quit recently Rudin *et.al.* predict existence of simple cubic structure between the β-Po and bcc structures for S [21].

As for solid oxygen, however, the transition to a monatomic phase has never been observed yet. By expecting the β-Po structure being realized first in monatomic oxygen we have performed band structure calculations for β-Po oxygen and also for bcc oxygen. Figure 4.4.1 shows the total energy of β-Po type oxygen calculated as a function of c/a for

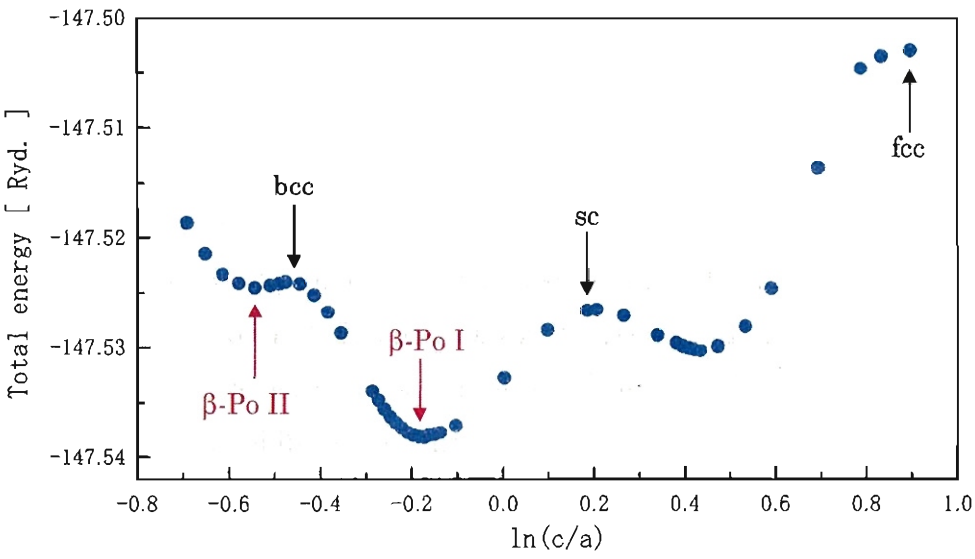

Figure 4.4.1: The total energy of β-Po type oxygen as a function of c/a for the atomic volume V_A=5.32Å^3.

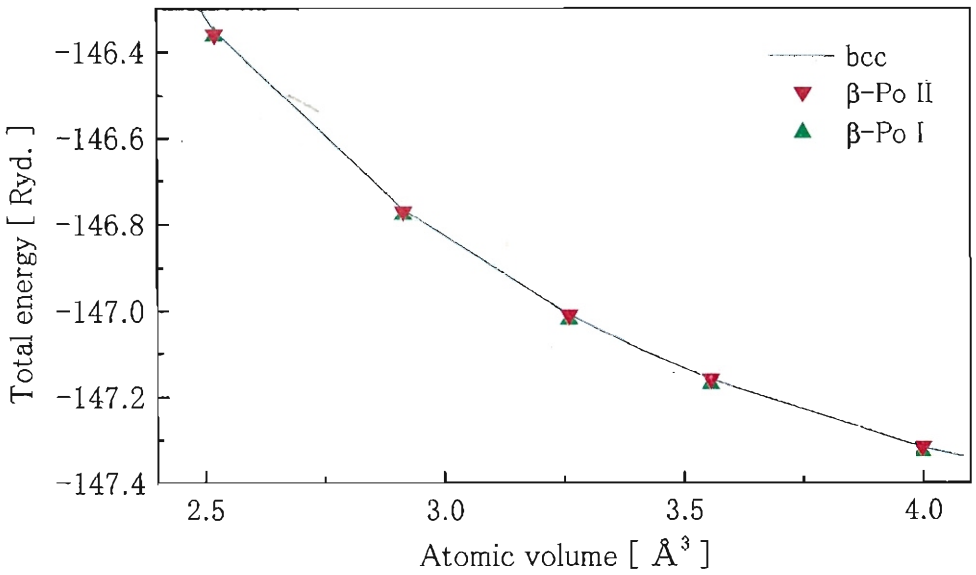

Figure 4.4.2: The total energies of the β-Po and the bcc structures as a function of the atomic volume.

V_A=5.32 Å^3 which corresponds to 160 GPa in the bcc phase. As seen from the figure there are two local minima: β-Po I and β-Po II, and the bcc, sc and fcc structures correspond to local maxima. Basically the shape of the total energy curve as a function of c/a is the same as that of selenium. However, the characteristic feature of oxygen is the existence of β-Po II. In any way, the β-Po structure is more stable than the cubic structures.

We have performed the calculations for smaller atomic volumes up to V_A=2.5 Å^3 which corresponds to more than 2 TPa in the bcc phase. We have plotted in Fig. 4.4.2 the total energies of the β-Po and the bcc structures as a function of volume. At larger volumes the total energies of bcc, β-Po I and β-Po II are in the order of β-Po I < β-Po II < bcc. With decreasing volume (increasing pressure) the energy difference between β-Po I and β-Po II becomes smaller, and then at V_A=2.5 Å^3 we obatin β-Po I $\simeq$ β-Po II < bcc. This may suggest that isostructural transition from β-Po I to β-Po II would occur. In any way the β-Po structure is always more stable than the bcc structure in the volume range of the present calculations. Therefore it is expected that transition from β-Po to bcc will be hard to occur in oxygen for the pressure region accessible by experiments.

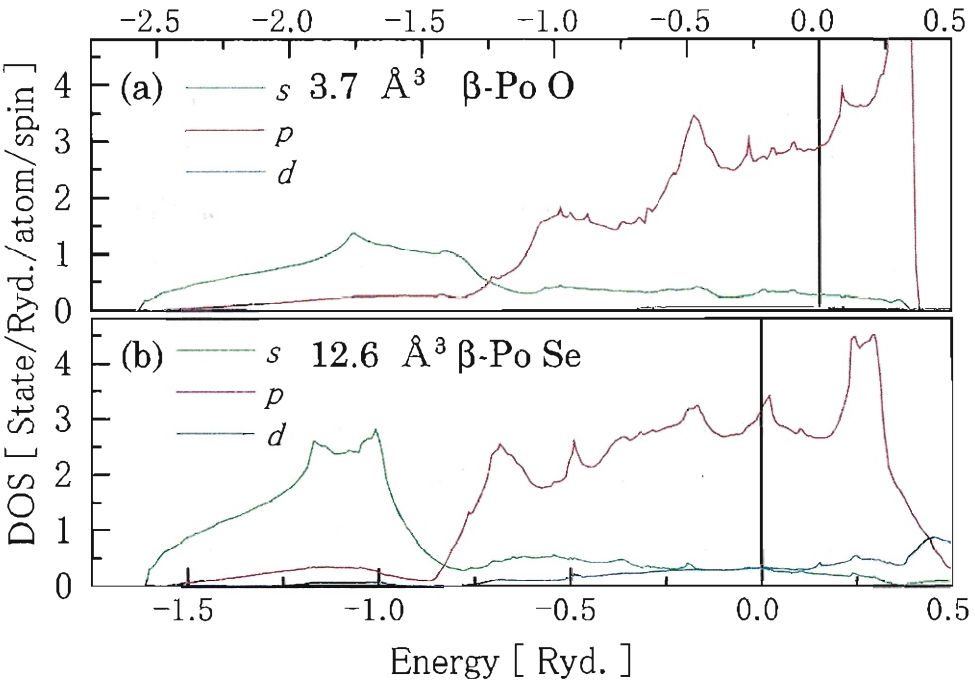

Figure 4.4.3: The partial DOS of (a) β-Po O and (b) β-Po Se. The upper window show the $2s$, $2p$ and $3d$ components for O and the lower ones the $4s$, $4p$ and $4d$ components for Se.

For comparison between the electronic structures of oxygen and selenium we show in Fig. 4.4.3 the partial density of states (DOS) obtained for O and Se with the β-Po structure, and in Fig. 4.4.4 the dispersion curves obtained for O and Se with the bcc structure. A quite important difference between O and Se is seen from Fig. 4.4.3, *i.e.* in Se the d-component is significantly included in the DOS at the Fermi level ε_F whereas in O the d-component is scarcely recognized near ε_F. The same difference is also seen between O and S or Te. In general, the more d-component is included, the stronger electron-lattice interaction is obtained. Therefore the electron-lattice interaction in monatomic phase of O is expected to be weak compared with that in other VI-b elements.

As seen from Figs. 4.4.4(a) and (b), the band structures of bcc Se and O are similar on the whole between (a) and (b). The lowest band is mainly derived from the s component, and the next three bands from the p component. In Figs. 4.4.4(c) and (d), on the other

hand, the s-p hybridization occurs considerably, and a remarkable difference is recognized in the band structures between O and Se. Namely, the locations of the s state and the three-fold degenerate p states are reversed at the symmetry point, Z. We consider the origin of this reversement as follows. In Se there exist the core $3s$ and $3p$ states which are orthogonal to the valence $4s$ and $4p$ states. In case of O, on the other hand, there exists certainly the core $1s$ state which is orthogonal to the valence $2s$ states whereas there is no core p state. As the result, with increasing pressure the $2p$ state of O can goes down beyond the $2s$ state because there is no repulsion from the core 'p' state. We are supposing that this peculiarity of oxygen may give rise to a structural sequence of monatomic phases different from other VI-b elements.

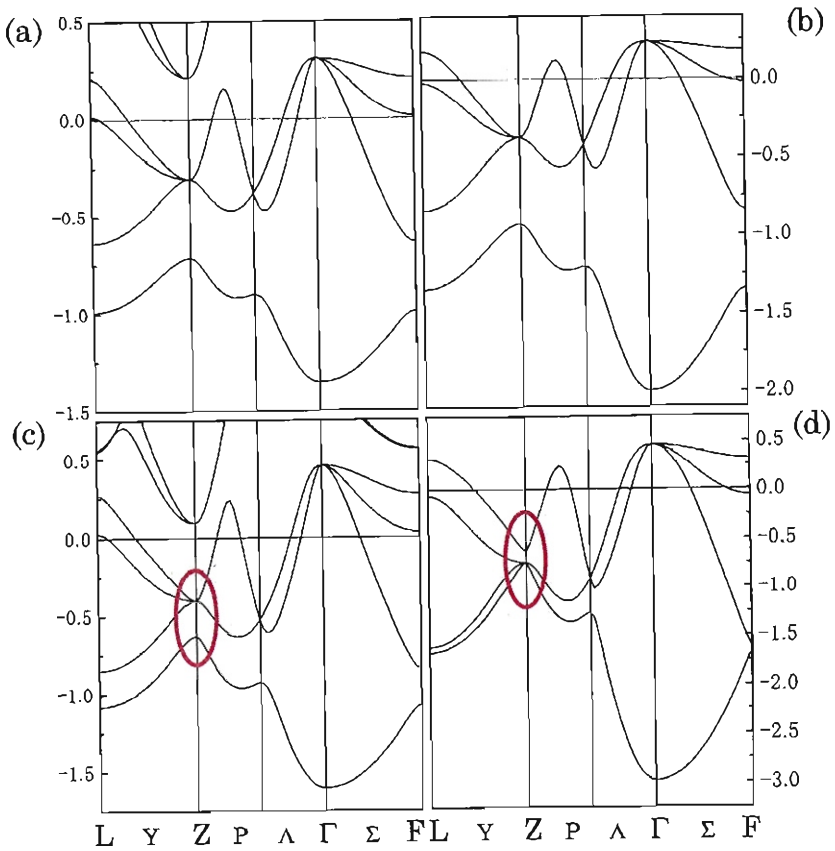

Figure 4.4.4: The energy dispersion curves of (a) bcc Se at V=16.3 Å^3 and (b) bcc O at V=5.2 Å^3, (c) bcc Se at V=12.6 Å^3 and (d) bcc O at V=3.0 Å^3.

Chapter 5

Lattice Dynamics and Superconductivity of Monatomic Selenium

Among VI-b elements, for monatomic bcc S the superconducting transition temperature T_c is predicted to be 15 K by Zakharov *et al.* [20], and for Te a jump in T_c from 2.5 K to 7.4 k has been observed at the phase transition from β-Po to bcc [16]. Mauri *et al.* have performed *ab initio* linear-response calculations for lattice dynamics of β-Po and bcc Te under pressures [24]. They reported that phonon anomaly for the transverse mode of bcc Te along the ΓN line in the first BZ. They have found that with decreasing pressure the phonon frequencies in the middle of the ΓN line become imaginary in a pressure region where the β-Po structure is stable. And they also succeeded in reproducing a jump in T_c at the phase transition from β-Po to bcc. As for Se there has been neither experimental nor theoretical study on superconductivity in its monatomic phases.

In this chapter we investigate lattice dynamics and superconductivity of monatomic β-Po and bcc selenium under high pressures. For calculation of lattice dynamics and electron-phonon interaction we use the linear-response LMTO method [31, 32], and the superconducting transition temperature T_c is calculated in the frame work of Allen-Dynes formalism [43].

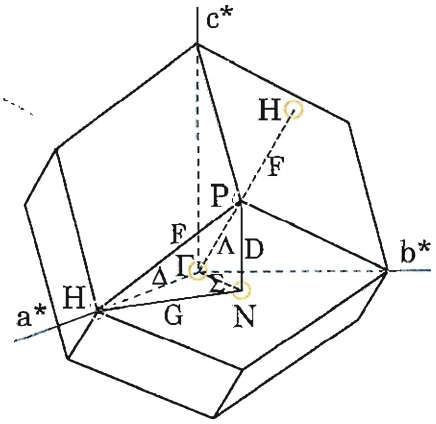

Figure 5.1.1: The first BZ of bcc structure.

5.1 Calculational Procedure of lattice dynamics

Our calculations of phonon dispersion and electron-phonon interaction for β-Po and bcc Se are performed in the framework of the LR-LMTO method which is described in detail in Appendix A.2.

Actual calculational procedures are as follows. We find the dynamical matrix as a function of wave vector for a set of irreducible $\boldsymbol{q}$ points at the (8, 8, 8) reciprocal lattice grid [29 points in the IBZ] for the bcc structure and (6, 6, 6) reciprocal lattice grid [32 points in the IBZ] for the β-Po structure. The (I,J,K) reciprocal lattice grid is defined in a usual manner: $\boldsymbol{q}_{ijk} = (i/I)\boldsymbol{G}_1 + (j/J)\boldsymbol{G}_2 + (k/K)\boldsymbol{G}_3$, where $\boldsymbol{G}_1, \boldsymbol{G}_2, \boldsymbol{G}_3$ are the primitive translations in the reciprocal space. The BZ of the β-Po structure has been shown already in Fig 4.1.1 and that of the bcc structure is depicted in Fig 5.1.1.

The self-consistent calculations are performed for every wave vector with use of the following basis set and criteria. We use 3κ–*spd*–LMTO basis set (27 orbitals) with the one-center expansions performed inside the MT spheres up to $\ell_{max} = 6$. In the interstitial region the basis functions are expanded in plane waves up to the cutoff corresponding to 134 (110), 176 (170), and 320 (320) plane waves per s, p, and d orbitals for bcc (β-Po) structure, respectively. The induced charge densities and the screened potentials are represented inside the MT spheres by spherical harmonics up to $\ell_{max} = 6$ and in the

interstitial region by plane waves with the cutoff corresponding to the (16, 16, 16) fast-Fourier-transform grid in the unit cell of direct space. The $\boldsymbol{k}$-space integration needed for constructing the induced charge density and the dynamical matrix is performed over the (16, 16, 16) grid [145 points in the IBZ] for the bcc structure and (12, 12, 12) grid [185 points in the IBZ] for the β-Po structure, which is twice denser than the grid of the phonon wave vectors $\boldsymbol{q}$. The integration is performed also by the improved tetrahedron method. However, the integration weights for the $\boldsymbol{k}$ points at these grid have been found to take precisely into account the effects arising from the Fermi surface and the energy bands. This is done with help of the band energies generated by the original FPLMTO method at the (32, 32, 32) grid [897 points in the IBZ] for the bcc structure and (24, 24, 24) grid [1313 points in the IBZ] for the β-Po structure. This procedure allows us to obtain more convergent results with respect to the number of $\boldsymbol{k}$ points.

For calculation of the electron-phonon coupling the corresponding $\boldsymbol{k}$-space integrations are more sensitive than dynamical matrices to the number of sampling $\boldsymbol{k}$-points. It has been performed with the help of the (32, 32, 32) grid for bcc and (24, 24, 24) for β-Po in the IBZ by means of the tetrahedron method.

The superconducting transition temperature T_c is calculated by using Allen-Dynes formula which is derived on the basis of the strong coupling theory of phonon mechanism. Instead of describing the details of the strong coupling theory, here we give only the necessary equations to calcuate T_c. In the following we completely obey the description of the refference [32].

For the electron-phonon spectral distribution functions $\alpha^2F(\omega)$, we employ the expression [44] in terms of the phonon linewidths $\gamma_{q\nu}$

$$\alpha^2F(\omega) = \frac{1}{2\pi N(\varepsilon_F)} \sum_{q\nu} \frac{\gamma_{q\nu}}{\omega_{q\nu}} \delta(\omega - \omega_{q\nu}), \tag{5.1.1}$$

where $N(\varepsilon_F)$ is the electronic density of states per atom and per spin at the Fermi level. When the energy bands around the Fermi level are linear in the range of phonon energies, the linewidth is given by the Fermi "golden rule" and is written as follows:

$$\gamma_{q\nu} = 2\pi\omega_{q\nu} \sum_{kjj'} |g^{q\nu}_{k+qj',kj}|^2 \delta(\varepsilon_{kj} - \varepsilon_F)\delta(\varepsilon_{k+qj'} - \varepsilon_F). \tag{5.1.2}$$

where $g^{q\nu}_{k+qj',kj}$ is the electron-phonon matrix element, and conventionally written in the form

$$g^{q\nu}_{k+qj',kj} = \langle \boldsymbol{k}+\boldsymbol{q}j'|\delta^{q\nu}V_{\rm eff}|\boldsymbol{k}j\rangle, \tag{5.1.3}$$

where $\boldsymbol{k}j$ denotes the one-electron basis $\Psi_{\boldsymbol{k}j}$ and $\delta^{q\nu}V_{\rm eff}$ is the change in the effective potential induced from a particular $\boldsymbol{q}\nu$ phonon mode. Precisely speaking, the electron-phonon matrix element must be corrected for the incompleteness of the basis functions, but we do not discuss it here. The expression of $T_{\rm c}$ derived by Allen-Dynes [43] by modifying the McMillan formula [45] is given as

$$T_{\rm c} = \frac{\omega_{\log}}{1.2}\exp\left(-\frac{1.04(1+\lambda)}{\lambda-\mu^*(1+0.62\lambda)}\right), \tag{5.1.4}$$

where

$$\lambda = 2\int_0^\infty {\rm d}\omega \frac{\alpha^2F(\omega)}{\omega}, \tag{5.1.5}$$

$$\omega_{\log} = \exp\frac{1}{\lambda}\int_0^\infty \frac{{\rm d}\omega}{\omega}\alpha^2F(\omega)\log\omega. \tag{5.1.6}$$

Usually λ is called the dimensionless electron-phonon coupling constant, $\omega_{\log}$ the logarithmic -averaged phonon frequency and μ^* the effective screened Coulomb repulsion constant whose value is usually taken to be between 0.1 and 0.15.

In case of monatomic metals λ can be expressed also in the following form:

$$\lambda = \frac{N(\varepsilon_{\rm F})\langle I^2\rangle}{M\langle\omega^2\rangle} = \frac{\eta}{M\langle\omega^2\rangle}, \tag{5.1.7}$$

where M is the mass of the atoms and $\langle\omega^2\rangle$ denotes the average of squared phonon frequencies which is given as

$$\langle\omega^2\rangle = \frac{\displaystyle\int \omega^2\frac{\alpha^2F(\omega)}{\omega}{\rm d}\omega}{\displaystyle\int\frac{\alpha^2F(\omega)}{\omega}{\rm d}\omega}. \tag{5.1.8}$$

Further $\langle I^2\rangle$ represents the Fermi surface average of squared electron-phonon coupling interaction which is defined by

$$\langle I^2\rangle = \frac{\displaystyle\sum_{q\nu}\sum_{kjj'}|g^{q\nu}_{k+qj',kj}|^2\delta(\varepsilon_{kj}-\varepsilon_F)\delta(\varepsilon_{k+qj'}-\varepsilon_F)}{\displaystyle\sum_{q\nu}\sum_{kjj'}\delta(\varepsilon_{kj}-\varepsilon_F)\delta(\varepsilon_{k+qj'}-\varepsilon_F)} \tag{5.1.9}$$

and $\eta = N(\varepsilon_{\rm F})\langle I^2\rangle$ is called the Hopfield parameter.

5.2 Lattice dynamics and superconductivity in bcc Se

5.2.1 Phonon dispersion and phonon anomaly

We first calculated the phonon dispersion curve along the high symmetry line (ΓN) for bcc Se at different 4 volumes (pressures), 10.37 Å^3 (214.2 GPa), 11.11 Å^3 (165.6 GPa), 11.85 Å^3 (128.6 GPa) and 12.59 Å^3 (102.59 GPa). The results are shown in Fig. 5.2.1. As the pressure decreases, the overall tendency of decrease of phonon frequency is seen. In particular, the frequency softening is remarkable for one of the transverse modes (shown by the red curve), and this mode exhibits a notable phonon anomaly, *i.e.*, a dip in the middle of the line. The same phonon anomaly is obtained also in S [20]. This softening of the transverse mode does not cause directly the bcc → β-Po transition with decreasing pressure because both of the β-Po and bcc phases have one atom per unit cell. However Zakharov and Cohen [20] have pointed out that it plays an important role in changing

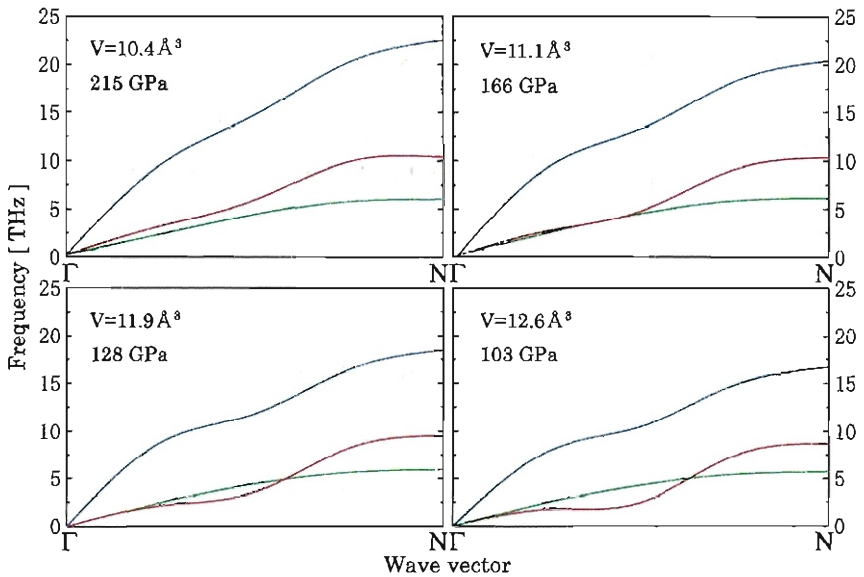

Figure 5.2.1: The phonon dispersion for bcc Se. The blue line denotes longitudinal mode, and the red and green lines the transverse modes.

the coordination number from eight to six during the bcc $\rightarrow$ β-Po transition.

F. Mauri *et al.* have performed *ab initio* linear-response calculation for lattice dynamics of bcc Te under pressures [24]. They reported the same anomaly for the transverse mode along the ΓN line and found that with decreasing pressure the phonon frequencies in the middle of the ΓN line become imaginary in a pressure region where the β-Po structure is stable. In our calculation complete softening of the transverse mode has not been observed even at 100 GPa where the β-Po structure is stable. Complete softening may be realized at further lower pressures.

Figure 5.2.2 shows the pressure dependence of the phonon dispersion along several symmetry lines and the phonon density of state (DOS) calculated at three volumes (or pressures) 11.85 Å^3 (128.6 GPa), 11.41 Å^3 (149.6 GPa) and 11.11 Å^3 (165.6 GPa). It is noted that except along the ΓN line all the phonon frequencies soften linearly with decreasing pressure (or increasing volume).

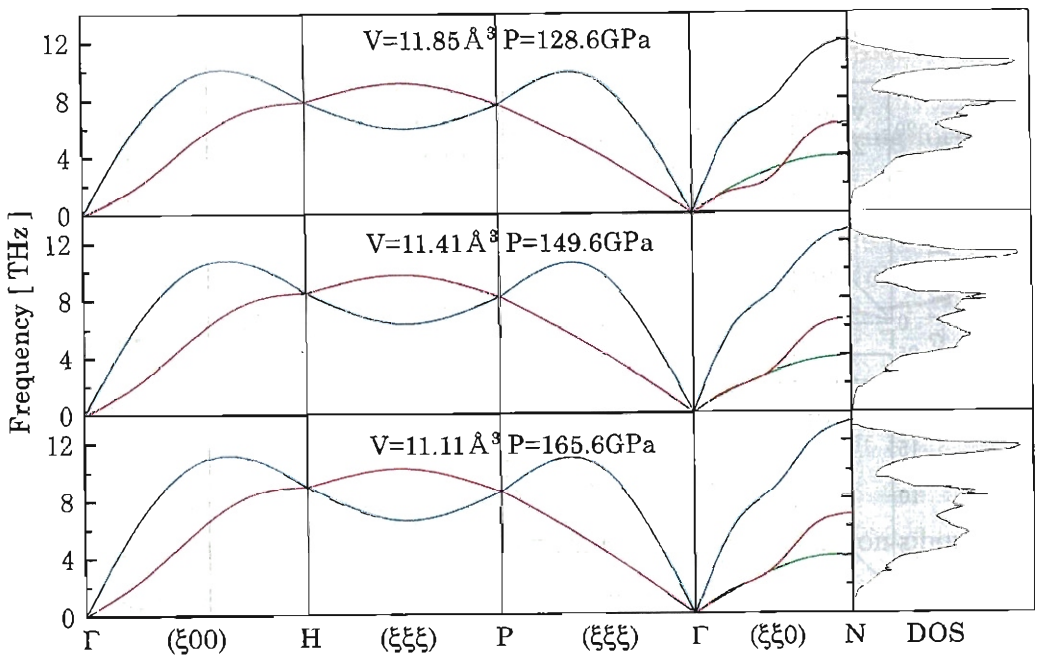

Figure 5.2.2: The phonon dispersion and phonon density of state (DOS) for bcc Se. The blue line denotes longitudinal modes. The red and green lines denote transverse modes.

5.2.2 Pressure dependence of superconducting transition temperature

By using the Allen-Dynes formula we have estimated the superconducting transition temperature T_c of bcc Se at three pressures: 128 GPa, 150 GPa and 166 GPa. In Table 5.1 we give the values of calculated T_c together with DOS at the Fermi level $N(\varepsilon_F)$, the Hopfield parameter η, the logarithmic average frequency ω_{log}, the average of squared phonon frequencies $\langle\omega^2\rangle$ and the electron phonon coupling constant λ. With decreasing pressure the value of ω_{log} decreases while the value of λ increases, but the rate of change of λ exceeds that of ω_{log}. As the results the value of T_c increases considerably with decreasing pressure. Since λ can be expressed by

$$\lambda = \frac{N(\varepsilon_F)\langle I^2\rangle}{M\langle\omega^2\rangle} = \frac{\eta}{M\langle\omega^2\rangle},$$

the frequency softening (decrease of $\langle\omega^2\rangle$) is considered to contribute to the increase of λ with decreasing pressure.

In order to obtain a more physical insight into the characteristic pressure dependence of T_c we first look into mode and wave-vector dependencies of the phonon linewidths $\gamma_{q\nu}$ which are shown in Fig. 5.2.3 along the symmetry lines. From the figure it is clearly recognized that $\gamma_{q\nu}$ is almost independent of pressure except for the longitudinal mode

Table 5.1: The electronic DOS at the Fermi level $N(\varepsilon_F)$, the Hopfield parameter η, the logarithmic average frequencies ω_{log}, the average of squared phonon frequencies $\langle\omega^2\rangle$, the electron phonon coupling constant λ and the superconducting transition temperatures T_c calculated as a function of pressure for bcc Se. The two values for T_c correspond to two different values of μ^* (0.10 and 0.12). The units of $N(\varepsilon_F)$ and η are state/Ryd./atom/spin and Ryd./a^2, respectively.

P (GPa)	$N(\varepsilon_F)$	η	ω_{log} (K)	$\langle\omega^2\rangle$ (K^2)	λ	T_c (K)
128.6	5.45	0.20	224.73	291.95^2	0.83	11.29, 9.90
149.6	5.24	0.21	248.03	316.41^2	0.73	9.53, 8.11
165.6	5.10	0.21	264.62	335.11^2	0.66	8.03, 6.64

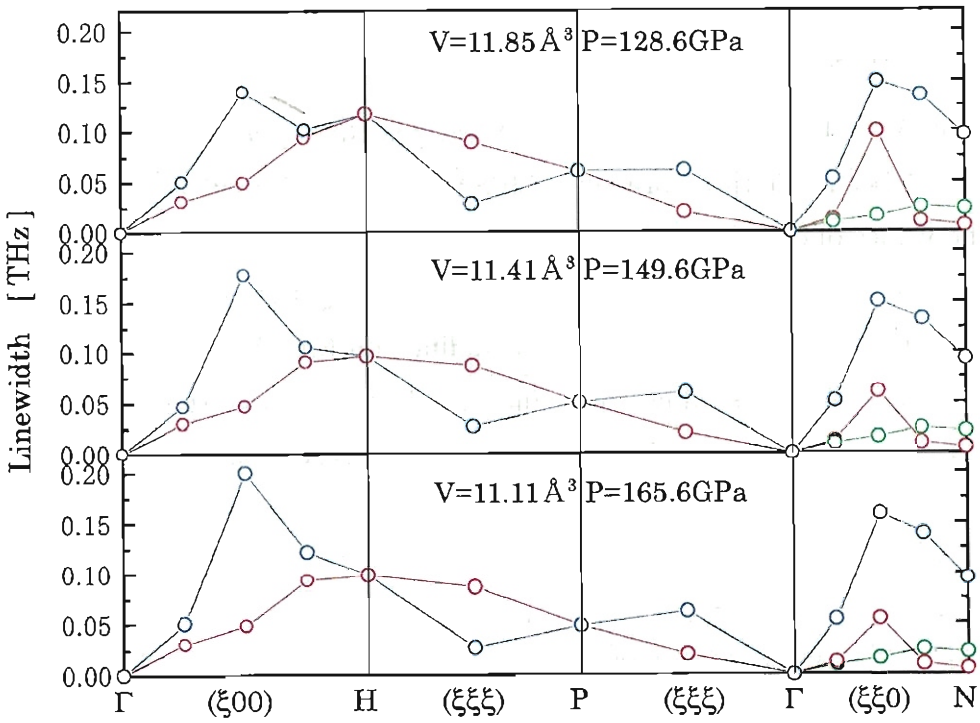

Figure 5.2.3: The phonon line width $\gamma_{q\nu}$ calculated for three different pressures. The blue line denotes the results for the longitudinal mode, and the red and green ones those for the transverse modes. Note that the transverse modes are degenerate along the Γ-H-P-Γ line.

along the ΓH line and one of the transverse modes along the ΓN line represented by red curve.

With decreasing pressure, $\gamma_{q\nu}$ of the longitudinal mode along the ΓH decreases whereas that of the transverse mode along the ΓN line increases considerably. Generally speaking, large phonon linewidth contributes to increase the dimensionless electron-phonon coupling λ. Therefore, it is expected that the transverse mode along the ΓN line plays an important role in giving rise to such a characteristic pressure dependence of T_c.

To clarify the role of the transverse mode along the ΓN line in more detail we have calculated a quantity $\alpha^2(\omega)$ which is defined by

$$\alpha^2(\omega) = \frac{\alpha^2 F(\omega)}{D(\omega)}, \tag{5.2.1}$$

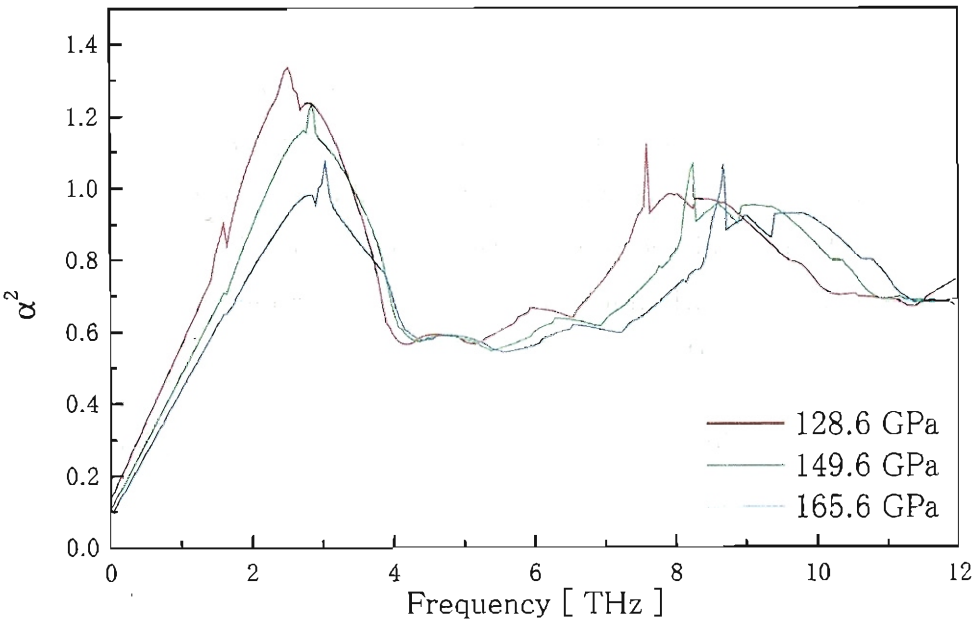

Figure 5.2.4: The frequency dependence of $\alpha(\omega)^2$ obtained for three pressures.

where $\alpha^2F(\omega)$ is the spectral function and $D(\omega)$ denotes the phonon density of states. We consider that by inspecting the frequency dependence of $\alpha^2(\omega)$ we can know which phonons make dominant contribution to the dimensionless electron-phonon coupling λ. In Fig 5.2.4 the calculated $\alpha^2(\omega)$ is shown as a function of frequency for three pressures. It may be reasonably regarded that the peak around 2 THz originates from transverse phonons along the ΓN line and the peak around 7∼10 THz from longitudinal phonons along the ΓH line. As seen from the figure, both the peaks move towards the lower frequency side with decreasing pressure owing to the frequency softening. It should be noted, however, that the magnitude of $\alpha^2(\omega)$ around 2 THz increases remarkably with decreasing pressure whereas the magnitude of $\alpha^2(\omega)$ around 7∼10 THz is less dependent on pressure. Therefore, we can say again that transverse phonons in the middle of the ΓN line make a dominant contribution to λ.

Combining all of the above results we conclude that the origin of remarkable increase of T_c of bcc Se with decreasing pressure is mainly attributed to phonon anomaly (remarkable frequency softening) in the middle of the ΓN line.

5.3 Superconductivity in β-Po

In this section we calculate the superconducting transition temperature of β-Po Se. To see the pressure dependence of T_c in β-Po Se we have calculated T_c at pressures 103.1 GPa and 118.2 GPa with use of two kinds of lattice constants: one is the lattice constants evaluated by calculation and the other is those determined by experiments which are given in Table 5.2. Figure 5.3.1 shows the electronic dispersion curves and the density of states calculated for 103.1 GPa.

Table 5.2: Two sets of lattice constants c/a and a of β-Po Se determined by calculation and experiments.

	103.1 GPa calc.	103.1 GPa Exp.	118.2 GPa calc.	118.2 GPa Exp.
c/a	0.71	0.75	0.67	0.74
a (Å)	7.471	7.314	7.504	7.255

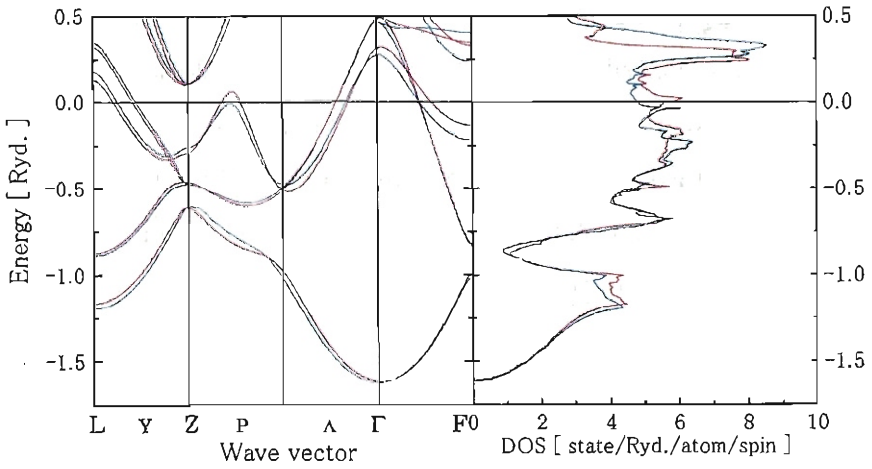

Figure 5.3.1: The band structure and the DOS of β-Po Se at atomic volume V=12.59 Å (103.1 GPa). The red curves denote the results obtained with use of lattice constants estimated by calculation and the blue ones those with use of lattice constants determined by experiments. [19]. The horizontal line denotes the Fermi level.

The values of calculated T_c are given in Table 5.3 together with the electronic DOS at the Fermi level $N(\varepsilon_F)$, the Hopfield parameter η, the logarithmic average frequency ω_{log}, the average of squared phonon frequencies $\langle\omega^2\rangle$ and the electron phonon coupling constants λ. Comparing T_c obtained for different sets of lattice constants there is a large difference. For the lattice constants estimated by calculation the magnitude of T_c is larger and it increases considerably with decreasing pressure. For lattice constants determined by measurements, on the other hand, the magnitude of T_c is smaller and it depends little on pressure.

As to the logarithmic average frequencies ω_{log} we obtain larger values for the experimental lattice constants. As to the electron-phonon coupling λ, on the other hand, for the theoretical lattice constants we have much larger values and furthermore λ depends considerably on pressure, which gives higher and pressure-sensitive transition temperature T_c in case of the theoretical lattice constants.

In order to clarify the origin of the different magnitude and the different pressure dependence of T_c for different sets of lattice constants we have calculated the phonon

Table 5.3: The electronic DOS at the Fermi level $N(\varepsilon_F)$, the Hopfield parameter η, the logarithmic average frequencies ω_{log}, the average of squared phonon frequencies $\langle\omega^2\rangle$, the electron phonon coupling constant λ and the superconducting transition temperatures T_c of β-Po Se calculated for 103.1 GPa and 118.2 GPa. The upper two lines show the results obtained with use of the lattice constants estimated by calculation and the lower two lines those with use of the lattice constants determined by experiments. The two values for T_c correspond to two different values of μ^* (0.10 and 0.12). The units of $N(\varepsilon_F)$ and η are state/Ryd./atom/spin and Ryd./a^2, respectively.

P (GPa)	$N(\varepsilon_F)$	η	ω_{log} (K)	$\langle\omega^2\rangle$ (K^2)	λ	T_c (K)
103.1	5.23	0.19	192.98	264.72^2	0.92	11.74, 10.49
118.2	5.50	0.19	204.84	279.76^2	0.82	10.10, 8.84
103.1	4.89	0.16	250.11	311.71^2	0.58	5.14, 4.04
118.2	4.85	0.17	255.88	324.58^2	0.57	5.01, 3.91

density of states $D(\omega)$, the spectral function $\alpha^2F(\omega)$ and $\alpha^2(\omega)$ defined by Eq. 5.2.1. The results are shown in Fig. 5.3.2. All of the three quantities behave differently for different sets of lattice constants. The magnitude of $\alpha^2(\omega)$ for the theoretical lattice constants is larger than that for the experimental lattice constants almost on the whole frequency

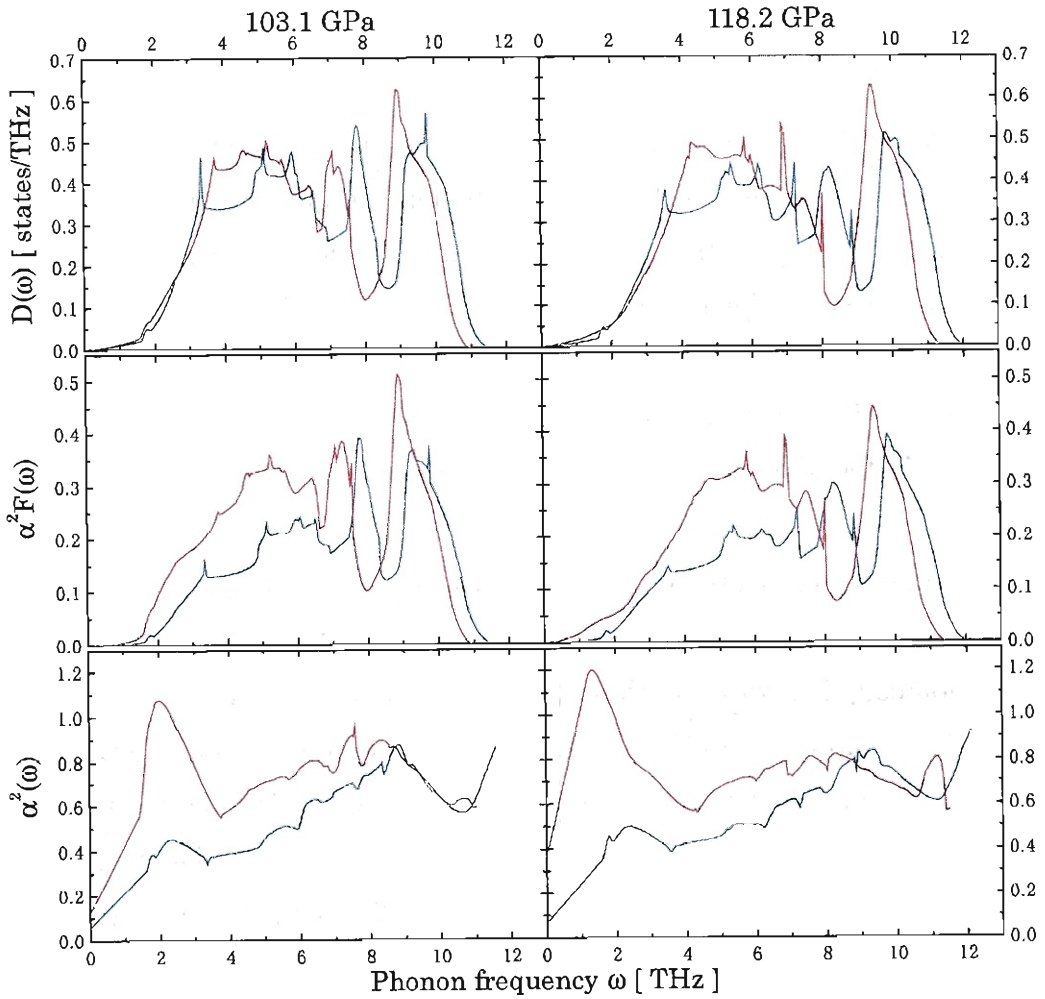

Figure 5.3.2: The phonon density of states $D(\omega)$, the spectral function $\alpha^2F(\omega)$ and $\alpha^2(\omega)$ defined by Eq. 5.2.1 calculated for pressures 103.1 GPa (left hand side) and 118.2 GPa (right hand side) with use of the theoretical and experimental lattice constants. The red curves represent the results for the theoretical lattice constants and the blue curves for the experimental lattice constants.

range. In particular the magnitude of a peak in $\alpha^2(\omega)$ around 2 THz obtained for the calculational lattice constants is remarkably enhanced compared with that obtained for the experimental ones, thus the magnitude of λ and T_c take large values. For the experimental lattice constants $\alpha^2(\omega)$ depends little on pressure and hence the magnitude of λ and T_c are also less dependent on pressure. In any we recognize that electron-phonon coupling λ and the superconducting transition temperature T_c depend sensitively on the values of lattice constants.

In summary we show in Fig. 5.3.3 the values of T_c calculated for β-Po and bcc Se as a function of pressure. In conclusion, if we adopt the experimental lattice constants for β-Po Se, the superconducting transition temperature T_c is almost pressure independent in β-Po phase and there is a large jump in T_c at the transition from β-Po to bcc.

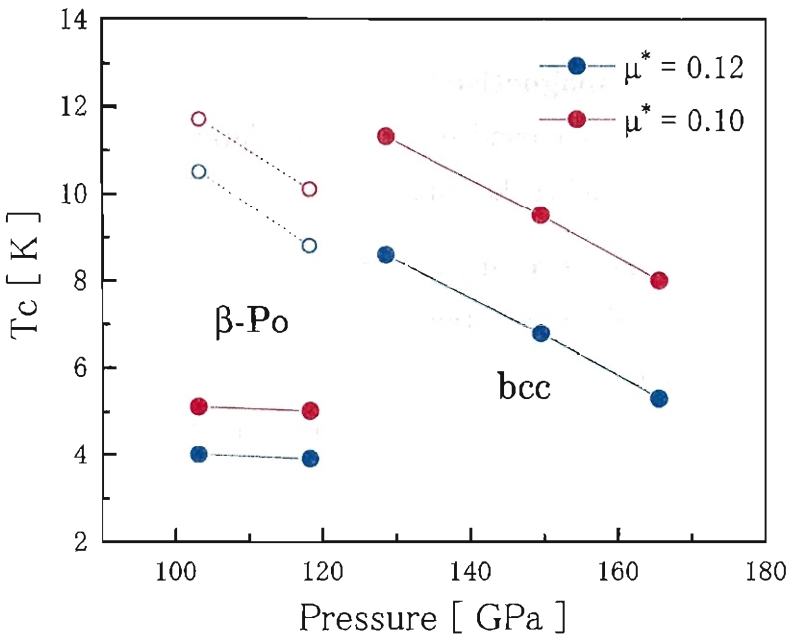

Figure 5.3.3: The superconducting transition temperature T_c of Se as a function of pressure. The blue and red circles denote the computed values of T_c with μ^*=0.12 and μ^*=0.10, respectively. For the β-Po structure the open circles represent the results for the lattice constants estimated by calculation and the closed circles those for the lattice constants determined by experiments.

Chapter 6

Summary

In this thesis we have made first-principles study on solid oxygen and selenium under high pressures. Here we summarize the main results obtained by the present study.

Electronic structure and magnetism of molecular phase of oxygen

We have performed electronic band structure calculations using FPLMTO for molecular phases of oxygen by changing the volume.

- **Electronic band structure at ambient pressure**
  We have found that the most stable state is the AF state at ambient pressure. The spin polarization is due to the split between HOMO and LUMO by exchange interaction. We have also found that character of a free oxygen molecule is still kept in α-O_2.

- **Insulator-metal transition**
  Our present work show that the pressure-induced insulator-metal transition occurs by band overlapping which closes the indirect energy gap. At the transition volume V_M=25.98 Å^3, the magnetic moment still remains in each molecule. With farther decreasing the volume the magnetic moment disappear and the nonmagnetic metallic phase is realized at V_M=11.36 Å^3 which corresponds to the ζ-phase at 116 GPa.

Our present calculational results indicate strongly that solid oxygen would be a nonmagnetic metal under high pressures higher than about 100 GPa.

Monatomic phase of selenium and oxygen

In order to find out pressure-induced phase transition in monatomic selenium and oxygen we have performed FPLMTO calculation for the β-Po and the bcc structures.

- **Pressure induced phase transition in monatomic selenium**

  We have succeeded in reproducing the phase transition from β-Po to bcc as observed from experiment. The obtained pressure dependencies of lattice parameters agree fairly well with the experimental results. The estimated transition pressure is 120 GPa. It improves the previous theoretical calculations, but still lower than the experimental value 150 GPa.

- **Investigation of monatomic oxygen**

  We have calculated the total energy of monatomic oxygen by adopting the β-Po structure which includes the bcc, fcc and sc structures. We have found that the results for oxygen are quite different from those for selenium. As the results we suppose that oxygen may give rise to a structural sequence of monatomic phase different from other VI-b elements.

Lattice dynamics and superconductivity of monatomic selenium

We have investigated the lattice dynamics and electron-phonon interaction of β-Po and bcc structure Se by using linear-response FPLMTO method. The superconducting transition temperature T_c is calculated in the frame work of Allen-Dynes formalism.

- **Phonon dispersion and phonon anomaly in bcc structure**

  We observed overall tendency of decrease of phonon frequency with decreasing pressure. In particular, the frequency softening is remarkable for one of the transverse modes in the middle of the ΓN-line, and this mode exhibits a notable phonon anomaly. In our calculation for Se complete softening of this phonon mode has not been observed, in contrast with the same phonon mode in Te [24].

- **Pressure dependence of T_c in bcc structure**

  The pressure dependence of T_c has benn estimated. With decreasing pressure the

value of T_c increases considerably. The origin of remarkable increase of T_c is mainly attributed to phonon anomaly in the middle of the ΓN line.

- **Superconductivity in β-Po structure**
  We have calculated T_c of β-Po Se for two kinds of lattice constant: the lattice constants evaluated by calculation and those determined by experiments. The obtained T_c is quite different between the theoretical and the experimental lattice constants. For the former T_c is larger and it increases considerably with decreasing pressure. For the latter, on the other hand, T_c is smaller and it depend little on pressure. The origin of this discrepancy is due to the magnitude of density of state at the Fermi energy and the enhancement of $\alpha^2(\omega)$ at low frequencies of theoretical lattice constants.

Finally we predict the pressure dependence of realistic monatomic Se as follows: in β-Po phase T_c is almost pressure independent and there is a large jump in T_c at the transition from β-Po to bcc, and then in bcc phase T_c decreases rapidly with increasing pressure.

Appendix A

1D Chain of Oxygen molecules

As mentioned in Introduction magnetic properties of the 1D system of oxygen molecules physisorbed in Cu-trans-1,4-cyclohexanedicarboxylic acid (CCHD) are unusual and quite interesting. In order to seek for the origin of such peculiar magnetic properties we investigate in this Appendix A the magnetism of 1D chain of oxygen molecules on the basis of a model Hamiltonian. Since the degenerate antibonding π^* orbitals, $\pi^*_{2p_x}$ and $\pi^*_{2p_y}$, of a single oxygen molecule play an important and essential role for the magnetic properties, a relevant model Hamiltonian will be a two-band Hubbard Hamiltonian. Therefore we first construct a model Hamiltonian appropriate to 1D chain of oxygen molecules, and then analyze it in detail. We pay particular attention to how the magnetic properties are affected by change of inter-molecular transfer energies which may be controlled by pressure. We also focus our attention on the effect of removing degeneracy of $\pi^*_{2p_x}$ and $\pi^*_{2p_y}$ orbitals.

A.1 Construction of model Hamiltonian

We adopt the following form of 1-D two-band Hubbard Hamiltonian:

$$\begin{aligned}\mathcal{H} &= \sum_{i\mu\sigma} V_\mu n_{i\mu\sigma} + \sum_{\sigma}\sum_{i\mu\nu} T_{i\mu,i+\delta\nu} C^\dagger_{i\mu\sigma} C_{i+\delta\nu\sigma} \\ &+ \sum_{i\mu} U n_{i\mu\uparrow} n_{i\mu\downarrow} + \sum_{\sigma_1\sigma_2}\sum_{i\mu\neq\nu} U n_{i\mu\sigma_1} n_{i\nu\sigma_2}\end{aligned}$$

$$+ \sum_{\sigma_1\sigma_2} \sum_{i\mu\neq\nu} J C^{\dagger}_{i\mu\sigma_1} C^{\dagger}_{i\nu\sigma_2} C_{i\mu\sigma_2} C_{i\nu\sigma_1} \tag{A.1.1}$$

where $c^{\dagger}_{i\mu\sigma}(c_{i\mu\sigma})$ represents creation (annihilation) operator of μ-orbital with σ-spin at i th O_2 molecule and $n_{i\mu\sigma}$ is the number operator. Here we are considering two orbitals μ=1 or 2, keeping in mind two molecular orbitals $\pi^*_{2p_x}$ and $\pi^*_{2p_y}$ as shown in Fig. A.0.1. The first term denotes the orbital energies and the second term the inter-molecular transfer energies. The third, the fourth and the fifth terms represent, respectively, the intra-orbital Coulomb energy, the inter-orbital Coulomb energy and the exchange interaction. For simplicity we assume that the intra- and the inter-orbital Coulomb energies are the same. Further we consider transfer energies only between nearest neighboring (n.n.) molecules, that is, $\delta = \pm 1$ in the second term.

In order to estimate the intra-molecular exchange interaction J we applied *ab initio* Molecular Orbital (CASSCF/6-31Gd) calculations for single O_2 molecule and obtained J=0.95 eV. As for the Coulomb energy U we adopt the value estimated by Bhandari *et al* [46]: U=11.6 eV. These values of J and U are expected to be less dependent on the inter-molecular distance. The orbital energy V_μ and the transfer energy $T_{i\mu,i+\delta\nu}$ are expected to depend strongly on materials, and hence we investigate the ground state properties of Hamiltonian A.1.1 for a wide range of V_μ and $T_{i\mu,i+\delta\nu}$.

Before proceeding to actual calculations, however, we have made rough estimation of V_μ and $T_{i\mu,i+\delta\nu}$ for the orthorhombic δ-phase of solid oxygen. The orbital energy difference and transfer energy configuration is defined as Fig A.1.2. First, we have carried out FPLMTO band calculations for the paramagnetic state of the δ-phase with the lattice

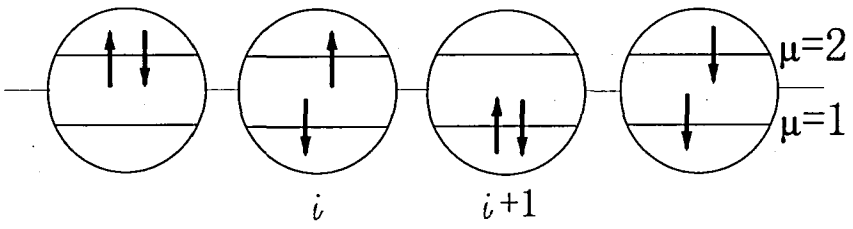

Figure A.0.1: A schematic view of molecular arrangement in our two-band Hubbard model.

constant observed at 9.6 GPa, a=4.22 Å, b=2.95 Å and c=6.69 Å. Then, by a fitting procedure with use of tight-binding (TB) method we have estimated V_μ and $T_{i\mu,i+\delta\nu}$. Figure A.1.1 shows the comparison of the energy dispersions and the density of states (DOS) calculated by the FPLMTO and TB method. As seenfrom the figure the DOS we can consider the main component of the wave function near the E_F is $\pi^*_{2p_x}$ and $\pi^*_{2p_y}$ orbitals. It is seen that band structures near E_F are reproduced fairly well by the TB method. The estimated values of nearest neighboring (n.n.) transfer energies and the orbital energy difference are given in Table A.1. The transfer energies between farther neighboring molecules are smaller by one order of magnitude or more compared with those between n.n. molecules. In this sense, the δ-phase may be regarded as a pseudo-two-dimensional (2-D) system.

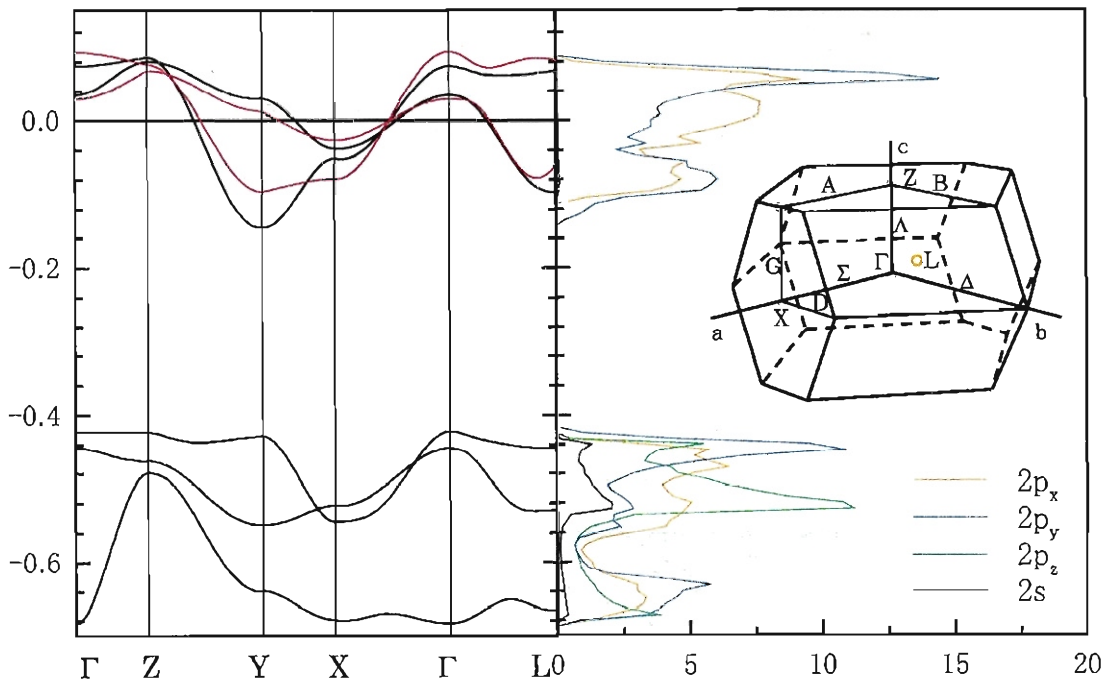

Figure A.1.1: The energy dispersion and the DOS of the δ-phase calculated by the FPLMTO method (black0 curve) and by the TB method (red curves).

Table A.1: The estimated values of the n.n. intermolecular transfer energies and the orbital energy difference in the TB calculation which can reproduce the band structures obtained by the FPLMTO method (in unit of eV).

T_{xx}	T_{xy}	T_{yy}	$V_y - V_x$
0.29	0.28	0.096	0.49

A.2 Analysis by exact diagonalization

In order to clarify the nature of the ground state we have adopted the exact diagonalization method with use of Lanczos transformation, and calculated the following physical quantities, electron number of each orbital n_μ, fluctuation of electron number $(\delta n_\mu)^2$, local spin moment at each molecule $\boldsymbol{S}_i^2$, and spin–spin correlation function $< \boldsymbol{S}_{i\mu} \cdot \boldsymbol{S}_{i+\delta\nu} >$, which are defined as

$$n_\mu = \frac{1}{2N} < \sum_i \sum_\sigma n_{i\mu\sigma} >, \tag{A.2.1}$$

$$(\delta n_\mu)^2 = \frac{1}{2N} < \sum_i (\sum_\sigma n_{i\mu\sigma} - \sum_\sigma < n_{i\mu\sigma} >)^2 >, \tag{A.2.2}$$

$$\boldsymbol{S}_i^2 = \frac{1}{N} < \sum_{i\mu\nu} \{ S_{i\mu}^z S_{i\nu}^z + \frac{1}{2}(S_{i\mu}^+ S_{i\nu}^- + S_{i\mu}^- S_{i\nu}^+) \} >, \tag{A.2.3}$$

$$< \boldsymbol{S}_{i\mu} \cdot \boldsymbol{S}_{i+\delta\nu} > = \frac{1}{2N} \sum_i \{ < \boldsymbol{S}_{i\mu} \cdot \boldsymbol{S}_{i+\delta\nu} + \boldsymbol{S}_{i\nu} \cdot \boldsymbol{S}_{i+\delta\nu} > \}. \tag{A.2.4}$$

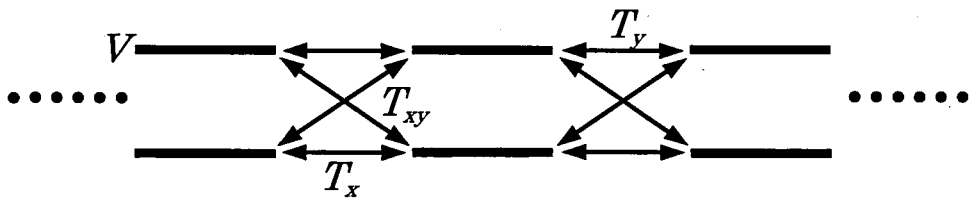

Figure A.1.2: Illustration of the n.n. intermolecular transfer energies (T_x, T_{xy}, T_y) and the orbital energy difference in the model Hamiltonian.

In performing actual calculations we renormalized the energies by the exchange energy J, and throughout this paper we fixed the Coulomb repulsion energy to U/J=10. Further the electron number per molecule is fixed to two, that is, half-filling is assumed. We define $v \equiv (V_2 - V_1)/J$ (> 0), and by assuming T_{11}=T_{12} and T_{22}=0 for simplicity we also define $\tau \equiv T_{11}/J$. Finally exact diagonalizations have been performed for the chain size N=6 with use of the periodic boundary condition.

Figure A.2.1(a), (b) and (c) shows the contour maps of the calculated n_μ, $(\delta n_\mu)^2$ and $\boldsymbol{S}_i^2$, respectively, in the $v - \tau$ plane. We here note that qualitatively the same results as shown in Fig. A.2.1 have been obtained from calculations by assuming T_{11}=T_{22}=0, $T_{12} \neq 0$ or T_{11}=T_{12}=T_{22}. It should be also noted that AF behavior of spin correlation has been recognized, although spin correlation itself diminishes with increasing τ.
For small τ, as seen from Fig. A.2.1(b), fluctuation of electron number $(\delta n_\mu)^2$ at each site is quite small, which indicates that electrons are localized, *i.e.* the system is an insulator (AF insulator). For large τ, on the other hand, $(\delta n_\mu)^2$ have significant values, which indicates itinerant character of electrons. Our calculations are for finite size systems, and therefore it is rather difficult to give rigorous discussion on insulator-metal transition. However, from the present results we may expect transition from AF-insulator to AF-metal with increasing the transfer energy. Since solid oxygen is rather a 2-D system, we are extending our calculations to 2-D two-band Hubbard Hamiltonian in order to get insight into the magnetic properties of solid oxygen under high pressures.

Now we pay attention to the effects of v (orbital energy difference) on the magnetic properties, confining ourselves in the small τ region. Then, as recognized clearly from Figs. A.2.1(a), (b) and (c) oxygen molecule has certainly well-defined spin S=1 in case of small v, whereas with increasing v local spin moment of oxygen molecule diminishes toward spin singlet state. On the basis of this result we suggest that peculiar magnetic properties of oxygen physisorbed in CCHD may be explained by taking account of the effect of orbital energy difference. We reasonably expect that the orbital energy difference may be large in oxygen in restricted geometry.

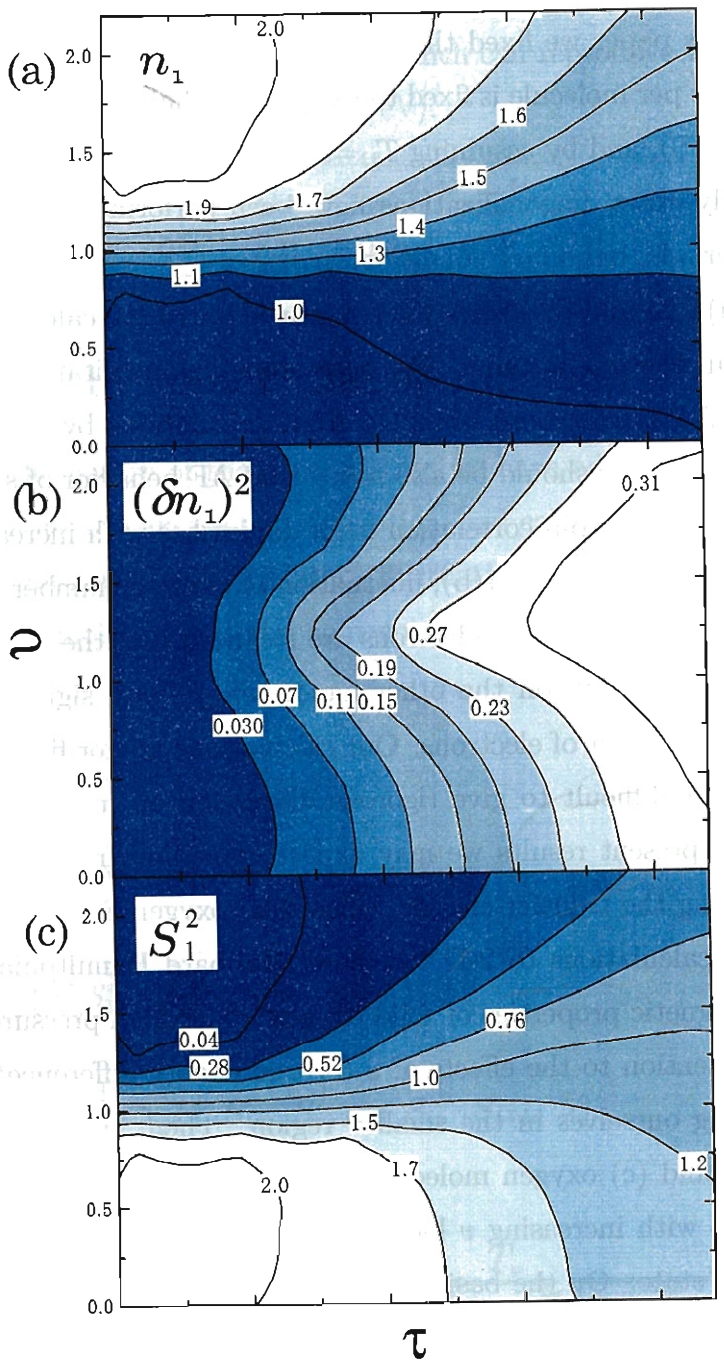

Figure A.2.1: The contour map of (a) n_1 (electron number in lower orbital), (b) (δn_1) (fluctuation of n_1) and (c) S_i^2 (local spin moment) in the $\upsilon - \tau$ plane, which are obtained for the chain size N=6 with use of U/J=10.

Appendix B

Theoretical Methods

B.1 Full Potential LMTO

In this section we give some computational techniques which are necessary for actual calculations using the FPLMTO method.

B.1.1 Fourier transform of pseudo-LMTO's

In this method, lattice Fourier transformation is performed to get the numerical values of the Hankel functions in the interstitial region[31]. To improve the convergence with respect to the number of reciprocal lattice vectors, we define "pseudo"-LMTO. Namely, the Bloch orbitals are split into a smooth pseudo-LMTO part $\tilde{K}_{\kappa L}$ which extends over the entire space, and a local and strongly varying part which is nonzero only inside the MTS and approaches zero continuously and differentiably on the boundaries. Thus $\tilde{K}_{\kappa L}$ is the solution of the equation

$$(-\nabla^2 - \kappa^2)\tilde{K}_{\kappa L}(\boldsymbol{r}) = g_L(\boldsymbol{r}). \tag{B.1.1}$$

The function on the right-hand side of the Helmholz equation is a decaying Gaussian toward MTS boundaries with multiplied spherical harmonics:

$$g_L(\boldsymbol{r}) = g_L^0 \left(\frac{\eta}{\pi}\right)^{\frac{3}{2}} r^\ell \mathrm{e}^{-\eta r^2} \mathrm{i}^\ell Y_L(\hat{\boldsymbol{r}}),$$

where g_L^0 is a normalization constant which defines later. The most important parameter is η. It is chosen such that the Gaussian is approximately zero when $r > S_{MT}$ and η must depend on ℓ as well as the sphere radius S_{MT}. The solution $\tilde{K}_{\kappa L}$ is thus the Hankel function for large r, it is a regular function for small r and it is smooth together with its radial derivatives at any r.

The Bloch sums and Fourier transform of pseudo-LMTO and $g_L(\boldsymbol{r})$ is given as:

$$\tilde{\chi}^{\boldsymbol{k}}_{\kappa RL}(\boldsymbol{r}) = \sum_{\boldsymbol{t}} \mathrm{e}^{\mathrm{i}\boldsymbol{k}\cdot\boldsymbol{r}} \tilde{K}_{\kappa L}(\boldsymbol{r}_R - \boldsymbol{t}) = \sum_{\boldsymbol{G}} \tilde{\chi}_{\kappa RL}(\boldsymbol{k}+\boldsymbol{G}) \mathrm{e}^{\mathrm{i}(\boldsymbol{k}+\boldsymbol{G})\cdot\boldsymbol{r}} \tag{B.1.2}$$

$$G^{\boldsymbol{k}}_{RL}(\boldsymbol{r}) = \sum_{\boldsymbol{t}} \mathrm{e}^{\mathrm{i}\boldsymbol{k}\cdot\boldsymbol{r}} g_L(\boldsymbol{r}) = \sum_{\boldsymbol{G}} u_{RL}(\boldsymbol{k}+\boldsymbol{G}) \mathrm{e}^{\mathrm{i}(\boldsymbol{k}+\boldsymbol{G})\cdot\boldsymbol{r}}, \tag{B.1.3}$$

where $\boldsymbol{G}$ is the reciprocal lattice vector. And the Helmholtz equation (B.1.1) in the reciprocal space is represented as

$$(-\nabla^2 - \kappa^2) \sum_{\boldsymbol{G}} \tilde{\chi}_{\kappa RL}(\boldsymbol{k}+\boldsymbol{G}) \mathrm{e}^{\mathrm{i}(\boldsymbol{k}+\boldsymbol{G})\cdot\boldsymbol{r}} = \sum_{\boldsymbol{G}} u_{RL}(\boldsymbol{k}+\boldsymbol{G}) \mathrm{e}^{\mathrm{i}(\boldsymbol{k}+\boldsymbol{G})\cdot\boldsymbol{r}}. \tag{B.1.4}$$

The Fourier coefficients $\tilde{\chi}_{\kappa RL}$ is given by solving equation (B.1.4)

$$\tilde{\chi}_{\kappa RL}(\boldsymbol{k}+\boldsymbol{G}) = \frac{u_{RL}(\boldsymbol{k}+\boldsymbol{G})}{|\boldsymbol{k}+\boldsymbol{G}|^2 - \kappa^2}. \tag{B.1.5}$$

For the Fourier coefficients $u_{RL}(\boldsymbol{k}+\boldsymbol{G})$, we obtain the following relation by performing inverse Fourier transformation for equation (B.1.3)

$$u_{RL}(\boldsymbol{k}+\boldsymbol{G}) = \Omega_{\mathrm{cell}}^{-1} \mathrm{e}^{-\mathrm{i}(\boldsymbol{k}+\boldsymbol{G})\cdot\boldsymbol{R}} g_L^0 Y_\ell^m(\widehat{\boldsymbol{k}+\boldsymbol{G}}) (2\eta)^{-\ell} |\boldsymbol{k}+\boldsymbol{G}|^\ell \mathrm{e}^{-|\boldsymbol{k}+\boldsymbol{G}|^2/4\eta}, \tag{B.1.6}$$

where Ω_{cell} is volume of the unit cell. The normalization constant g_L^0 is defined as

$$g_L^0 = 4\pi (2\eta)^\ell \frac{S_{MT}^{\ell+1} \mathrm{e}^{\kappa^2/4\eta}}{(2\ell-1)!!}, \tag{B.1.7}$$

under condition that smooth connection to the real Hankel function at MTS.

Finally, we obtain the Fourier coefficients $\tilde{\chi}_{\kappa RL}$ by substituting (B.1.6) and (B.1.7) for (B.1.5)

$$\begin{aligned} \tilde{\chi}_{\kappa RL}(\boldsymbol{k}+\boldsymbol{G}) = {} & \frac{4\pi}{\Omega_{\mathrm{cell}}} \frac{S_{MT}^{\ell+1}}{(2\ell-1)!!} \frac{|\boldsymbol{k}+\boldsymbol{G}|^\ell}{|\boldsymbol{k}+\boldsymbol{G}|^2 - \kappa^2} \mathrm{e}^{(\kappa^2 - |\boldsymbol{k}+\boldsymbol{G}|^2)/4\eta} \\ & \times Y_\ell^m(\widehat{\boldsymbol{k}+\boldsymbol{G}}) \mathrm{e}^{-\mathrm{i}(\boldsymbol{k}+\boldsymbol{G})\cdot\boldsymbol{R}}, \end{aligned} \tag{B.1.8}$$

where the Gaussian damping parameter is defined by the following relation

$$\frac{(S_{MT}\eta_\ell^2)^{\ell+2}\mathrm{e}^{-(S_{MT}\eta_\ell)^2}}{(G_{cut}/2\eta_\ell^2)^{\ell}\mathrm{e}^{-(G_{cut}/2\eta_\ell^2)^2}} = const. \tag{B.1.9}$$

The right hand side is set as 0.5 in the present work and G_{cut} is the absolute value of maximum reciprocal lattice vector to be used, which is defined by numerical and computational conditions.

B.1.2 Representation of density

The valence density is given by the sum of the squares of the wave functions. Using equation (2.1.8) we obtain the valence density

$$n^v(\boldsymbol{r}) = \sum_{k\lambda}\sum_{\kappa RL}\sum_{\kappa' R' L'} f_{k\lambda} A^{k\lambda *}_{\kappa' R' L'} A^{k\lambda}_{\kappa RL} \chi^{k}_{\kappa' R' L'}(\boldsymbol{r}) \chi^{k}_{\kappa RL}(\boldsymbol{r}), \tag{B.1.10}$$

where $f_{k\lambda}$ is occupation number of each orbitals. We split the valence density (B.1.10) into two part

$$n^v(\boldsymbol{r}) = \sum_{\boldsymbol{t}}\sum_{R} \hat{n}^v_R(\boldsymbol{r}-\boldsymbol{t}) + \tilde{n}(\boldsymbol{r}) \tag{B.1.11}$$

with

$$\hat{n}^v_R(\boldsymbol{r}) = \sum_L \hat{n}^v_{RL}(r)\mathrm{i}^\ell Y_L(\hat{\boldsymbol{r}}), \tag{B.1.12}$$

and

$$\tilde{n}(\boldsymbol{r}) = \sum_{\boldsymbol{G}} \tilde{n}(\boldsymbol{G})\mathrm{e}^{\mathrm{i}\boldsymbol{G}\cdot\boldsymbol{r}}. \tag{B.1.13}$$

The density n^v given in Eq. (B.1.11) thus consists of a localized part $\hat{n}^v_R$ and a pseudo-part $\tilde{n}$. $\hat{n}^v_{RL}$ is nonzero only inside the sphere at site R and goes continuously and differentiably to zero at the MTS boundary, whereas $\tilde{n}$ is smooth and nonzero everywhere.

The Hartree potential is calculated by solving Poisson's equation for the total charge density ρ. In order that the localize part of the charge density gives rise to localized potential auxiliary charges Δ, which are localized inside, the MTS are added and subtracted

to the total charge density[25]

$$\rho(\boldsymbol{r}) = \left[\sum_t \sum_R \{\hat{n}_R^v(\boldsymbol{r}-\boldsymbol{t}) + n_R^{c,N}(\boldsymbol{r}-\boldsymbol{t}) - \Delta_{RL}(\boldsymbol{r}-\boldsymbol{t})\}\right] + \left[\tilde{n}(\boldsymbol{r}) + \sum_t \sum_R \Delta_{RL}(\boldsymbol{r}-\boldsymbol{t})\right] \quad \text{(B.1.14)}$$

$$= \hat{\rho}(\boldsymbol{r}) + \tilde{\rho}(\boldsymbol{r}) \quad \text{(B.1.15)}$$

where $n_R^{c,N}$ is the core electron and the nuclear point charges. The Δ's are introduced in order to compensate the multipole moments of the local charge density $\hat{n}_R^v + n_R^{c,N}$, i.e.

$$\int_{\Omega_R} \frac{\hat{n}_R^v(\boldsymbol{\xi}) + n_R^{c,N}(\boldsymbol{\xi}) - \Delta_{RL}(\boldsymbol{\xi})}{|\boldsymbol{r}-\boldsymbol{\xi}|} \mathrm{d}\boldsymbol{\xi} = 0. \quad \text{(B.1.16)}$$

Thus the auxiliary charge Δ have to satisfy the condition

$$\int_0^{S_{MT}} \left[\hat{n}_R^v(r) + \sqrt{4\pi} n_R^{c,N}(r)\delta_{\ell,0} - \Delta_{RL}(r)\right] r^{\ell+2} \mathrm{d}r = 0. \quad \text{(B.1.17)}$$

If Eq. (B.1.17) is fulfilled, $\hat{\rho}$ does not produce an electrostatic field outside its own sphere. The influence of the charge in a given sphere on the rest of the crystal is completely described by the field produced by the Δ which is added to the pseudo-density. Poisson's equation for $\tilde{\rho}$ is solved by Fourier transformation. The auxiliary density Δ must be localize inside MTS and be smooth enough to ensure a fast convergence of the Fourier series. The Gaussian type auxiliary density is used in the present calculations [47]

$$\Delta_{RL}(\boldsymbol{r}) = d_{RL} r^\ell \mathrm{e}^{-(\eta r)^2} \mathrm{i}^\ell Y_L(\hat{\boldsymbol{r}}), \quad \text{(B.1.18)}$$

where the damping constant η is also defined by Eq.(B.1.9) with the following condition:

$$G_{cut}^{\text{orbit.}} \leq G_{cut}^{\text{dens.}}, \quad \text{(B.1.19)}$$

and the coefficient d_{RL} is defined by the condition Eq. (B.1.17).

B.2 Linear-response calculations

For the calculation of the lattice vibrational property and electron-phonon interactions, we use the linear-response FPLMTO (LR-LMTO) method [31, 32]. In this section we briefly review the lattice dynamics, density-functional perturbation theory and representation of dynamical matrices in the framework of linear-response theory.

B.2.1 Lattice Dynamics

The Hamiltonian for the entire system is given by

$$\mathcal{H} = \mathcal{H}_{e\ell} + \mathcal{H}_L + \mathcal{H}_{e\ell-L}, \tag{B.2.1}$$

where $\mathcal{H}_{e\ell}$, $\mathcal{H}_L$, $\mathcal{H}_{e\ell-L}$ denotes electron–electron, phonon–phonon and electron–phonon part, respectively. Each part of the Hamiltonian is expressed as follows:

$$\begin{aligned}
\mathcal{H}_{e\ell} &= \sum_i \frac{\boldsymbol{P}_i^2}{2m} + \frac{1}{2}\sum_{ii'} \frac{e^2}{|\boldsymbol{r}_i - \boldsymbol{r}_{i'}|} \\
\mathcal{H}_L &= \sum_{\ell\mu} \frac{\boldsymbol{P}_{\ell\mu}^2}{2M_\mu} + \frac{1}{2}\sum_{\ell\mu\ell'\mu'} \frac{Z_\mu Z_{\mu'} e^2}{|\boldsymbol{R}_{\ell\mu} - \boldsymbol{R}_{\ell'\mu'}|} \\
\mathcal{H}_{e\ell-L} &= \sum_i \sum_{\ell\mu} \frac{-Z_\mu e^2}{|\boldsymbol{r}_i - \boldsymbol{R}_{\ell\mu}|},
\end{aligned} \tag{B.2.2}$$

where M is the mass of μth ion in the ℓth unit cell and $R_{\ell\mu}$ denotes its position, m is the mass of ith electron and r_i represents its position, and $\boldsymbol{P}_i$ denotes the momentum of ith atom. Let $\Psi(\{r_i\}, \{R_{\ell\mu}\})$ be the eigen function of the Hamiltonian (B.2.1), so that

$$\mathcal{H}\Psi(\{\boldsymbol{r}_i\}, \{\boldsymbol{R}_{\ell\mu}\}) = E\Psi(\{\boldsymbol{r}_i\}, \{\boldsymbol{R}_{\ell\mu}\}), \tag{B.2.3}$$

where E is the total energy of the entire system. In the crystal, we couldn't solve the eigen state of the system which includes about 10^{23} electron and ion. To solve the Schrödinger equation (B.2.3) we applied two kind of approximations, *i.e.*, adiabatic and harmonic approximations.

The essential idea of the adiabatic approximation is that the ions being about 2×10^3 to 10^5 times heavier, move much more slowly than the electrons. At any given instant, therefore, the electrons "see" the ions fixed in some configuration. In the adiabatic approximation,

we separate electronic and ionic motion. So that we define the wave function of the entire system as follows:

$$\Psi(\{\boldsymbol{r}_i\},\{\boldsymbol{R}_{\ell\mu}\}) = \psi(\{\boldsymbol{r}_i\})\chi(\{\boldsymbol{R}_{\ell\mu}\}), \tag{B.2.4}$$

where $\chi(\{\boldsymbol{R}_{\ell\mu}\})$ represent ionic wave function and $\psi(\{\boldsymbol{r}_i\})$ is a wave function for the entire system of electrons. We imagine the ions to be fixed in some configuration and for this particular $\{R_{\ell\mu}\}$ we can construct the Schrödinger equation for the electrons

$$\left[\mathcal{H}_{e\ell}(\{\hat{r}_i\}) + \mathcal{H}_{e\ell-L}(\{\hat{r}_i\},\{R_{\ell\mu}\}) + \frac{1}{2}\sum_{\ell\mu\ell'\mu'}\frac{Z_\mu Z_{\mu'}e^2}{|\boldsymbol{R}_{\ell\mu}-\boldsymbol{R}_{\ell'\mu'}|}\right]\psi(\{\boldsymbol{r}_i\}) = E^{tot}\psi(\{\boldsymbol{r}_i\}), \tag{B.2.5}$$

here E^{tot} denote energy of electronic systems plus ion–ion interactions, $R_{\ell\mu}$ means static ion position and $\hat{r}_i$ denotes an operator. Substituting (B.2.4) in (B.2.3) and making use of (B.2.5), we can define the Hamiltonian for the ions.

$$\mathcal{H}_L = \sum_{\ell\mu}\frac{P_{\ell\mu}^2}{2M_\mu} + V(\{\boldsymbol{R}_{\ell\mu}\}), \tag{B.2.6}$$

here we rewrite $E^{tot}(\{\boldsymbol{R}_{\ell\mu}\})$ to $V(\{\boldsymbol{R}_{\ell\mu}\})$ which is adiabatic potential.
In general, the adiabatic potential $V(\{\boldsymbol{R}_{\ell\mu}\})$ depends on all the individual coordinates $\boldsymbol{R}_{\ell\mu}$ of the ions. If the displacements of the ions from their equilibrium positions $\boldsymbol{R}^0_{\ell\mu}$ are small, $V(\{\boldsymbol{R}_{\ell\mu}\})$ can be written as a power series in the displacements $\boldsymbol{u}_{\ell\mu} = \boldsymbol{R}_{\ell\mu} - \boldsymbol{R}^0_{\ell\mu}$:

$$\begin{aligned} V(\{\boldsymbol{R}_{\ell\mu}\}) &= V(\{\boldsymbol{R}^0_{\ell\mu}\}) + \sum_{m\nu}\sum_{\alpha} u^\alpha_{m\nu}\frac{\partial}{\partial R^\alpha_{m\mu}}V(\{\boldsymbol{R}_{\ell\mu}\})\Big|_{\{\boldsymbol{R}_{\ell\mu}\}=\{\boldsymbol{R}^0_{\ell\mu}\}} \\ &\quad + \frac{1}{2}\sum_{m\nu}\sum_{n\lambda}\sum_{\alpha\beta} u^\alpha_{m\nu}u^\beta_{n\lambda}\frac{\partial^2}{\partial R^\alpha_{m\nu}\partial R^\beta_{n\lambda}}V(\{\boldsymbol{R}_{\ell\mu}\})\Big|_{\{\boldsymbol{R}_{\ell\mu}\}=\{\boldsymbol{R}^0_{\ell\mu}\}} + \cdots, \end{aligned} \tag{B.2.7}$$

where α,β is the Cartesian component. In harmonic approximation, the series is terminated at second derivatives. Further corrections to $V(\{\boldsymbol{R}_{\ell\mu}\})$, especially those of third and forth term, are known as unharmonic terms. Since $V(\{\boldsymbol{R}^0_{\ell\mu}\})$ is just the static potential energy of the crystal (*i.e.*, independent of the displacement coordinates), it can be

ignored for the time being. The expansion coefficients are defined as follows:

$$V^{\alpha}_{m\nu} = \frac{\partial}{\partial R^{\alpha}_{m\nu}} V(\{\boldsymbol{R}_{\ell\mu}\})\Big|_{\{\boldsymbol{R}_{\ell\mu}\}=\{\boldsymbol{R}^0_{\ell\mu}\}} \tag{B.2.8}$$

$$V^{\alpha\beta}_{m\nu\lambda} = \frac{\partial^2}{\partial R^{\alpha}_{m\nu}\partial R^{\beta}_{n\lambda}} V(\{\boldsymbol{R}_{\ell\mu}\})\Big|_{\{\boldsymbol{R}_{\ell\mu}\}=\{\boldsymbol{R}^0_{\ell\mu}\}} . \tag{B.2.9}$$

The force acting on the $\ell\mu$ atom in the α–direction due to the displacements of all atoms $m\nu$ is given by

$$F^{\alpha}_{\ell\mu} = -V^{\alpha}_{\ell\mu} - \sum_{m\nu}\sum_{\beta} V^{\alpha\beta}_{\ell\mu m\nu} u^{\beta}_{m\nu}. \tag{B.2.10}$$

If all atoms are in their equilibrium positions this force must be zero, that is, in the harmonic approximation we obtain the expression of force

$$F^{\alpha}_{\ell\mu} = -\sum_{m\nu}\sum_{\beta} V^{\alpha\beta}_{\ell\mu m\nu} u^{\beta}_{m\nu}, \tag{B.2.11}$$

from equation (B.2.10).

The equation of motion for $u^{\beta}_{m\nu}$ is given by

$$M_{\mu}\ddot{u}^{\alpha}_{\ell\mu} = -\sum_{m\nu}\sum_{\beta} V^{\alpha\beta}_{\ell\mu m\nu} u^{\beta}_{m\nu}. \tag{B.2.12}$$

The Hamiltonian for the atom is given by

$$\mathcal{H}_L = \sum_{\ell\mu}\sum_{\alpha}\frac{P^{\alpha 2}_{\ell\mu}}{2M_{\mu}} + \frac{1}{2}\sum_{\ell m}\sum_{\mu\nu}\sum_{\alpha\beta} V^{\alpha\beta}_{\ell\mu m\nu} u^{\alpha}_{\ell\mu} u^{\beta}_{m\nu}, \tag{B.2.13}$$

where momentum $P^{\alpha}_{\ell\mu}$ is conjugate to $u^{\alpha}_{\ell\mu}$. We note here that $P^{\alpha}_{\ell\mu}$ and $u^{\alpha}_{\ell\mu}$ satisfy the following commutation relation:

$$[u^{\alpha}_{\ell\mu}, P^{\beta}_{m\nu}] = i\hbar\delta_{\ell m}\delta_{\mu\nu}\delta_{\alpha\beta}. \tag{B.2.14}$$

Introducing the Fourier transforms for the infinitesimal displacement and moment

$$\begin{aligned} \boldsymbol{u}_{\ell\mu} &= \frac{1}{\sqrt{N}}\sum_{\boldsymbol{q}} \mathrm{e}^{i\boldsymbol{q}\cdot\boldsymbol{R}_{\ell}}\boldsymbol{u}^{\boldsymbol{q}}_{\mu} \\ \boldsymbol{P}_{\ell\mu} &= \frac{1}{\sqrt{N}}\sum_{\boldsymbol{q}} \mathrm{e}^{i\boldsymbol{q}\cdot\boldsymbol{R}_{\ell}}\boldsymbol{P}^{\boldsymbol{q}}_{\mu}, \end{aligned} \tag{B.2.15}$$

and assuming the time dependence of u_μ^q as $e^{i\omega t}$, we obtain the secular equation given by substitute (B.2.15) for (B.2.12) as

$$\sum_{\mu\beta}\left[D_{\mu\nu}^{\alpha\beta}(\boldsymbol{q})-M_\mu\omega^2\delta_{\mu\nu}\delta_{\alpha\beta}\right]u_\nu^\beta(\boldsymbol{q})=0, \tag{B.2.16}$$

where the matrix $D(\boldsymbol{q})$ is called the dynamical matrix and its matrix elements is defined by

$$D_{\mu\nu}^{\alpha\beta}(\boldsymbol{q})=\sum_{\ell-m}V_{\ell\mu m\nu}^{\alpha\beta}e^{i\boldsymbol{q}\cdot(\boldsymbol{R}_\ell-\boldsymbol{R}_m)}. \tag{B.2.17}$$

And we can obtain the Hamiltonian in reciprocal space given by substitute (B.2.15) for (B.2.13) as

$$\mathcal{H}_L=\sum_{\boldsymbol{q}}\left[\sum_{\mu\alpha}\frac{P_\mu^{\alpha 2}}{2M_\mu}+\frac{1}{2}\sum_{\mu\nu}\sum_{\alpha\beta}D_{\mu\nu}^{\alpha\beta}(\boldsymbol{q})u_\mu^{q\alpha}u_\nu^{q\beta}\right], \tag{B.2.18}$$

By solving the secular equation (B.2.16), we obtain the frequency and the polarization vector of phonons. Therefore, our interest move to diagonalize the matrix

$$\frac{1}{\sqrt{M_\mu}}D_{\mu\nu}^{\alpha\beta}(\boldsymbol{q})\frac{1}{\sqrt{M_\nu}}. \tag{B.2.19}$$

If we express the infinitesimal displacement $u_\mu^{q\alpha}$ in terms of the phonon normal coordinate $Q_\gamma(\boldsymbol{q})$ as

$$u_\mu^{q\alpha}=\frac{1}{\sqrt{M_\mu}}\sum_\gamma\varepsilon_{\mu\alpha,\gamma}^{q}Q_\gamma(\boldsymbol{q}), \tag{B.2.20}$$

where γ is expressed the vibrational mode index. Then the Hamiltonian of lattice part (B.2.13) is expressed in the following form:

$$\mathcal{H}_L=\sum_{q\gamma}\left[\frac{1}{2}S_\gamma(\boldsymbol{q})S_\gamma(-\boldsymbol{q})+\frac{1}{2}Q_\gamma(\boldsymbol{q})Q_\gamma(-\boldsymbol{q})\omega_{q\gamma}^2\right] \tag{B.2.21}$$

where $S_\gamma(\boldsymbol{q})$ represents the momentum operator conjugate to $Q_\gamma(\boldsymbol{q})$, and then $S_\gamma(\boldsymbol{q})$ and $Q_\gamma(\boldsymbol{q})$ satisfy the relation

$$[Q_\gamma(\boldsymbol{q}),S_{\gamma'}(\boldsymbol{q}')]=i\hbar\delta_{\boldsymbol{q}\boldsymbol{q}'}\delta_{\gamma\gamma'}. \tag{B.2.22}$$

Finaly we introduce the annihilation and the creation operators defined by

$$\begin{aligned} S_\gamma(\boldsymbol{q}) &= -i\sqrt{\frac{\hbar}{2\omega_{\boldsymbol{q}\gamma}}}(a_{-\boldsymbol{q}\gamma} - a^\dagger_{\boldsymbol{q}\gamma}) \\ Q_\gamma(\boldsymbol{q}) &= \sqrt{\frac{\hbar}{2\omega_{\boldsymbol{q}\gamma}}}(a_{\boldsymbol{q}\gamma} + a^\dagger_{-\boldsymbol{q}\gamma}), \end{aligned} \tag{B.2.23}$$

with the bosonic commutation relations

$$[a_{\boldsymbol{q}\gamma}, a^\dagger_{\boldsymbol{q}'\gamma'}] = i\hbar\delta_{\boldsymbol{q}\boldsymbol{q}'}\delta_{\gamma\gamma'}, \quad [a^\dagger_{\boldsymbol{q}\gamma}, a^\dagger_{\boldsymbol{q}'\gamma'}] = 0, \quad [a_{\boldsymbol{q}\gamma}, a_{\boldsymbol{q}'\gamma'}] = 0.$$

Then the Hamiltonian (B.2.21) is rewritten as

$$\mathcal{H}_L = \sum_{\boldsymbol{q}\gamma} \hbar\omega_{\boldsymbol{q}\gamma}(a^\dagger_{\boldsymbol{q}\gamma}a_{\boldsymbol{q}\gamma} + \frac{1}{2}). \tag{B.2.24}$$

B.2.2 Density Functional Perturbation Theory

We discuss the density functional perturbation theory (DFPT)[33] in this section. The study of response coefficients of solids or derivatives of total energy has often performed, in the framework of DFT. The aim of this section we obtain the second derivative of the total energy with respect to atomic infinitesimal distortion to prepare for the LR-LMTO method. The adiabatic potential in solids expressed as the second derivative of the total energy for electronic system.

Let us consider one perturbation, associated with a small parameter λ, i.e. in this case atomic displacement. For a generic observable of the system $X(\lambda)$, we write the perturbation series as follows:

$$X(\lambda) = X^{(0)} + \lambda X^{(1)} + \lambda^2 X^{(2)} + \lambda^3 X^{(3)} + \cdots. \tag{B.2.25}$$

The expansion coefficients are no the derivatives of $X(\lambda)$ with respect to λ, but are related to them by a simple numerical coefficient:

$$X^{(n)} = \frac{1}{n!}\frac{d^n X}{d\lambda^2}\bigg|_{\lambda=0} \tag{B.2.26}$$

The applied potential $V(\boldsymbol{r})$, external to the electronic system, is supposed known through all orders, while it is our aim to calculate the perturbation expansion of other quantities, such as the energy E or the density $\rho(\boldsymbol{r})$.

Perturbation expansion of Kohn–Sham equation

In the LMTO method, the wave function is given by linear combinations of LMTO's as described above equation (2.1.8). For simplicity, in this section, we represent that wave function as follows:

$$|\psi_i\rangle = \sum_\alpha A^i_\alpha |\chi_\alpha\rangle, \tag{B.2.27}$$

where i denotes k-points and bands λ, and α includes κ, R, L explained in 2.1. Note here, we omit $\boldsymbol{k}$ which on the shoulder of χ_α. Since we can make an Bloch state at an certain wave vector $\boldsymbol{k}$, we define $|\chi_\alpha\rangle$ is an Bloch wave which has same $\boldsymbol{k}$ at the shoulder of expansion coefficients A^i_α. The total energy is then considered as a functional of only the expansion coefficients A^i_α, which are found by applying the Rayleigh-Ritz variational principle. We rewrite the Kohn-Sham type eigenvalue problem at (2.1.9) as

$$\sum_\beta \langle\chi_\alpha|\mathcal{H}_{\mathrm{KS}} - \varepsilon_i|\chi_\beta\rangle A^i_\beta = 0, \tag{B.2.28}$$

with the normalization condition

$$\int \psi_i(\boldsymbol{r})\psi_i(\boldsymbol{r})\mathrm{d}\boldsymbol{r} = \langle\psi_i|\psi_i\rangle = 1. \tag{B.2.29}$$

Now we perform the perturbative development by using equation (B.2.25) for those quantities. The equation (B.2.29) become, at order i

$$\sum_{j=0}^{m} \langle\psi_i^{(j)}|\psi_i^{(m-j)}\rangle = 0, \tag{B.2.30}$$

and premultiplying equation (B.2.28) by $\sum A^i_\alpha$

$$\sum_{j=0}^{m}\sum_{k=0}^{m} \langle\psi_i^{(j)}|\left(\mathcal{H}-\varepsilon_i\right)^{(m-j-k)}|\psi_i^{(k)}\rangle = 0, \tag{B.2.31}$$

here the Hamiltonian is expanded as

$$\mathcal{H} = \mathcal{H}^{(0)} + \lambda\mathcal{H}^{(1)} + \lambda^2\mathcal{H}^{(2)} + \cdots = \mathcal{H}_{\mathrm{KS}} + \lambda V^{(1)}_{\mathrm{eff}} + \lambda^2 V^{(2)}_{\mathrm{eff}}. \tag{B.2.32}$$

where V_{eff} is the effective potential. At 0th order, it given as

$$V_{\mathrm{eff}} = V_{\mathrm{ext}} + \int \frac{\rho(\boldsymbol{r}')}{|\boldsymbol{r}-\boldsymbol{r}'|}\mathrm{d}\boldsymbol{r}' + \mu_{\mathrm{xc}}, \qquad \text{with } \mu_{\mathrm{xc}} = \frac{\delta E_{\mathrm{xc}}}{\delta\rho}. \tag{B.2.33}$$

To shorten the notations, we will sometimes omit (0) at $X^{(0)}$. From this expansion, the first-order and second-order derivative in the eigenvalues are given by

$$\varepsilon_i^{(1)} = \{\langle\psi_i|\mathcal{H}_{\rm KS} - \varepsilon_i|\psi_i^{(1)}\rangle + \text{c.c.}\} + \langle\psi_i|V_{\rm eff}^{(1)}|\psi_i\rangle \tag{B.2.34}$$

$$\begin{aligned}\varepsilon_i^{(2)} &= \{\langle\psi_i|\mathcal{H}_{\rm KS} - \varepsilon_i|\psi_i^{(2)}\rangle + \text{c.c.}\} + \{\langle\psi_i|V_{\rm eff}^{(1)}|\psi_i^{(1)}\rangle + \text{c.c.}\} \\ &\quad + \langle\psi_i^{(1)}|\mathcal{H}_{\rm KS} - \varepsilon_i|\psi_i^{(1)}\rangle + \langle\psi_i|V_{\rm eff}^{(2)}|\psi_i\rangle.\end{aligned} \tag{B.2.35}$$

Perturbation expansion of total energy

The LDA total energy is given by the standard expression

$$E = \sum_i f_i\varepsilon_i - \int V_{\rm eff}\rho \mathrm{d}\boldsymbol{r} + \int V_{\rm ext}\rho \mathrm{d}\boldsymbol{r} + \frac{1}{2}\int \frac{\rho\rho'}{|\boldsymbol{r}-\boldsymbol{r}'|}\mathrm{d}\boldsymbol{r}\mathrm{d}\boldsymbol{r}' + E_{\rm xc} \tag{B.2.36}$$

where f_i is the occupation number of ith band and E_{xc} is the exchange-correlation functional as given by LDA. The expansion of E_{xc} can obtain easily as

$$\begin{aligned}E_{\rm xc} &= \int \varepsilon_{\rm xc}\rho \mathrm{d}\boldsymbol{r} \\ E_{\rm xc}^{(1)} &= \int \mu_{\rm xc}\rho^{(1)}\mathrm{d}\boldsymbol{r} \\ E_{\rm xc}^{(2)} &= \int \mu_{\rm xc}\rho^{(2)}\mathrm{d}\boldsymbol{r} + \frac{1}{2}\int \mu_{\rm xc}^{(1)}\rho^{(1)}\mathrm{d}\boldsymbol{r},\end{aligned} \tag{B.2.37}$$

where $\mu_{\rm xc}$ and $\mu_{\rm xc}^{(1)}$ is given by

$$\mu_{\rm xc} = \varepsilon_{\rm xc} + \rho\left.\frac{\mathrm{d}\varepsilon_{\rm xc}}{\mathrm{d}\rho}\right|_{\rho=\rho(\boldsymbol{r})} \quad \text{and} \quad \mu_{\rm xc}^{(1)} = \rho^{(1)}\left(2\left.\frac{\mathrm{d}\varepsilon_{\rm xc}}{\mathrm{d}\rho}\right|_{\rho=\rho(\boldsymbol{r})} + \rho\left.\frac{\mathrm{d}^2\varepsilon_{\rm xc}}{\mathrm{d}\rho^2}\right|_{\rho=\rho(\boldsymbol{r})}\right). \tag{B.2.38}$$

To obtain first-order derivative of the total energy with respect to atomic displacement, we apply the expansion of (B.2.25).

$$\begin{aligned}E^{(1)} &= \sum_i\{f_i\varepsilon_i^{(1)} + f_i^{(1)}\varepsilon_i\} - \int(V_{\rm eff}\rho^{(1)} + V_{\rm eff}^{(1)}\rho)\mathrm{d}\boldsymbol{r} \\ &\quad + \int(V_{\rm ext}\rho^{(1)} + V_{\rm ext}^{(1)}\rho)\mathrm{d}\boldsymbol{r} + \int\frac{\rho^{(1)}\rho'}{|\boldsymbol{r}-\boldsymbol{r}'|}\mathrm{d}\boldsymbol{r}\mathrm{d}\boldsymbol{r}' + \int\mu_{\rm xc}\rho^{(1)}\mathrm{d}\boldsymbol{r}\end{aligned} \tag{B.2.39}$$

According to the electron number conservation condition the term containing the first-order derivative in the occupation numbers vanishes, i.e.

$$\sum_i f_i^{(1)}\varepsilon_i = \sum_i \varepsilon_i\delta(\varepsilon_F - \varepsilon_i)(\varepsilon_F^{(1)} - \varepsilon_i^{(1)}) = \varepsilon_F N_{\rm valence}^{(1)} = 0. \tag{B.2.40}$$

Insert the first-order derivative in the eigenvalues (B.2.34) to equation (B.2.39). We obtain the following expression for the first-order derivative in the total energy

$$E^{(1)} = \sum_i f_i\{\langle\psi_i|\mathcal{H}_{\rm KS}-\varepsilon_i|\psi_i^{(1)}\rangle + \text{c.c.}\} + \int V_{\rm ext}^{(1)}\rho \mathrm{d}\boldsymbol{r} + \int\left\{V_{\rm ext} + \int\frac{\rho'}{|\boldsymbol{r}-\boldsymbol{r}'|}\mathrm{d}\boldsymbol{r}' + \mu_{\rm xc} - V_{\rm eff}\right\}\rho^{(1)}\mathrm{d}\boldsymbol{r}. \quad \text{(B.2.41)}$$

If the electron density is self-consistent, the expression in curly brackets of the integral with $\rho^{(1)}$ is equal to zero, and the obtained result is known as the Hellmann-Feynman force plus the incomplete-basis-set (or Pulay) correction [first contribution in (B.2.41)]. If the lattice in the equilibrium position, $E^{(1)}$ is equal to zero.

The second-order derivative, $E^{(2)}$, which is expressed via the dynamical matrix of a solid, is found by performing one more expansion of Eq.(B.2.25)

$$\begin{aligned} E^{(2)} = {} & \sum_i\{f_i\varepsilon_i^{(2)} + f_i^{(1)}\varepsilon_i^{(1)} + f_i^{(2)}\varepsilon_i\} - \int(V_{\rm eff}\rho^{(2)} + V_{\rm eff}^{(1)}\rho^{(1)} + V_{\rm eff}^{(2)}\rho)\mathrm{d}\boldsymbol{r} \\ & + \int(V_{\rm ext}\rho^{(2)} + V_{\rm ext}^{(1)}\rho^{(1)} + V_{\rm ext}^{(2)}\rho)\mathrm{d}\boldsymbol{r} + \int\frac{\rho^{(2)}\rho'}{|\boldsymbol{r}-\boldsymbol{r}'|}\mathrm{d}\boldsymbol{r}\mathrm{d}\boldsymbol{r}' \\ & + \frac{1}{2}\int\frac{\rho^{(1)}\rho'^{(1)}}{|\boldsymbol{r}-\boldsymbol{r}'|}\mathrm{d}\boldsymbol{r}\mathrm{d}\boldsymbol{r}' + \int\mu_{\rm xc}\rho^{(2)}\mathrm{d}\boldsymbol{r} + \frac{1}{2}\int\mu_{\rm xc}^{(1)}\rho^{(1)}\mathrm{d}\boldsymbol{r}. \end{aligned} \quad \text{(B.2.42)}$$

Since we have proved that $\varepsilon^{(1)} = 0$, then $f_i^{(1)} = \delta(\varepsilon_F - \varepsilon_i)(\varepsilon_F^{(1)} - \varepsilon_i^{(1)})$ is also equal to zero. The contribution in in (B.2.42) from the second-order derivative in the occupation numbers reads

$$\begin{aligned} \sum_i f_i^{(2)}\varepsilon_i = {} & \sum_i \varepsilon_i\{\varepsilon_F^{(1)} - \varepsilon_i^{(1)}\}^2\frac{\mathrm{d}}{\mathrm{d}\varepsilon_F}\delta(\varepsilon_F - \varepsilon_i) \\ & + \varepsilon_F\sum_i\delta(\varepsilon_F - \varepsilon_i)\{\varepsilon_F^{(2)} - \varepsilon_i^{(2)}\}. \end{aligned} \quad \text{(B.2.43)}$$

Since $\varepsilon_F^{(1)} = \varepsilon_i^{(1)} = 0$, the whole expression is equal to $\varepsilon_F N_{\rm valence}^{(2)} = 0$. Thus we can omit the contributions from the derivative in the occupation numbers. Insert the second-order derivative in the eigenvalues (B.2.35) to equation (B.2.42). We obtain the following expression for the second-order derivative in the total energy

$$\begin{aligned} E^{(2)} = {} & \sum_i f_i\{\langle\psi_i|\mathcal{H}_{\rm KS}-\varepsilon_i|\psi_i^{(2)}\rangle + \text{c.c.}\} + \sum_i f_i\langle\psi_i^{(1)}|\mathcal{H}_{\rm KS}-\varepsilon_i|\psi_i^{(1)}\rangle \\ & + \frac{1}{2}\int V_{\rm ext}^{(1)}\rho^{(1)}\mathrm{d}\boldsymbol{r} + \int V_{\rm ext}^{(2)}\rho\mathrm{d}\boldsymbol{r} + \frac{1}{2}\int V_{\rm eff}^{(1)}\rho^{(1)}\mathrm{d}\boldsymbol{r} \end{aligned} \quad \text{(B.2.44)}$$

$$+\int\left\{V_{\text{ext}}+\int\frac{\rho'}{|\boldsymbol{r}-\boldsymbol{r}'|}\mathrm{d}\boldsymbol{r}'+\mu_{\text{xc}}-V_{\text{eff}}\right\}\rho^{(2)}\mathrm{d}\boldsymbol{r} \tag{B.2.45}$$

where the last integral with $\rho^{(2)}$ can be dropped since the expression in curly brackets is equal to zero if the unperturbed charge density is self-consistent.

The final expression for the second-order derivative in the total energy is given by

$$\begin{aligned}E^{(2)} &= \sum_i f_i\{\langle\psi_i|\mathcal{H}_{\text{KS}}-\varepsilon_i|\psi_i^{(2)}\rangle+\text{c.c.}\}+\sum_i f_i\langle\psi_i^{(1)}|\mathcal{H}_{\text{KS}}-\varepsilon_i|\psi_i^{(1)}\rangle \\ &\quad +\frac{1}{2}\int V_{\text{ext}}^{(1)}\rho^{(1)}\mathrm{d}\boldsymbol{r}+\int V_{\text{ext}}^{(2)}\rho\mathrm{d}\boldsymbol{r}+\frac{1}{2}\int V_{\text{eff}}^{(1)}\rho^{(1)}\mathrm{d}\boldsymbol{r}\end{aligned} \tag{B.2.46}$$

B.2.3 Density-functional linear response

Within DFT, the problem of calculating the lattice dynamics essentially amounts to finding the change in the electronic charge density induced by the presence of a phonon with wave vector $\boldsymbol{q}$. We use the same notation as previous section for positions of atom $\boldsymbol{R}_{\ell\mu}$, the translation vectors $\boldsymbol{t}$ and the small atomic displacement $\boldsymbol{u}_{\ell\mu}$. We suppose that the atoms are displaced from their equilibrium positions by a small amount:

$$\boldsymbol{u}_{\ell\mu}=\boldsymbol{u}_\mu^{\boldsymbol{q}}\mathrm{e}^{\mathrm{i}\boldsymbol{q}\cdot\boldsymbol{R}_\ell}+\boldsymbol{u}_\mu^{\boldsymbol{q}*}\mathrm{e}^{-\mathrm{i}\boldsymbol{q}\cdot\boldsymbol{R}_\ell}, \tag{B.2.47}$$

where $\boldsymbol{u}_\mu^{\boldsymbol{q}}$ is a complex polarization vector and $\boldsymbol{q}$ is the phonon wave vector. Now we extend small parameter λ in equation (B.2.25) to three-dimension small displacement of atom, *i.e.* $\boldsymbol{u}_{\ell\mu}$. Thus we can define the first and second-order change of the certain quantities as follows:

$$\delta X=\sum_{\ell\mu}\boldsymbol{u}_{\ell\mu}X^{(1)},\quad \delta^2X=\sum_{\ell\mu}\sum_{m\nu}\boldsymbol{u}_{\ell\mu}\boldsymbol{u}_{m\nu}X^{(2)}. \tag{B.2.48}$$

The external fields after displacement is represented as

$$V_{\text{ext}}(\boldsymbol{r})=\sum_{m\nu}\frac{-Z_\nu\mathrm{e}^2}{|\boldsymbol{r}-\boldsymbol{R}_{m\nu}^0-\boldsymbol{u}_{m\nu}|}, \tag{B.2.49}$$

where Z_μ are the nuclei charges. By expanding this expression to first order in the displacements, we obtain that the static external field perturbs the crystal

$$\begin{aligned}\delta V_{\text{ext}} &= \sum_{\ell\mu}\boldsymbol{u}_{\ell\mu}V_{\text{ext}}^{(1)}=\sum_{\ell\mu}\boldsymbol{u}_{\ell\mu}\frac{\partial}{\partial\boldsymbol{R}_{\ell\mu}}\sum_{m\nu}\frac{-Z_\nu\mathrm{e}^2}{|\boldsymbol{r}-\boldsymbol{R}_{m\nu}|}\bigg|_{\boldsymbol{R}_{\ell\mu}=\boldsymbol{R}_{\ell\mu}^0} \\ &= \sum_\mu\{\boldsymbol{u}_\mu^{\boldsymbol{q}}\delta^+V_{\text{ext}}+\boldsymbol{u}_\mu^{\boldsymbol{q}*}\delta^-V_{\text{ext}}\}.\end{aligned} \tag{B.2.50}$$

where

$$\delta^{\pm}V_{\text{ext}} = \sum_{\ell} \mathrm{e}^{\pm \mathrm{i}\boldsymbol{q}\cdot\boldsymbol{R}_{\ell}} \frac{\partial}{\partial \boldsymbol{R}_{\ell\mu}} \frac{-Z_{\mu}\mathrm{e}^2}{|\boldsymbol{r}-\boldsymbol{R}_{\ell\mu}|}\bigg|_{\boldsymbol{R}_{\ell\mu}=\boldsymbol{R}^0_{\ell\mu}}. \tag{B.2.51}$$

δV_{ext} is represented as a superposition of two traveling waves with wave vectors $\pm\boldsymbol{q}$. The first-order changes in the charge density, effective potential (B.2.33) and the first-order correction of the wave function (B.2.27) induced by the perturbation (B.2.50) is represented in the same way by using first-order derivative

$$\begin{aligned}
\rho^{(1)} &= \sum_i f_i\{\psi_i^{(1)*}\psi_i + \psi_i^*\psi_i^{(1)}\} \\
V_{\text{eff}}^{(1)} &= V_{\text{ext}}^{(1)} + \int \frac{\rho'^{(1)}}{|\boldsymbol{r}-\boldsymbol{r}'|}\mathrm{d}\boldsymbol{r}' + \mu_{\text{xc}}^{(1)} \\
\psi_i^{(1)} &= \frac{\partial}{\partial \boldsymbol{R}_{\ell\mu}}\psi_i\bigg|_{\boldsymbol{R}_{\ell\mu}=\boldsymbol{R}^0_{\ell\mu}}.
\end{aligned}$$

Then

$$\delta\rho = \sum_{\ell\mu} \boldsymbol{u}_{\ell\mu}\rho^{(1)} = \sum_{\mu}\{\boldsymbol{u}_{\mu}^{q}\delta^{+}\rho + \boldsymbol{u}_{\mu}^{q*}\delta^{-}\rho\} \tag{B.2.52}$$

$$\delta V_{\text{eff}} = \sum_{\ell\mu} \boldsymbol{u}_{\ell\mu}V_{\text{eff}}^{(1)} = \sum_{\ell}\{\boldsymbol{u}_{\mu}^{q}\delta^{+}V_{\text{eff}} + \boldsymbol{u}_{\mu}^{q}\delta^{-}V_{\text{eff}}\} \tag{B.2.53}$$

$$\delta\psi_i = \sum_{\ell\mu} \boldsymbol{u}_{\ell\mu}\psi^{(1)} = \sum_{\mu}\{\boldsymbol{u}_{\mu}^{q}\delta^{+}\psi_i + \boldsymbol{u}_{\mu}^{q*}\delta^{-}\psi_i\}, \tag{B.2.54}$$

where

$$\delta^{\pm}\rho = \sum_i f_i(\delta^{\pm}\psi_i^*\psi_i + \psi_i^*\delta^{\pm}\psi_i) \tag{B.2.55}$$

$$\delta^{\pm}V_{\text{eff}} = \delta^{\pm}V_{\text{ext}} + \int \frac{\delta^{\pm}\rho'}{|\boldsymbol{r}-\boldsymbol{r}'|}\mathrm{d}\boldsymbol{r}' + \delta^{\pm}\rho\,\frac{\mathrm{d}\mu_{xc}}{\mathrm{d}\rho}\bigg|_{\rho=\rho(\boldsymbol{r})} \tag{B.2.56}$$

$$\delta^{\pm}\psi_i = \sum_{\ell} \mathrm{e}^{\pm \mathrm{i}\boldsymbol{q}\cdot\boldsymbol{R}_{\ell}} \frac{\partial}{\partial \boldsymbol{R}_{\ell\mu}}\psi_i\bigg|_{\boldsymbol{R}_{\ell\mu}=\boldsymbol{R}^0_{\ell\mu}}. \tag{B.2.57}$$

The exchange-correlation effects are taken into account in the LDA. The first-order correction of wave function $\delta^{\pm}\psi_i \equiv |\delta^{\pm}\psi_i\rangle$ is a Bloch wave with vector $\boldsymbol{k}+\boldsymbol{q}$ (will define appropriate in Section B.2.5) and it is the solution of the Sternheimer equation[34], which is the Schrödinger equation to linear order in the reciprocal space

$$(-\nabla^2 + V_{\text{eff}} - \varepsilon_i)|\delta^{\pm}\psi_i\rangle + \delta^{\pm}V_{\text{eff}}|\psi_i\rangle = 0. \tag{B.2.58}$$

We have dropped the term with the first-order corrections to the one electron energies which are equal to zero if $\boldsymbol{q} \neq 0$. Now we have to solve the induced charge density at self-consistently. A brief view as follows: (i) Solve the equation (B.2.58) with the external perturbation $\delta^{\pm}V_{\text{eff}}$, (ii) define the induced charge density according to (B.2.55) and (iii) find a new $\delta^{\pm}V_{\text{eff}}$ after (B.2.56). Steps (i)–(iii) are repeated until input and output $\delta^{\pm}\rho$ coincide within a required accuracy.

B.2.4 Dynamical Matrix

To see the equation (B.2.46), there is two undefined quantities, *i.e.* second-order change in V_{ext} and wave function ψ_i. Changes in the second-order are easy to find by using Eq.(B.2.48)

$$\begin{aligned}\delta^2 V_{\text{ext}} &= \sum_{\ell\mu}\sum_{m\nu} \boldsymbol{u}_{\ell\mu}\boldsymbol{u}_{m\nu} V^{(2)}_{\text{ext}} = \sum_{\ell\mu}\sum_{m\nu} \boldsymbol{u}_{\ell\mu}\boldsymbol{u}_{m\nu} \frac{\partial^2}{\partial \boldsymbol{R}_{\ell\mu}\partial \boldsymbol{R}_{m\nu}} \sum_{n\lambda} \frac{-Z_\lambda \mathrm{e}^2}{|\boldsymbol{r}-\boldsymbol{R}_{n\lambda}|}\bigg|_{\boldsymbol{R}=\boldsymbol{R}^0} \\ &= \sum_{\mu\nu}\{\boldsymbol{u}^{\boldsymbol{q}}_\mu \boldsymbol{u}^{\boldsymbol{q}}_\nu \delta^+\delta^+ V_{\text{ext}} + \boldsymbol{u}^{\boldsymbol{q}}_\mu \boldsymbol{u}^{\boldsymbol{q}*}_\nu \delta^+\delta^- V_{\text{ext}}\} + \text{c.c.}, \end{aligned} \tag{B.2.59}$$

where

$$\delta^+\delta^+ V_{\text{ext}} = \delta_{\mu\nu}\sum_\ell \mathrm{e}^{2\mathrm{i}\boldsymbol{q}\cdot\boldsymbol{R}_\ell} \frac{\partial^2}{\partial \boldsymbol{R}_{\ell\mu}\partial \boldsymbol{R}_{\ell\nu}} \frac{-Z\mathrm{e}^2}{|\boldsymbol{r}-\boldsymbol{R}_{\ell\nu}|}\bigg|_{\boldsymbol{R}=\boldsymbol{R}^0} \tag{B.2.60}$$

$$\delta^+\delta^- V_{\text{ext}} = \delta_{\mu\nu}\sum_\ell \frac{\partial^2}{\partial \boldsymbol{R}_{\ell\mu}\partial \boldsymbol{R}_{\ell\nu}} \frac{-Z\mathrm{e}^2}{|\boldsymbol{r}-\boldsymbol{R}_{\ell\nu}|}\bigg|_{\boldsymbol{R}=\boldsymbol{R}^0}. \tag{B.2.61}$$

It is directly seen that the variation $\delta^+\delta^- V_{\text{ext}}$ is a periodical function at the original lattice while the function $\delta^+\delta^+ V_{\text{ext}}$ translates like a wave of wave vector $2\boldsymbol{q}$. For the wave function we can same expansion as

$$|\delta^2\psi_i\rangle = \sum_{\mu\nu}\{\boldsymbol{u}^{\boldsymbol{q}}_\mu \boldsymbol{u}^{\boldsymbol{q}}_\nu |\delta^+\delta^+\psi_i\rangle + \boldsymbol{u}^{\boldsymbol{q}}_\mu \boldsymbol{u}^{\boldsymbol{q}*}_\nu |\delta^+\delta^-\psi_i\rangle\} + \text{c.c.}. \tag{B.2.62}$$

Using above relation and the equation (B.2.46) we can obtain the second-order change of total energy

$$\begin{aligned}\delta^2 E = \sum_{\mu\nu} \boldsymbol{u}^{\boldsymbol{q}}_\mu \boldsymbol{u}^{\boldsymbol{q}*}_\nu \Bigg[&\sum_i f_i\langle \delta^+\delta^-\psi_i + \delta^-\delta^+\psi_i | \mathcal{H}-\varepsilon_i|\psi_i\rangle + \sum_i f_i\langle \delta^+\psi_i|\mathcal{H}-\varepsilon_i|\delta^-\psi_i\rangle \\ &+ \frac{1}{2}\int \delta^+ V_{\text{ext}}\delta^-\rho \mathrm{d}\boldsymbol{r} + \int \delta^+\delta^- V_{\text{ext}}\rho \mathrm{d}\boldsymbol{r} + \frac{1}{2}\int \delta^+ V_{\text{eff}}\delta^-\rho \mathrm{d}\boldsymbol{r}\Bigg] + \text{c.c.}. \end{aligned} \tag{B.2.63}$$

We see that this expression does not contain the second-order contributions with wave vectors $\pm 2\boldsymbol{q}$. $\delta^{\pm}\delta^{\mp}\psi_i$ are the functions of wave vector $\boldsymbol{k}$ and only they contribute to the matrix elements with ψ_i. $\delta^{\pm}\delta^{\mp}V_{\rm ext}$ is periodical and only this gives a nonzero contribution to the integral with ρ. Finally, we arrive at the expression for the dynamical matrix defined in (B.2.43).

$$\begin{aligned} D^{\alpha\beta}_{\mu\nu}(\boldsymbol{q}) &= \sum_i f_i \langle \delta^+\delta^-\psi_i + \delta^-\delta^+\psi_i | \mathcal{H} - \varepsilon_i | \psi_i \rangle + \sum_i 2 f_i \langle \delta^+\psi_i | \mathcal{H} - \varepsilon_i | \delta^-\psi_i \rangle \\ &\quad + \int \delta^+ V_{\rm ext} \delta^- \rho \mathrm{d}\boldsymbol{r} + \int \delta^+\delta^- V_{\rm ext} \rho \mathrm{d}\boldsymbol{r} + \int \delta^+ V_{\rm eff} \delta^- \rho \mathrm{d}\boldsymbol{r}. \end{aligned} \tag{B.2.64}$$

Note here, the difference of the coefficient 2nd, 3rd and 5th in Eqs.(B.2.63) (B.2.64) caused by different definition of perturbational expansions.

B.2.5 First-order corrections

This section we construct the basis functions which represent the first-order perturbations. The unperturbed wave function given in Eq.(B.2.27) is expanded in terms of the MT basis set $|\chi_\alpha\rangle$. We perform the same perturbational expansion for Eqs.(B.2.57) (B.2.62)

$$|\delta^{\pm}\psi_{k\lambda}\rangle = \sum_\alpha \{ A^{k\lambda}_\alpha |\delta^{\pm}\chi^{k}_\alpha\rangle + \delta^{\pm}A^{k\lambda}_\alpha |\chi^{k+q}_\alpha\rangle \} \tag{B.2.65}$$

$$\begin{aligned} |\delta^{\pm}\delta^{\mp}\psi_{k\lambda}\rangle &= \sum_\alpha \{ A^{k\lambda}_\alpha |\delta^{\pm}\delta^{\mp}\chi^{k}_\alpha\rangle + \delta^{\pm}A^{k\lambda}_\alpha |\delta^{\mp}\chi^{k\pm q}_\alpha\rangle \\ &\quad + \delta^{\mp}A^{k\lambda}_\alpha |\delta^{\pm}\chi^{k\mp q}_\alpha\rangle + \delta^{\pm}\delta^{\mp}A^{k\lambda}_\alpha |\chi^{k}_\alpha\rangle \}. \end{aligned} \tag{B.2.66}$$

Note here, we recover the omitted wave vector for χ in Eq.(B.2.27). In equation (B.2.65) the first term is the change in the MT orbital due to the movements of atoms and the second one is the original linear MT orbital of wave vector $\boldsymbol{k} \pm \boldsymbol{q}$. By inserting (B.2.66) in the first term of (B.2.63) and (B.2.64) we see that the second-order changes $\delta^{\pm}\delta^{\mp}A^{k\lambda}_\alpha$ do not contribute because they enter as coefficients to due the unperturbed basis functions and

$$\sum_\alpha \delta^{\pm}\delta^{\mp}A^{k\lambda}_\alpha \langle \chi^{k}_\alpha | \mathcal{H}_{\rm KS} - \varepsilon_{k\lambda} | \psi_{k\lambda}\rangle = 0. \tag{B.2.67}$$

The absence of the coefficients $\delta^{\pm}\delta^{\mp}A^{i}_\alpha$ has an important consequence. Since $|\delta^{\pm}\delta^{\mp}\psi_i\rangle$ has only the unknown contribution from the first-order changes in A^{i}_α and since the Hilbert

space $\{|\chi_\alpha\rangle, |\delta\chi_\alpha\rangle\}$ of the basis functions is fixed, we see that the variational freedom of the functional (B.2.63) is provided only by the coefficients $\delta^\pm A^i_\alpha$. The variation of the Eq.(B.2.63) with respect to $\delta^\pm A^i_\alpha$ leads Sternheimaer equation plus the incomplete-basis-set correction

$$\sum_\alpha \langle \chi^{k\pm q}_\beta | \mathcal{H}_{\rm KS} - \varepsilon_{k\lambda} | \chi^{k\pm q}_\alpha \rangle \delta^\pm A^{k\lambda}_\alpha + \sum_\alpha \{ \langle \chi^{k\pm q}_\beta | \delta^\pm V_{\rm eff} | \chi^k_\alpha \rangle + \langle \delta^\pm \chi^{k\mp q}_\beta | \mathcal{H}_{\rm KS} - \varepsilon_{k\lambda} | \chi^k_\alpha \rangle + \langle \chi^{k\pm q}_\beta | \mathcal{H}_{\rm KS} - \varepsilon_{k\lambda} | \delta^\pm \chi^k_\alpha \rangle \} A^{k\lambda}_\alpha = 0. \tag{B.2.68}$$

This equation involves only the occupied states of the unperturbed system, which are necessary for constructing the induced charge density according to (B.2.55). It may be solved using an iterative algorithm with the number of operations proportional to $N_{\rm band} \times N^2_{\rm basis}$, where $N_{\rm band}$ is a number of filled bands and $N_{\rm basis}$ is a number of the basis functions used for representing the unperturbed wave functions and their first-order corrections. Because of the minimal size of the basis in the LMTO method, it is not a time-consuming step to find eigenvalue $\varepsilon_{k\lambda}$ and eigenvectors $A_{k\lambda}$ for all energy bands ($= N_{\rm basis}$) at some grid of wave vectors $\boldsymbol{k}$. The expression of the coefficient is given by solving Eq.(B.2.68) as

$$\delta^\pm A^{k\lambda}_\alpha = \sum_{\lambda'} \frac{A^{k\pm q\lambda'}_\alpha}{\varepsilon_{k\lambda} - \varepsilon_{k\pm q\lambda'}} \times \left\{ \sum_\beta A^{k\pm q\lambda'}_\beta \langle \delta^\pm \chi^{k\mp q}_\beta | \mathcal{H}_{\rm KS} - \varepsilon_{k\lambda} | \psi_{k\lambda} \rangle + \sum_\beta \langle \psi_{k\pm q\lambda} | \mathcal{H}_{\rm KS} - \varepsilon_{k\lambda} | \delta^\pm \chi^k_\beta \rangle A^{k\lambda}_\beta + \langle \psi_{k\pm q\lambda'} | \delta^\pm V_{\rm eff} | \psi_{k\lambda} \rangle \right\}. \tag{B.2.69}$$

Finally we obtain the expression for $|\psi_{k\lambda}\rangle$ by substituting (B.2.69) into (B.2.65)

$$|\delta^\pm \psi_{k\lambda}\rangle = \sum_\alpha A^{k\lambda}_\alpha |\delta^\pm \chi^k_\alpha\rangle + \sum_{\lambda'} \frac{|\psi_{k\pm q\lambda'}\rangle}{\varepsilon_{k\lambda} - \varepsilon_{k\pm q\lambda'}} \times \left\{ \sum_\alpha A^{k\pm q\lambda'}_\alpha \langle \delta^\pm \chi^{k\mp q}_\alpha | \mathcal{H}_{\rm KS} - \varepsilon_{k\lambda} | \psi_{k\lambda} \rangle + \sum_\alpha \langle \psi_{k\pm q\lambda} | \mathcal{H}_{\rm KS} - \varepsilon_{k\lambda} | \delta^\pm \chi^k_\alpha \rangle A^{k\lambda}_\alpha + \langle \psi_{k\pm q\lambda'} | \delta^\pm V_{\rm eff} | \psi_{k\lambda} \rangle \right\}. \tag{B.2.70}$$

The first three terms containing $|\delta\chi\rangle$ appear because of the use of incomplete-basis-set. If we use a complete basis set, then the fist and third terms in (B.2.70) cancel, the second term vanishes, and arises standard perturbative formula

$$|\delta^\pm \psi_{k\lambda}\rangle = \sum_{\lambda'} \frac{\langle \psi_{k\pm q\lambda'} | \delta^\pm V_{\rm eff} | \psi_{k\lambda} \rangle}{\varepsilon_{k\lambda} - \varepsilon_{k\pm q\lambda'}} |\psi_{k\pm q\lambda'}\rangle \tag{B.2.71}$$

Bibliography

[1] G.C. DeFotis, Phys. Rev B **23** (1981) 4714

[2] R.D. Etters, A.A. Helmy and K. Kobashi, Phys. Rev. B **28** (1983) 2166

[3] R.J. Meier and R.B. Helmholkt, Rhys. Rev. B **29** (1984) 1387

[4] P.W. Stephens and C.F. Majkrzak, Phys. Rev. B **33** (1986) 1

[5] S.W. Johnson, M. Nicol and D. Schiferl, J. Appl. Cryst. **26** (1993) 320

[6] A.L. Ruoff and S. Desgreniers, in *Molecular systems under high pressure*, ed. R. Pucci and G. Piccitto (Elsevier Science Publishers B.V., North-Holland, 1991) p 123

[7] S. Desgreniers, Y.K. Vohra and A.L. Ruoff, J. Phys. Chem. **94** (1990) 1117

[8] Y. Akahama, H. Kawamura, D. Häusermann and M. Hanfland, Phys. Rev. Lett. **74** (1995) 4690

[9] K. Shimizu, K. Suhara, K. Amaya, and S.Endo J. Phys. Soc. Jpn. **65** (1996) 1527

[10] K. Shimizu, K. Suhara, M. Ikumo M. Eremets and K. Amaya, Nature, **65**(1998) 767

[11] S. Serra, G. Chiarotti, S. Scandolo, and E. Tosatti, Phys. Rev. Lett. **80** (1998) 5160

[12] K. Kususe, Y. Hori, S. Suzuki and K. Nakao, J. Phys. Soc. Jpn. **68** (1999) 2692

[13] W. Mori, T.C. Kobayashi, J. Kurobe, K. Amaya, Y. Narumi, T. Kumada, K. Kindo, H.A. Katori, T. Goto, N. Miura, S. Takamizawa, H. Nakayama and K. Yamaguchi, Mol. Cryst. Liq. Cryst. **306** (1997) 587

[14] Y. Akahama, M. Kobayashi and H. Kawamura, Solid. State. Commun. **83** (1992) 273

[15] J.C. Jamieson and D.B. McWhan, J. Chem. Phys. **43** (1965) 1149

[16] G. Parthasarathy and W. B. Holzapfel, Phys. Rev. B **37** (1988) 8499

[17] H. Luo, R.G. Greene and A. L. Ruoff, Phys. Rev. Lett. **71** (1993) 2943

[18] Y. Akahama, M, Kobayshi and H. Kawamura, Solid State Commun. **84** (1992) 803

[19] Y. Akahama, M. Kobayashi and H. Kawamura, Phys. Rev. B **47** (1993) 20

[20] O. Zakharov and M.L. Cohen, Phys. Rev. B **52** (1995) 12572

[21] S.P. Rudin and A.Y. Liu, Phys. Rev. Lett. **83** (1999) 3049

[22] S. Kometani, M.I. Eremets, K. Shimizu, M. Kobayashi and K. Amaya, J. Phys. Soc. Jpn. **66** (1997) 2564

[23] V.V. Struzhkin, R.J. Hemley, H.K. Mao and Y.A Timofeev, Nature **390** (1997) 382

[24] F. Mauri, O. Zakhalov, S. de Gironcoli, S.G. Luie and M.L. Cohen, Phys. Rev. Lett. **77** (1996) 1151

[25] K. H. Weyrich, Phys. Rev. B **37** (1988) 10269

[26] M. Methfessel, C.O. Rodriguez and O.K. Andersen, Phys. Rev. B **40** (1988) 2009

[27] S.Yu. Savrasov and D.Yu. Savrasov, Phys. Rev. B **46** (1992) 12181

[28] P. Hoenberg and W. Kohn, Phys. Rev. **136** (1964) B864

[29] W. Kohn and L. J. Sham, Phys. Rev. **140** (1965) A1133

[30] E.U. Condon and G.H. Shortley, in *The Theory of Atomic Spectra* (Cambridge U.P., Cambridge, 1951)

[31] S.Yu. Savrasov, Phys. Rev. B **54** (1996) 16470

[32] S.Yu. Savrasov and D.Yu Savrasov, Phys. Rev. B **54** (1996) 16487

[33] X. Gonze and J.P. Vigneron, Phys. Rev. B **39** (1989) 13120

[34] R.M. Sternheimer, Phys. Rev. **107** (1957) 1565

[35] I.N. Krupskii, A.I. Prokhvatilov, A.F. Prikhot'ko and L.I. Shanskii, Sov. J. Low Temp. Phys. **5** (1979) 130

[36] D. Schiferl, D.T. Cromer, L.A. Schwalbe and R.L. Mills, Acta Cryst. B **39** (1983) 153

[37] O. Gunnarsson and B.I. Lundqvist, Phys. Rev. B **13** (1976) 4274

[38] P.E. Blöchel, O. Jepsen and O.K. Andersen, Phys. Rev. B **49** (1994) 16223

[39] M. Geshi, T. Oda and Y. Hiwatari, J. Phys. Soc. Jpn. **67** (1998) 3141

[40] A. Nishikawa, K. Niizeki and K. Shindo, Jpn. J. Appl. Phys. **32** (1993) Suppl. 32-1 48

[41] J.P. Perdew, K. Burke and Yu. Wang, Phys. Rev. B **54** (1996) 16533

[42] F.D. Murnaghan, Proc. Natl. Acad. Sci. U.S.A., **30** (1994) 244

[43] P.B. Allen and R.C. Dynes, Phys. Rev. B **12** (1975) 905

[44] G.M. Eliashberg, Zh. Éksp. Teor. Fiz. **38**, (1960) 966 [Sov. Phys. JETP **11** (1960) 696]

[45] W.L. McMillan, Phys. Rev. B **12** (1968) 331

[46] R. Bhandari and L.M. Falicov, J. Phys. C **6** (1973) 479

[47] K. Yamaguchi, Ph.D. thesis, Osaka University, Japan, 1997

List of Publications

1. Y. Matsumoto, M. Otani, H. Miyagi and N. Suzuki
   "Theoretical Study on Organic One-Dimensinal Ferrimagnets"
   Molecular Crystals and Liquid Crystals, **306** (1997) 339-344.

2. Y. Matsumoto, M. Otani, H. Miyagi and N. Suzuki
   "Magnetic Susceptibility of Spin-Alternating Chains"
   Journal of the Physical Society of Japan, **66** No.6(1997) 1844-1845.

3. M. Otani, K. Yamaguchi. H. Miyagi and N. Suzuki
   "First-Principles Calculations of Electronic Band Structures of High Pressure Phase of Solid Oxygen"
   The Review of High Pressure Science and Technology, **7** (1998) 178-180.

4. M. Otani, K. Yamaguchi, H. Miyagi and N. Suzuki
   "The Pressure-Induced Insulator-Metal Transition of Solid Oxygen
   – Band-Structure Calculatoins"
   Journal of Physics: Condensed Matter, **10** (1998) 11603-11606.

5. M. Otani, H. Miyagi and N. Suzuki
   "Theoretical Study of Magnetic Properties of Low-Dimensional Oxygen Molecular Assemblies"
   Physica B: Condensed Matter, **265** (1999) 60-63.

6. M. Otani and N. Suzuki
   "Theoretical Study on Electronic Structure and Lattice Dynamics of Solid O and Se under High Pressures"
   The Review of High Pressure Science and Technology, in press.